



Faculty of Mechanical and Process Engineering  
University of Applied Sciences Düsseldorf

MASTER'S THESIS

# Extension of the multi-level *hp* Finite Cell Method for Efficient Thermo-Viscoplastic Analysis

A thesis submitted for obtaining the degree of

*Master of Science*

in Mechanical Engineering by

Oliver Wege

**Matriculation number:** 796046

**Supervisor:** Prof. Dr.-Ing. habil. Martin Ruess  
Computational Mechanics

**2nd Examiner:** Prof. Dr.-Ing. Roland Reichardt  
Informatics

**Advisor:** Jan Niklas Schmäke, M.Sc.  
Computational Mechanics

**Date of submission:** March 20, 2024



## Extension of the multi-level *hp* Finite Cell Method for Efficient Thermo-Viscoplastic Analysis

The finite cell method (FCM) is a higher order fictitious domain method which is perfectly suited for the analysis of domains of very high complexity including demanding geometry, multi-material interfaces or moving domain fronts, to name just a few challenging fields of modeling & analysis. The interplay of sophisticated developments in the context of model refinement, the treatment of essential boundary conditions and the benefits of higher order approximation spaces form this novel type of numerical solution method, which offers the highest degree of modeling flexibility and superior convergence properties compared to the established finite element (FEM) standard [1].

Recently, the method has demonstrated its extensibility for plastic analysis, outperforming classical FEM solutions by using high order approximation and hierachic model refinement [2,3]. An extension to viscoplasticity is of major relevance e.g. for the rate-dependent prediction of the deformation behavior of metals over time to capture the creep flow after the application of external loading. To this end, a viscoplasticity model shall be implemented into the existing FCM-Framework FELiNA (Finite Elements for Linear and Non-linear Analyses). Moreover, a coupling extension for thermo-elastic and thermo-viscoplastic analysis is to be prepared as part of the code development. The implementation shall be extensively tested and compared with documented benchmark solutions and models from the engineering routine.

The project includes the following items:

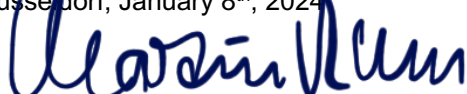
1. Development of a workplan including appropriate work packages and *Milestones*.
2. Literature research on established viscoplasticity models, including the reasoned selection of a suitable model to be implemented and tested.
3. The implementation includes the following steps:
  - Getting familiar with the FCM framework FELiNA and the documentation of the latest extensions to plasticity [3].
  - Appropriate choice of a viscoplasticity model suited for the deformation analysis of metals at high temperatures and implementation into FELiNA.
  - Implementation of a thermo-elastic coupling as preparation for a later thermo-viscoplastic analysis.
  - Code verification of the implemented software packages with appropriate benchmark problems from literature. Identification of potential limit points of the implemented model.
  - Modeling and analysis of a demonstrator example including a critical assessment of the quality and reliability of the analysis.
4. Documentation of all work steps including the developed software extensions and analyzed problems with LaTeX. The documentation should also include appropriate comments in the developed code.

[1] D. Schillinger, M. Ruess. The Finite Cell Method: A review in the context of higher-order structural analysis of CAD and image-based geometric models, Archives of Computational Methods in Engineering 22(3): 391-455, 2015.

[2] A. Abedian, J. Parvizian, A. Düster, E. Rank. The finite cell method for the J2 flow theory of plasticity, Finite Elements in Analysis and Design 69: 37-47, 2013.

[3] J.N. Schmäke. Hierachic Refinement and Plasticity Analysis in the Framework of the Finite Cell Method. M.Sc.-Thesis, 06.09.2023, Mechanical Engineering, Düsseldorf University of Applied Sciences.

Düsseldorf, January 8<sup>th</sup>, 2024



Prof. Dr.-Ing. habil. Martin Ruess



*Thanks to friends, family and friends who feel like family for every  
bit of support and encouragement on my journey through life.*



# Abstract

To achieve accurate results, the Finite Cell Method relies on the careful integration of the cells that are cut by the geometric boundary. This generally entails a more computationally demanding integration process compared to conventional FEM, as a large number of quadrature points are usually required in the cut cells. For linear analysis, this is a fair trade-off for the bypassed mesh generation. However, for non-linear analysis, such as viscoplasticity, the cut cells must be integrated many times during the solution procedure and are evaluated at the quadrature points in each iteration to solve the local equations. In this work, the field of viscoplastic analysis shall be extended by using non-negative moment fitting quadrature in the finite cell method combined with multi-level  $hp$  refinements. Instead of conventional cell partitioning to integrate the cut cells, this novel quadrature rule is used to find an optimized, usually much smaller set of quadrature points beforehand, which pays off in efficiency during the non-linear analysis. This approach is extended with multi-level  $hp$  refinements to precisely capture non-smooth features in local events. By coupling the viscoplastic with thermal analysis, a wide range of complex problems from engineering praxis can be modeled.



# Contents

<b>1</b>	<b>Introduction</b>	<b>11</b>
<b>2</b>	<b>Fundamental concepts</b>	<b>13</b>
2.1	The finite element method . . . . .	13
2.1.1	Strong form . . . . .	13
2.1.2	Galerkin method of weighted residuals . . . . .	14
2.1.3	Approximation space . . . . .	16
2.1.4	High-order shape functions . . . . .	18
2.1.5	Algebraic system of equations . . . . .	21
2.1.6	Convergence properties of $h$ -FEM and $p$ -FEM . . . . .	23
2.1.7	Multi-level $hp$ -FEM . . . . .	25
2.2	The finite cell method . . . . .	32
2.2.1	Basic concept . . . . .	32
2.2.2	Adaption of the weak formulation . . . . .	33
2.2.3	Integration of cut-cells . . . . .	34
<b>3</b>	<b>Efficient integration of cut-cells</b>	<b>37</b>
3.1	Moment fitting quadrature . . . . .	38
3.1.1	Non-negative moment fitting . . . . .	39
3.1.2	Adaptive algorithm . . . . .	42
3.2	Numerical results . . . . .	43
3.2.1	Recovery of the Gauss-Legendre quadrature . . . . .	43
3.2.2	Sphere-cut unit cell . . . . .	44
<b>4</b>	<b>Linear thermoelasticity</b>	<b>47</b>
4.1	Linear elasticity . . . . .	47
4.1.1	Kinematics of deformation . . . . .	47
4.1.2	Balance of forces and momentum . . . . .	49
4.1.3	Constitutive relation . . . . .	50
4.1.4	Strong form . . . . .	51
4.1.5	Weak form . . . . .	51
4.2	Formulation of the multi field problem . . . . .	53

4.3 Weak form of linear thermoelasticity . . . . .	56
4.4 Ring plate benchmark . . . . .	59
<b>5 Small strain elastoplasticity</b>	<b>63</b>
5.1 Mathematical theory . . . . .	63
5.1.1 Strain decomposition . . . . .	65
5.1.2 Free energy potential . . . . .	65
5.1.3 Elastic material law . . . . .	68
5.1.4 Yield criterion . . . . .	69
5.1.5 Plastic flow rule . . . . .	71
5.1.6 Hardening law . . . . .	72
5.1.7 Summary of the elastoplastic model . . . . .	74
5.2 Finite elements for elastoplasticity . . . . .	74
5.2.1 Euler discretization of the initial value problem . . . . .	75
5.2.2 Global incremental-iterative solution procedure . . . . .	76
5.2.3 Elastic predictor return mapping algorithm . . . . .	80
5.2.4 Elastoplastic consistent tangent operator . . . . .	84
5.3 Perforated plate benchmark . . . . .	86
<b>6 Thermo-viscoplasticity</b>	<b>91</b>
6.1 Mathematical theory of viscoplasticity . . . . .	91
6.1.1 Viscoplastic flow rule and hardening law . . . . .	93
6.1.2 Summary of the viscoplastic model . . . . .	94
6.1.3 Euler discretization of the viscoplastic initial value problem . . . . .	94
6.1.4 Elastic predictor viscoplastic return mapping algorithm . . . . .	95
6.1.5 Viscoplastic consistent tangent operator . . . . .	98
6.2 Viscoplastic perforated plate benchmark . . . . .	100
6.3 Thermo-viscoplastic coupling . . . . .	107
6.3.1 Numerical treatment of temperature-dependent parameters . . . . .	109
6.3.2 Thermo-viscoplastic perforated plate benchmark . . . . .	111
6.4 Analysis of a metal foam pore . . . . .	113
<b>7 Conclusion and outlook</b>	<b>117</b>

# Chapter 1

## Introduction

### Motivation and objectives

The simulation of physical phenomena in engineering, physics, medicine or biology has become increasingly relevant to the research community and in industry over the last decades. Engineers use powerful numerical solution methods like the finite element method (FEM) to estimate the safety, practicability or durability of their design. The finite element method is the foundation of the finite cell method (FCM). A method that bypasses the computationally expensive mesh generation of the standard finite element method by using the fictitious domain approach. In combination with the use of high order approximation spaces, the finite cell method is a powerful analysis tool to accurately simulate geometries of high complexity. Lately, refinement techniques like the multi-level  $hp$  method were developed to adaptively refine the mesh locally by superposition. This way, an entire remeshing of the domain is avoided and especially non-smooth features in local events can be captured with high accuracy.

The main objective of this work is the identification of a viscoplastic material model for metals and implementation into the framework of the finite cell method using multi-level  $hp$  overlay refinements.

This model shall be prepared for the thermo-viscoplastic coupling to simulate rate-dependent plastic flow of metals at high temperatures. Foundation of the thermal coupling is the linear thermoelasticity theory. The derived model shall be tested on benchmark problems against established references.

A third part of this work deals with the efficient numerical integration of cut-cells in the finite cell method for nonlinear analysis. The novel non-negative moment fitting approach is tested on the models throughout this work in terms of stability and efficiency.

## Outline

**Chapter 2** states the fundamentals for the methods used in this work. The finite element method is outlined with its main properties and characteristics from the differential equation in the strong form to weak integral equations and finally the numerically treatable algebraic system of equations. Additionally, the finite cell method is briefly introduced.

**Chapter 3** proposes the use of the moment fitting quadrature approach to numerically integrate cut-cells in the finite cell method efficiently.

**Chapter 4** outlines the theory of linear elasticity and its coupling with the heat conduction problem in preparation for the thermo-viscoplastic coupling.

**Chapter 5** treats the basis of the viscoplastic theory. The rate-independent elastoplastic theory is introduced beforehand to be extended to the rate-dependent theory of viscoplasticity. Both models are derived under the assumption of infinitesimal small strains.

**Chapter 6** finally captures the viscoplastic model and its thermal coupling. Besides the analysis of a benchmark problem, a model with higher geometric complexity is presented to demonstrate the performance of the proposed material model and quadrature scheme.

# Chapter 2

## Fundamental concepts

### 2.1 The finite element method

To illustrate the fundamental principles of the finite element method, the derivation process of the algebraic system of equations from a boundary-constrained partial differential equation is outlined in this section. Solving a boundary value problem by means of the finite element method essentially requires two main components:

- the weak formulation of the problem, and
- a space of trial functions which approximate the weak equations.

The strong formulation implies a solution space that already fulfills the equations and boundary conditions at each and every point of the solution domain. Whereas the weak formulation is not required to fulfill the equations and boundary conditions absolutely, but only has weak solutions concerning certain trial (or test) functions.

#### 2.1.1 Strong form

For the sake of simplicity and later use, the scalar-valued field problem of stationary heat conduction is used to describe the procedure. Let  $u(\mathbf{x})$  be the primal unknown (temperature), let  $\mathbf{q}(\mathbf{x})$  denote the flux (heat flux vector) and let  $s(\mathbf{x})$  be a source function (heat supply per unit volume) at a point  $\mathbf{x} \in \mathbb{R}^d$  on the domain  $\Omega$  with spatial dimension  $d = 1, \dots, 3$ . The relationship between the primal unknown and the flux is described by a constitutive equation that reflects the material behavior of the body. In the case of heat conduction, Fourier's law covers this part with

$$\mathbf{q} = -\kappa \cdot \nabla u, \quad \nabla u = \frac{\partial u}{\partial \mathbf{x}} = \frac{\partial u}{\partial x_i}, \quad i = 1, \dots, d \quad (2.1)$$

where  $\kappa$  is a symmetric tensor describing the conductivity of the material. If  $\kappa$  is constant over  $\Omega$ , the material is classified as homogenous, and it is said to be isotropic, if the

material behaves uniformly in all spatial orientations, namely  $\kappa = \kappa \cdot \mathbf{I}$ . The strong form of stationary heat conduction can be summarized as

$$\nabla \cdot \mathbf{q} + s = 0 \quad \forall \mathbf{x} \in \Omega \quad (2.2a)$$

$$\mathbf{q} = -\kappa \cdot \nabla u \quad \forall \mathbf{x} \in \Omega \quad (2.2b)$$

$$u = \bar{u} \quad \forall \mathbf{x} \in \Gamma_D \quad (2.2c)$$

$$\mathbf{q} \cdot \mathbf{n} = \bar{q} \quad \forall \mathbf{x} \in \Gamma_N \quad (2.2d)$$

where (2.2a) is the diffusion equation or, for  $\kappa = \mathbf{I}$ , known as the Poisson equation, and represents the equilibrium state in the form of a partial differential equation. The vector  $\mathbf{n}$  is the surface normal at  $\mathbf{x}$ . Equation (2.2c) is a so-called *Dirichlet* or *essential* boundary condition with prescribed temperatures on the boundary  $\Gamma_D$ . Equation (2.2d) is called a *Neumann* or *natural* boundary condition where the heat flux on the boundary  $\Gamma_N$  is prescribed. It shall be noted that the boundaries of prescribed values do not intersect and that their union describes the complete boundary of  $\Omega$ , that is

$$\Gamma_D \cap \Gamma_N = \emptyset \quad \wedge \quad \Gamma_D \cup \Gamma_N = \Gamma = \partial\Omega. \quad (2.3)$$

## 2.1.2 Galerkin method of weighted residuals

To transfer the strong form (2.2) to the weak form of the problem, two kinds of functions shall be introduced. Firstly, the set of trial functions

$$\mathcal{T} = \{u(\mathbf{x}) \mid u \in \mathcal{H}^1(\Omega), u = \bar{u} \ \forall \mathbf{x} \in \Gamma_D\}, \quad (2.4)$$

containing all functions  $u$  which satisfy the Dirichlet boundary condition (2.2c) a priori and are contained in the Sobolev space of functions  $\mathcal{H}^1$  defined by

$$\mathcal{H}^1(\Omega) := \{u \in \mathcal{L}^2 \mid \exists \nabla u : \nabla u \in \mathcal{L}^2(\Omega)\}, \quad \mathcal{L}^2(\Omega) = \int_{\Omega} (\nabla u)^2 d\Omega < \infty, \quad (2.5)$$

namely,  $u$  is square-integrable and its derivative exists and is square-integrable as well. The first step of the method of weighted residuals is to identify the residual terms of the strong form (2.2) by rearrangement

$$r_{1_\Omega} := \nabla \cdot (\kappa \cdot \nabla u) - s = 0 \quad \forall \mathbf{x} \in \Omega \quad (2.6a)$$

$$r_{2_\Gamma} := u - \bar{u} = 0 \quad \forall \mathbf{x} \in \Gamma_D \quad (2.6b)$$

$$r_{3_\Gamma} := \mathbf{q} - \bar{\mathbf{q}} = 0, \quad \mathbf{q} = -\kappa \cdot \nabla u \cdot \mathbf{n} \quad \forall \mathbf{x} \in \Gamma_N \quad (2.6c)$$

where the method of weighted residuals transforms the set of residual equations into the minimization problem

$$\sum_{i_\Omega} \int_{\Omega} v \cdot r_{i_\Omega} d\Omega + \sum_{j_\Gamma} \int_{\Gamma} v \cdot r_{j_\Gamma} d\Gamma = 0. \quad (2.7)$$

At this point, the second kind of function is introduced, namely the set of weight functions, or in a Galerkin-sense variations

$$\mathcal{V} = \{v \mid v \in \mathcal{H}^1(\Omega), v = 0 \ \forall x \in \Gamma_D\} \quad (2.8)$$

which have the same requirements as the trial functions, except that they satisfy the homogenous form ( $\bar{u} = 0$ ) of the Dirichlet boundary condition (2.2c). To proceed with the integral equation of weighted residuals (2.7)

$$\int_{\Omega} v \cdot [\nabla \cdot (\kappa \cdot \nabla u) - s] d\Omega + \int_{\Omega} v \cdot [u - \bar{u}] d\Omega + \int_{\Omega} v \cdot [\kappa \cdot \nabla u + \bar{q}] d\Omega = 0, \quad (2.9)$$

integration by parts is applied to the first integral term to reduce the derivative of  $u$  from second to first order. After rearrangement, the variational equation reads

$$\begin{aligned} \int_{\Omega} \nabla v \cdot \kappa \cdot \nabla u d\Omega &= \int_{\Omega} v \cdot s d\Omega + \int_{\Gamma_D} v \cdot q d\Gamma + \int_{\Gamma_N} v \cdot \bar{q} d\Gamma \\ &\wedge u = \bar{u} \quad \forall x \in \Gamma_D \end{aligned} \quad (2.10)$$

providing the so-called *Extended Principle of Virtual Temperatures* where  $v$  are the virtual temperatures. The first integral term on the right-hand side can be considered as the volume load term, the second term is the extension term which reflects the dual unknowns, namely heat flux reactions, and the last integral term denotes the surface loading. The Dirichlet boundary conditions are considered in a strong form concerning the prescribed temperatures. The symmetry of the bilinear functional follows from the symmetry of the material tensor of conductivities  $\kappa$  and also holds for isotropic materials in elastic problems. To write the weak form compactly, (2.10) can also be written in terms of a symmetric bilinear functional containing the left-hand side of the equation and a linear functional containing the right-hand side

$$\mathcal{B}(v, u) = \mathcal{F}(v) \quad (2.11a)$$

$$\mathcal{B}(v, u) := \int_{\Omega} \nabla v \cdot \kappa \cdot \nabla u d\Omega, \quad \mathcal{B}(v, u) = \mathcal{B}(u, v) \quad (2.11b)$$

$$\mathcal{F}(v) := \int_{\Omega} v \cdot s d\Omega + \int_{\Gamma_D} v \cdot q d\Gamma + \int_{\Gamma_N} v \cdot \bar{q} d\Gamma. \quad (2.11c)$$

Galerkin's method of weighting the residuals is well established in the finite element method and suggests utilizing finite-dimensional subsets  $\mathcal{T}^h \subset \mathcal{T}$  and  $\mathcal{V}^h \subset \mathcal{V}$  to approximate the weak solution. Hence, the subsets  $(\circ)^h$  contain trial and weight functions, respectively, that are also in the supersets and therefore satisfy the same requirements. The superscript  $h$  is considered to be associated with the parametrization of a discretized domain – like a mesh – where  $h$  denotes the characteristic length of the discrete finite elements.

Since they appear with the same order of derivative in the weak form, the so-called *Bubnov-Galerkin approach* suggests that the weight function  $v^h \in \mathcal{V}^h$  is taken from the same set of functions as the trial function  $u^h \in \mathcal{T}^h$ . More specifically, the variations of the trial function  $u^h$  should be used as the weight functions

$$v_i^h = \delta u_i^h = \frac{\partial u^h}{\partial u_i}, \quad i = 1, \dots, n \quad (2.12)$$

which means taking the partial derivatives of the trial function with respect to its unknown coefficients  $u_i$ , yielding  $n$  weight functions. Let  $\mathcal{V}^h$  consist of all linear combinations of given functions  $N_i(\mathbf{x})$ ,  $i = 1, \dots, n$  such that the trial function decomposes into the sum

$$u^h(\mathbf{x}) = \sum_{i=1}^n u_i \cdot N_i(\mathbf{x}), \quad (2.13)$$

then the weight functions yield

$$v_i^h(\mathbf{x}) = \frac{\partial}{\partial u_i} \left[ \sum_{j=1}^n u_j \cdot N_j(\mathbf{x}) \right] = N_i(\mathbf{x}), \quad i = 1, \dots, n. \quad (2.14)$$

The functions  $N_i$  are referred to as basis or shape functions.

### 2.1.3 Approximation space

A key feature of the finite element method is the definition of the approximation function  $u^h(\mathbf{x})$  in a piecewise manner. A set of shape functions  $N_i$  is defined exclusively on their respective element domain  $\Omega_e$  for each of the non-overlapping elements, as Figure 2.1 depicts. Thus, the piecewise approximation holds the properties

$$u^h(\mathbf{x}) \in \begin{cases} C^\infty & \forall \mathbf{x} \in \Omega_e \quad "all derivatives of u^h are continuous on \Omega_e" \\ C^0 & \forall \mathbf{x} \in \Omega \quad "no derivative of u^h is continuous on \Omega". \end{cases} \quad (2.15)$$

Moreover, the shape functions are not defined in terms of global coordinates  $\mathbf{x}$ , but instead on a reference element  $\Omega_\xi$  with coordinates  $\xi \in [-1, 1]^d$  in the sense that all elements are hypercubes. Defining the shape functions on a normalized reference

domain enables a straightforward automation of the approximation space, since the shape functions are identical for each element of identical kind.

Let  $\Omega$  be a one-dimensional domain such that  $d = 1$  and a linear approximation basis, then  $\Omega$  is composed of the union of all non-overlapping  $\Omega_e = [x^{(1)}, x^{(2)}]$  and the reference space is  $\Omega_\xi = [-1, 1]$ . The global coordinates of an element can then be interpolated by the mapping

$$x(\xi) = \mathbf{x}_e^\top \cdot \mathbf{N}(\xi), \quad \text{with } \mathbf{x}_e^\top = [x^{(1)} \ x^{(2)}] \quad \text{and} \quad \mathbf{N}(\xi) = \frac{1}{2} \begin{bmatrix} 1 - \xi \\ 1 + \xi \end{bmatrix} \quad (2.16)$$

where  $N_i(\xi) \in [0, 1]$ . Assuming an *isoparametric* mapping, the physics follows by

$$u^h(\xi) = \mathbf{u}_e^\top \cdot \mathbf{N}(\xi), \quad \text{with } \mathbf{u}_e^\top = [u^{(1)} \ u^{(2)}] \quad \text{and} \quad \mathbf{N}(\xi) = \frac{1}{2} \begin{bmatrix} 1 - \xi \\ 1 + \xi \end{bmatrix} \quad (2.17)$$

using the same shape functions. Each element is characterized by a set of points, which coincide with the element's vertices in the case of a linear approximation space. These points are the discrete supports for the unknown values  $\mathbf{u}_e$  and are referred to as nodes, where  $(\bullet)^{(i)}$  indicates the  $i$ 's node of an element.

For the two-dimensional bilinear quadrilateral element in Figure 2.1, the shape functions can be obtained by taking the tensor product of two one-dimensional shape function vectors  $\mathbf{N}^{1D}(\xi) = [N_1(\xi) \ N_2(\xi)]^\top$  given in (2.17)

$$\tilde{\mathbf{N}}^{2D}(\xi) = \mathbf{N}^{1D}(\xi_1) \otimes \mathbf{N}^{1D}(\xi_2) = \begin{bmatrix} N_1(\xi_1) \cdot N_1(\xi_2) & N_1(\xi_1) \cdot N_2(\xi_2) \\ N_2(\xi_1) \cdot N_1(\xi_2) & N_2(\xi_1) \cdot N_2(\xi_2) \end{bmatrix} \quad (2.18)$$

It should be noted that this is just a neat way of noting the multiplication and does not necessarily make sense in the context of vector algebra. Nevertheless, the term *tensor product space* refers to such higher-dimensional shape function spaces. The mapping between the global  $\Omega_e$  and local  $\Omega_\xi$  is then governed by

$$\mathbf{x}(\xi) = \mathbf{x}_e^\top \cdot \mathbf{N}(\xi), \quad \text{with } \mathbf{x}_e = \begin{bmatrix} x_1^{(1)} & x_2^{(1)} \\ x_1^{(2)} & x_2^{(2)} \\ x_1^{(3)} & x_2^{(3)} \\ x_1^{(4)} & x_2^{(4)} \end{bmatrix} \quad \text{and} \quad \mathbf{N}(\xi) = \frac{1}{4} \begin{bmatrix} (1 - \xi_1) \cdot (1 - \xi_2) \\ (1 + \xi_1) \cdot (1 - \xi_2) \\ (1 + \xi_1) \cdot (1 + \xi_2) \\ (1 - \xi_1) \cdot (1 + \xi_2) \end{bmatrix}. \quad (2.19)$$

The concept is analogous to shape functions in three dimensions.

The gradient of the approximation (2.13) in the weak form (2.11b) is obtained by using the product rule of differentiation

$$\nabla u^h = \frac{\partial u^h}{\partial \mathbf{x}} = \frac{\partial}{\partial \mathbf{x}} [\mathbf{u}_e^\top \cdot \mathbf{N}(\xi)] = \mathbf{u}_e^\top \cdot \frac{\partial \mathbf{N}(\xi)}{\partial \mathbf{x}} = \mathbf{u}_e^\top \cdot \frac{\partial \mathbf{N}(\xi)}{\partial \xi} \cdot \frac{\partial \xi}{\partial \mathbf{x}}, \quad \frac{\partial \xi}{\partial \mathbf{x}} = \mathbf{J}^{-1} \quad (2.20)$$

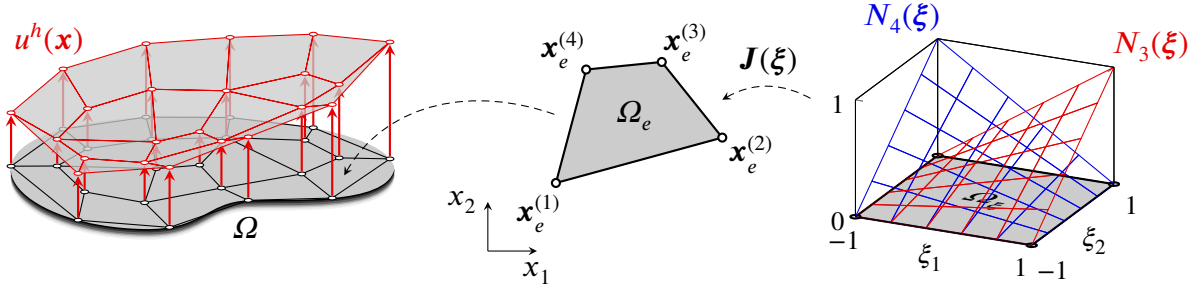


**Figure 2.1** The discretization principle of the finite element method is shown for bilinear quadrilateral elements. The continuous solution domain  $\Omega$  is approximated by a finite number of subdomains  $\Omega_e$ . The nodes  $x_e^{(i)}$  are numbered counter-clockwise by convention. Interpolation and integration is performed on the reference element  $\Omega_\xi$  with normalized coordinates  $\xi \in [-1, 1]^d$  using the shape functions  $N_i(\xi)$ ,  $i = 1, \dots, 4$ . Only the last two of them are shown for the sake of clarity.

with  $J^{-1}$  being the inverse of the so-called Jacobi matrix

$$J := \mathbf{x}_{,\xi} = \frac{\partial \mathbf{x}}{\partial \xi} = \frac{\partial}{\partial \xi} [\mathbf{x}_e^\top \cdot \mathbf{N}(\xi)] = \mathbf{x}_e^\top \cdot \frac{\partial \mathbf{N}}{\partial \xi} \quad (2.21)$$

where the derivatives of the shape functions with respect to the normalized coordinates  $\xi$  can be derived once. This way, they are, just like the shape functions themselves, identical for all elements of the same kind.

## 2.1.4 High-order shape functions

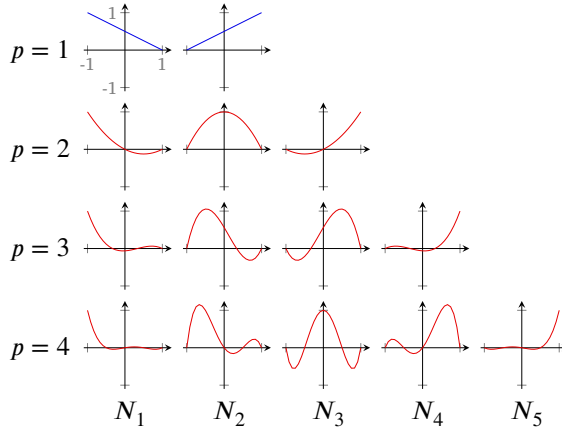
For the majority of problems, it can be assumed, that the solution varies in a nonlinear way over the domain due to the boundary conditions and the geometry. By using many elements with linear shape functions, nonlinearities can be tackled to a certain degree. However, especially in the gradients of  $u^h$ , the linear elements are very limited due to their constant derivatives. For the generation of higher-order approximation spaces, two kinds of shape functions have prevailed to construct a polynomial basis.

### Lagrange shape functions

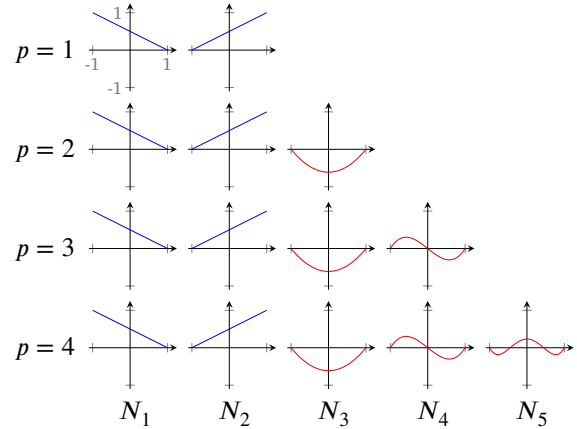
or *nodal finite elements* are based on a set of Lagrange basis polynomials  $N_i$ ,  $i = 1, \dots, p+1$  of degree  $p$  which are uniquely defined for each corresponding shape function space  $\mathcal{S}^p = \{N_1, \dots, N_{p+1}\}$ ,  $p = 1, 2, 3, \dots$ . The basis polynomials are

$$N_i(\xi) = \prod_{j=1, j \neq i}^{p+1} \frac{\xi - \xi_j}{\xi_i - \xi_j}, \quad N_i(\xi_j) = \delta_{ij} = \begin{cases} 1 & i = j \\ 0 & i \neq j \end{cases}, \quad \sum_{i=1}^{p+1} N_i(\xi) = 1 \quad (2.22)$$

where  $\xi_{\{i,j\}}$  are  $p + 1$  equidistant points on  $\xi \in [-1, 1]$ . Due to their Dirac-relation  $\delta_{ij}$  of being 1 at their assigned point and 0 at all other points (see Figure 2.2a) and their



(a) Lagrange



(b) Integrated Legendre

**Figure 2.2** The one-dimensional Lagrange shape functions for polynomial degrees  $p = 1, \dots, 4$  and their hierarchical companion based on integrated Legendre polynomials. Linear shape functions are colored blue while high-order shape functions are colored red.

fulfillment of the partition of unity, they are called interpolatory shape functions. This property is useful to impose inhomogeneous Dirichlet boundary conditions  $u = \bar{u} \neq 0, \forall x \in \Gamma_D$  since  $\bar{u}_i$  can simply be prescribed as the solution for the unknown value  $u_i$  at the corresponding node  $i$  (confer Figure 2.2a & equation (2.17)).

### Integrated Legendre shape functions

or *modal finite elements* are based on a set of linear shape functions  $\{N_1, N_2\}$  and integrated Legendre polynomials  $N_i, i = 3, \dots, p + 1$  of degree  $i - 1$ , which are hierarchically added for each corresponding shape function space  $\mathcal{S}^p = \{N_1, \dots, N_{p+1}\}$ ,  $p = 1, 2, 3, \dots$ . This way, the function space  $\mathcal{S}^{p-1}$  is augmented by a new polynomial  $N_{p+1}$  to form  $\mathcal{S}^p$  rather than defining a completely new set of functions, that is  $\mathcal{S}^{p-1} \subset \mathcal{S}^p, p = 2, 3, \dots$  (see Figure 2.2b). The Legendre polynomials  $P_n$  are defined by their property of being orthogonal polynomials on  $[-1, 1]$  and by normalization of  $P_n(1) = 1$  which is compactly stated in Rodrigues' formula

$$P_n(\xi) = \frac{1}{2^n \cdot n!} \cdot \frac{d^n}{d\xi^n} (\xi^2 - 1)^n. \quad (2.23)$$

The shape functions are then obtained by the integration formula

$$N_i(\xi) = \sqrt{\frac{2i-1}{2}} \cdot \int_{-1}^{\xi} P_{i-1}(\xi) d\xi = \frac{1}{\sqrt{4i-2}} \cdot (P_i(\xi) - P_{i-2}(\xi)), \quad i = 2, 3, \dots \quad (2.24)$$

Both, Lagrange and integrated Legendre, shape functions can be transferred to higher spatial dimensions by the tensor product just like in (2.18). Taking the tensor product of two or three sets of one-dimensional integrated Legendre shape functions will yield

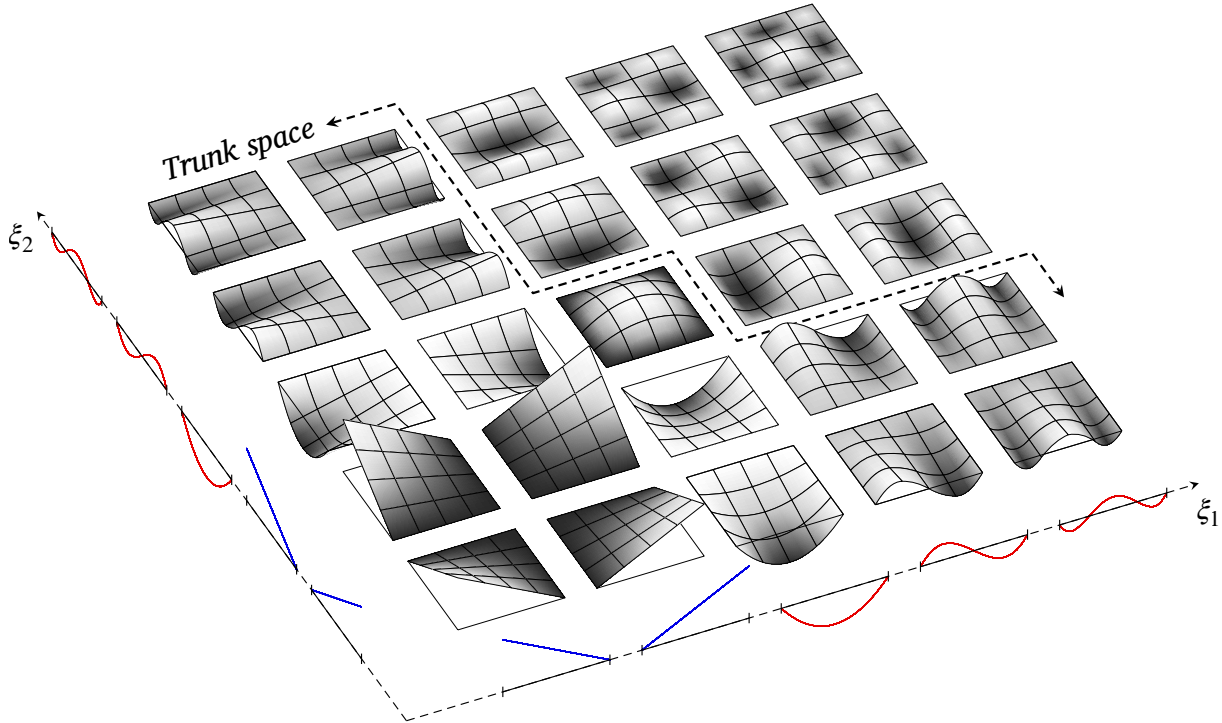


**Figure 2.3** *Tensor product* of the integrated Legendre shape functions for a polynomial degree  $p = 4$  in both dimensions,  $\xi_1$  and  $\xi_2$ . The tensor product of the linear shape functions yields *vertex modes* and their product with higher-order functions are the *edge modes*. The *Surface modes* are the quadrilateral's *internal modes* and are located in the upper  $3 \times 3$  grid where the dashed line indicates which *internal modes* are excluded to span the *trunk space*.

different modes that are associated with the topologies of the element as shown in Figure 2.3. A quadrilateral element shall be assumed. Multiplying the linear shape functions with each other, results in *vertex modes* which are identical to linear Lagrange shape functions. Multiplying linear with high-order shape functions yields *edge modes*, which are shape functions with non-zero values on the associated edge and are zero on all other edges. Multiplying high-order shape functions with each other will lead to *surface modes*, thus modes which are zero on the boundary and non-zero within the surface. Modes that are entirely zero at the boundary are called *bubble* or *internal modes* and can be treated in a special way. While non-internal modes contribute significantly to the interpolation, the internal modes do not. Therefore, some of the internal modes can be omitted to reduce the number of degrees of freedom per element. This so-called *trunk space* is spanned by including only high-order shape functions which satisfy

$$\begin{aligned} \xi_1^i \cdot \xi_2^j, \quad & i = 0, 1, \dots, p_1, \quad j = 0, 1, \dots, p_2 \\ & i + j \leq \max\{p_1, p_2\} \end{aligned} \tag{2.25}$$

for a quadrilateral element and

$$\xi_1^i \cdot \xi_2^j \cdot \xi_3^k, \quad i = 0, 1, \dots, p_1, \quad j = 0, 1, \dots, p_2, \quad k = 0, 1, \dots, p_3 \\ i + j + k \leq \max\{p_1, p_2, p_3\} \quad (2.26)$$

for a hexahedral element. To improve computational efficiency while maintaining the solution quality, the trunk space of integrated Legendre shape functions will be used, unless stated otherwise.

## 2.1.5 Algebraic system of equations

Recall the functionals of the weak form (2.11) and replace  $u$  and  $v$  with their finite-dimensional approximation equivalent  $u^h$  and  $v^h$ .

$$\begin{aligned} \mathcal{B}(v^h, u^h) &= \int_{\Omega} \nabla v^h \cdot \boldsymbol{\kappa} \cdot \nabla u^h d\Omega \\ &= \sum_{i=1}^n \sum_{j=1}^n \int_{\Omega} \nabla N_i \cdot \boldsymbol{\kappa} \cdot \nabla N_j d\Omega \cdot u_j^h \end{aligned} \quad (2.27)$$

$$\begin{aligned} \mathcal{F}(v^h) &= \int_{\Omega} v^h \cdot s d\Omega + \int_{\Gamma_D} v^h \cdot q d\Gamma + \int_{\Gamma_N} N_i \cdot \bar{q} d\Gamma \\ &= \sum_{i=1}^n \int_{\Omega} N_i \cdot s d\Omega + \int_{\Gamma_D} N_i \cdot q d\Gamma + \int_{\Gamma_N} N_i \cdot \bar{q} d\Gamma \end{aligned} \quad (2.28)$$

This approximation of the weak form can now be written in an algebraic system of equations

$$\begin{aligned} \boldsymbol{K} \cdot \boldsymbol{u} &= \boldsymbol{f}, & K_{ij} &= \int_{\Omega} \nabla N_i \cdot \boldsymbol{\kappa} \cdot \nabla N_j d\Omega, \\ f_i &= \int_{\Omega} N_i \cdot s d\Omega + \int_{\Gamma_D} N_i \cdot q d\Gamma + \int_{\Gamma_N} N_i \cdot \bar{q} d\Gamma \end{aligned} \quad (2.29)$$

with  $j = 1, \dots, n$  unknowns or degrees of freedom  $u_i$  and  $i = 1, \dots, n$  equations which can be solved by well-known methods from linear algebra. Note that the extensional flux reaction term over  $\Gamma_D$  is skipped for the load vector from now on since it is not required when solving for the primal unknown of interest. Nonetheless, the dual unknowns might be of interest and can be evaluated in a subsequent step. In the framework of a

piecewise interpolated domain

$$\Omega = \bigcup_e^{\eta_e} \Omega_e \quad (2.30)$$

the system matrix  $\mathbf{K}$  and the system vector  $\mathbf{f}$  are assembled from the contribution of each subdomain  $\Omega_e$

$$\mathbf{K} = \bigwedge_e^{\eta_e} \mathbf{K}_e, \quad \mathbf{f} = \bigwedge_e^{\eta_e} \mathbf{f}_e \quad (2.31)$$

which shall be referred to as elements. This act is denoted by the assembly operator  $\bigwedge$  which can be seen as a topological routine of assigning the element contributions  $(\circ)_e$  to their respective degrees of freedom in the system. The element integrals are evaluated by numerical quadrature rules where the Gauss quadrature rule dominates the vast majority of use cases due to its accuracy for sufficiently smooth integrands. The quadrature process is automated by integrating over the reference element domain  $\Omega_\xi$  and mapping the integral to the element domain  $\Omega_e$  with the help of the Jacobi matrix  $\mathbf{J} = \mathbf{x}_\xi = \partial \mathbf{x}_i / \partial \xi_j$  and its determinant  $|\mathbf{J}| = \det \mathbf{J}$

$$K_{e_{ij}} = \int_{\Omega_e} \nabla N_i \cdot \boldsymbol{\kappa} \cdot \nabla N_j d\Omega = \int_{\Omega_\xi} \nabla N_i \cdot \boldsymbol{\kappa} \cdot \nabla N_j \cdot |\mathbf{J}| d\Omega \quad (2.32a)$$

$$\approx \sum_{k=1}^{n_e^{\text{qp}}} \nabla N_i(\xi_k) \cdot \boldsymbol{\kappa} \cdot \nabla N_j(\xi_k) \cdot |\mathbf{J}(\xi_k)| \cdot w_k \quad (2.32b)$$

$$f_{e_i} = \int_{\Omega_e} N_i \cdot s d\Omega + \int_{\Gamma_{N_e}} N_i \cdot \bar{q} d\Gamma = \int_{\Omega_\xi} N_i \cdot s \cdot |\mathbf{J}| d\Omega + \int_{\Gamma_{N_e}} N_i \cdot \bar{q} d\Gamma \quad (2.33a)$$

$$\approx \sum_{k=1}^{n_e^{\text{qp}}} N_i(\xi_k) \cdot s(\mathbf{x}(\xi_k)) \cdot |\mathbf{J}(\xi_k)| \cdot w_k + \int_{\Gamma_{N_e}} N_i \cdot \bar{q} d\Gamma \quad (2.33b)$$

with  $\{i, j\} = 1, \dots, n_e^{\text{sf}}$  where  $n_e^{\text{sf}}$  is the number of shape functions assigned to the degrees of freedom of the element and  $n_e^{\text{qp}}$  being the number quadrature points in the element.  $\{\xi_k, w_k\}$  is the quadrature pair of the point in the reference coordinate system and its corresponding weight. If the considered material is inhomogeneous  $\boldsymbol{\kappa} = \boldsymbol{\kappa}(\mathbf{x})$ , the material matrix  $\boldsymbol{\kappa}$  must also be evaluated at the quadrature points as well.

The integral term of the element vector over the Neumann boundary  $\Gamma_{N_e}$  in (2.33b) has to be treated separately since it requires an additional mapping from the spatial dimension of the boundary  $d - 1$  to the domain  $d$ . This mapping involves quadrature

points on the surface (3D) or line (2D) topology

$$\begin{aligned} \int_{\Gamma_{N_e}} N_i \cdot \bar{q} d\Gamma &= \int_{\Gamma_{N_\zeta}} N_i^\Gamma(\zeta) \cdot \bar{q} \cdot |\mathbf{J}| \cdot |\mathbf{J}^\Gamma| d\Gamma, \quad \mathbf{J} = \frac{\partial \mathbf{x}}{\partial \zeta}, \quad \mathbf{J}^\Gamma = \frac{\partial \xi}{\partial \zeta} \\ &\approx \sum_{k=1}^{n_{\text{top}}^{\text{qp}}} N_i^\Gamma(\zeta_k) \cdot \bar{q} \cdot |\mathbf{J}(\xi_k)| \cdot |\mathbf{J}^\Gamma(\zeta_k)| \cdot w_k^\Gamma d\Gamma, \quad \bar{q} = \bar{q}(\mathbf{x}(\xi)), \quad \xi = \xi(\zeta) \end{aligned} \quad (2.34)$$

with  $(\bullet)^\Gamma$  being associated with the boundary topology of dimension  $d-1$  to be integrated over its own normalized coordinates  $\zeta$ , and  $n_{\text{top}}^{\text{qp}}$  being the number of quadrature points of this topology. Since the spatial dimension changes during the mapping, the Jacobi matrix is no longer a square matrix, namely  $\mathbf{J}^\Gamma \in \mathbb{R}^{d \times (d-1)}$ . The determinant is then calculated by the Frobenius norm  $\|\mathbf{J}^\Gamma\|_F$  which takes the square root of the sum over all squared entries. In the one-dimensional case, the boundary integral shrinks to a single point evaluation.

To obtain a unique solution  $\mathbf{u}$  for the linear system of equations (2.29), Dirichlet boundary conditions are applied, which have to prevent system modes with zero eigenvalue, e.g. rigid body motions along and around the coordinate axes in the case of an elastostatic problem. The solution vector can then be split into a free  $\mathbf{u}_f$  and a prescribed  $\mathbf{u}_p$  part, allowing to transfer known values to the right-hand side by

$$\begin{bmatrix} \mathbf{K}_{ff} & \mathbf{K}_{fp} \\ \mathbf{K}_{pf} & \mathbf{K}_{pp} \end{bmatrix} \cdot \begin{bmatrix} \mathbf{u}_f \\ \mathbf{u}_p \end{bmatrix} = \begin{bmatrix} \mathbf{f}_f \\ \mathbf{f}_p \end{bmatrix} \quad \Rightarrow \quad \mathbf{K}_{ff} \cdot \mathbf{u}_f = \mathbf{f}_f - \mathbf{K}_{fp} \cdot \mathbf{u}_p. \quad (2.35)$$

Note that the system of equations is not explicitly reordered in most computer implementations, but rather manipulated in the matrix rows and columns associated with the prescribed unknowns by means of suitable data structures.

## 2.1.6 Convergence properties of $h$ -FEM and $p$ -FEM

As shown in Section 2.1.2, Galerkin's approach suggests choosing only a finite-dimensional function space  $\mathcal{T}^h$  from the space of all trial functions  $\mathcal{T}$  to approximate the weak solution. The particular choice of a discretized domain, called *mesh*, with a certain polynomial degree does not necessarily yield a solution of sufficient quality. In addition, for complex engineering and general physics problems, especially with safety-related applications, it is necessary to be aware of the reliability of the results. Therefore, the ability to improve the approximation is of great significance.

Different refinement approaches have been established to improve the quality of the approximated solution by extending the trial function space. The underlying refinement principle is to increase the degrees of freedom. If they are increased in a way such that the trial function space of lower degrees of freedom  $\mathcal{T}_{r-1}^h$  is embedded in the refined one  $\mathcal{T}_r^h$ , that is  $\mathcal{T}_{r-1}^h \subset \mathcal{T}_r^h$ , the process is called an *extension* [Szabó, 1986]. The

following terms are widely used to categorize the major kinds of extensions [Szabó et al., 2004]:

*h*-extension: The element size  $h$  is progressively reduced while the polynomial degree of the shape functions is fixed, typically at  $p = 1$  or  $p = 2$ .

*p*-extension: The polynomial degree of the shape functions  $p$  is increased while the element size  $h$  is fixed.

*hp*-extension: Both element size  $h$  is refined and polynomial degree  $p$  is increased simultaneously.

A small one-dimensional elasticity model shall demonstrate the convergence properties of the *h*- and *p*-extension [Szabó et al., 2004]. The problem is summarized in Figure 2.4, showing a rod which is fixed at the left boundary and subjected to a domain load  $s(x)$ . To assess the approximation quality, the exact solution is derived analytically

$$u(x) = \frac{1}{8} \left( \frac{\sin(8x)}{8} - \cos(8) \cdot x \right) \quad (2.36)$$

which allows for a visual comparison of the refinement strategies. Figure 2.5 depicts the *h*-refined results at the top where the element number is increased by one for each refinement step. With decreasing element size, the nonlinear curve can be represented more and more accurately. However, it requires many elements to accurately capture the nonlinear characteristics, particularly the gradient suffers from linear shape functions due to their constant derivative.

For a quantitative evaluation of the approximation quality, the *relative error in energy norm* [Szabó, 1986] is typically calculated by

$$\|e\|_E = \sqrt{\frac{|\mathcal{B}(\mathbf{u}, \mathbf{u}) - \mathcal{B}(\mathbf{u}^h, \mathbf{u}^h)|}{|\mathcal{B}(\mathbf{u}, \mathbf{u})|}} \quad (2.37)$$

where  $\mathcal{B}(\bullet, \bullet)$  refers to the bilinear functional, see (2.11), and  $\mathbf{u}$  to a reference solution, while  $\mathbf{u}^h$  is the approximated solution. For this problem, the reference energy based on the analytically derived gradient is

$$\mathcal{B}(\mathbf{u}, \mathbf{u}) = 2 \cdot 4.282509341997325 \cdot 10^{-3}. \quad (2.38)$$

To relate the computational effort to the accuracy, the error is plotted over the unconstrained degrees of freedom, or in other words the system dimension of  $\mathbf{K}_{ff}$  in (2.35). Figure 2.4 depicts the convergence curves of the error using different refinement approaches. The *h*-extension results in algebraic rates of convergence towards the exact solution, while the *p*-extension shows exponential rates of convergence during the refinement process. An algebraic rate can be identified as a linear curve on double logarithmic axes. Since the computer implementation uses double precision with

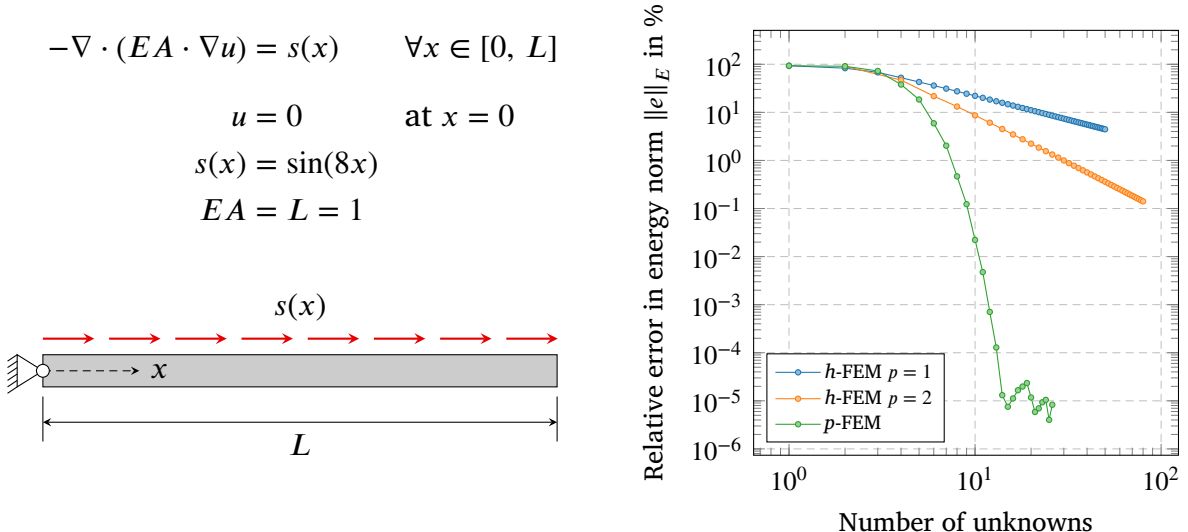


**Figure 2.4** A one-dimensional elasticity benchmark model of a rod subjected to a domain load  $s(x)$ . Note that for unit axial rigidity  $EA$ , the problem is identical to (2.2a) with unit conductivity. The graph on the right shows the convergence of the model to illustrate the basic convergence properties of the  $h$ - and  $p$ -extension.

64 bit for floating point numbers, the subtraction in (2.37) can be computed with a machine accuracy of  $10^{-16}$ . Considering the square root, this leads to an accuracy of  $10^{-8}$  or in percent  $10^{-6}\%$  which is exactly the order of magnitude the  $p$ -FEM stagnates in Figure 2.4.

### 2.1.7 Multi-level $hp$ -FEM

Mesh refinements can be applied on the global domain or locally in regions of interest which can be of great use when dealing with small-scale phenomena, e.g. singularities or discontinuities. This location can either be defined a priori from intuition or posteriori by certain refinement metrics that adaptively refine elements. Figure 2.6 shows a common challenge of local refinements, namely that if the mesh is refined consequently without respecting topological coherence, so-called *hanging nodes* will appear. Hanging nodes have no connection to other elements, thus they can take any value which leads to a violation of the continuity requirement (2.15) of  $u^h$  being  $C^0$  continuous on  $\Omega$ . On the left of Figure 2.6, an alternative refinement process is shown where the  $C^0$  continuity is preserved since no node is unconnected. However, the example also illustrates that the refinement has to propagate into neighboring elements to ensure continuity and therefore loses its local character.

Another aspect of refinements is the process of remeshing. If the mesh should be locally refined where small-scale characteristics like singularities or non-smooth artifacts disturb the approximation quality, smooth regions should remain untouched. Therefore, it is effective to only replace single elements with smaller elements instead of regenera-

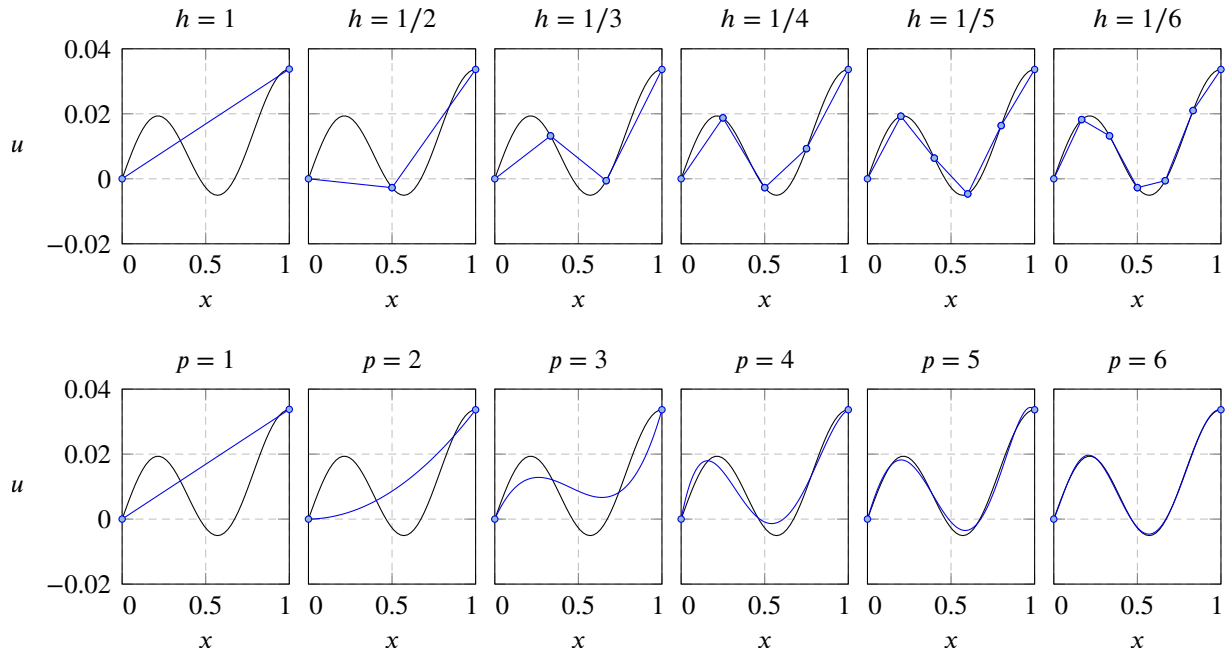


**Figure 2.5** Displacement solution of the one-dimensional elastic rod with  $h$ -refinements on the top and  $p$ -refinements at the bottom. Note that for accurate solutions at the nodes, the source term integral (2.33b) requires a sufficient number of quadrature points to integrate the trigonometric function accurately.

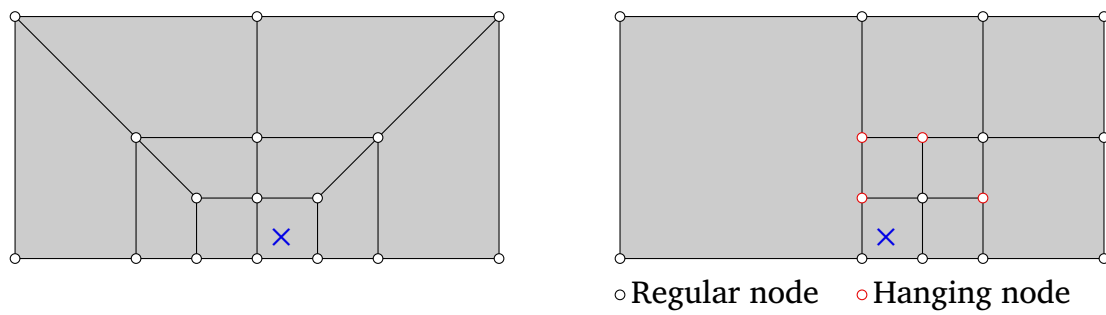


**Figure 2.6** Local refinement of a  $1 \times 2$  mesh at a point of interest  $\text{X}$ . The left strategy shows a mesh that is topologically coherent while the right mesh suffers from hanging nodes [Schmäke, 2023].

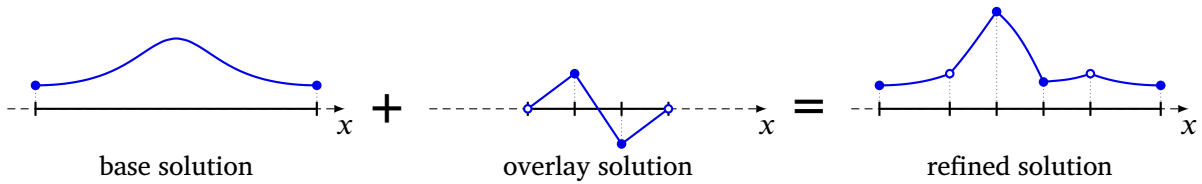


**Figure 2.7** The concept of overlay refinements: Taking a high-order base solution and superimposing a finer, linear mesh to a region of interest. The refined solution composes a high-order approximation with local refinements capturing small-scale characteristics [Schmäke, 2023].

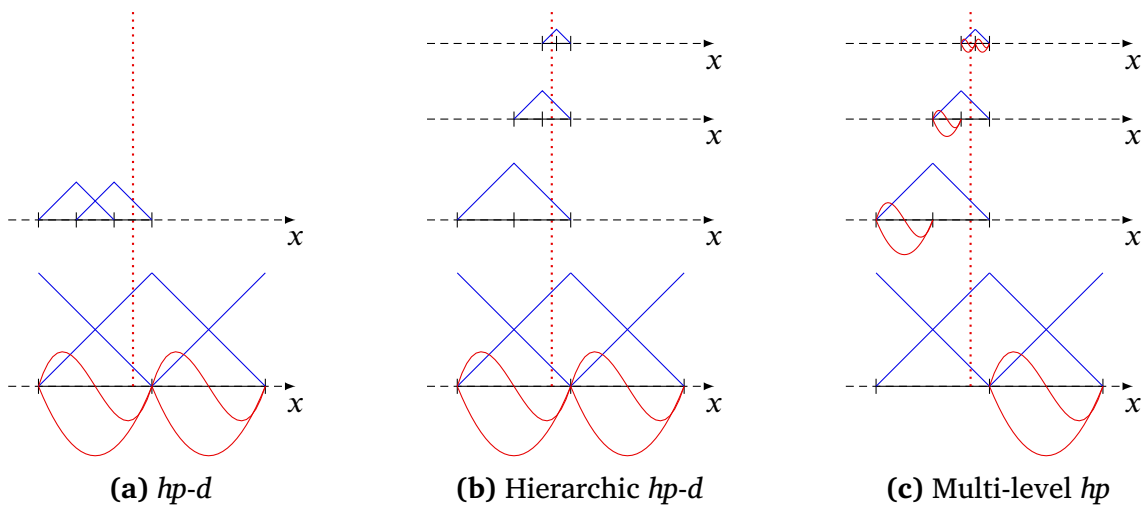


**Figure 2.8** Overlay refinement versions ordered by their time of development. The base solution shall be refined at a point of interest, indicated by the dotted line. Method (a) refines with one linear overlay, (b) uses multiple bisected linear overlays and (c) also refines by bisection, but uses high-order overlays [Schmäke, 2023].

ting a mesh that is identical for the most part. The problem of hanging nodes can be overcome by introducing additional constraints, but this comes with other problems. The implementation of hanging node constraints is highly complex in terms of the algorithmic treatment [Šolín et al., 2008]. Similar to the left example of Figure 2.6, the refinements have to propagate to neighboring elements when following certain regularity rules to ensure continuity. This leads to a decrease in the convergence rates and a loss of the exponential convergence property [Schröder, 2011, Šolín et al., 2010]. In this work, the mesh is refined by superposition instead of replacement, which means that smaller overlaying elements are introduced to refine. The concept of *overlay refinements* was introduced by [Rank, 1992]. The fundamental concept shown in Figure 2.7 suggests superimposing a finer, linear mesh on a high-order base solution. Since the refined solution is a decomposition of a high-order  $p$ -solution and a refined linear  $h$ -overlay, the method is termed *hp-decomposition* or simply the *hp-d*-extension. Figure 2.8a illustrates the shape function space of the *hp-d* refinement. A high-order space of  $p = 3$  is shown which is refined by one linear overlay in the left element. Note that the overlay space does contain the shape functions associated with its boundary,

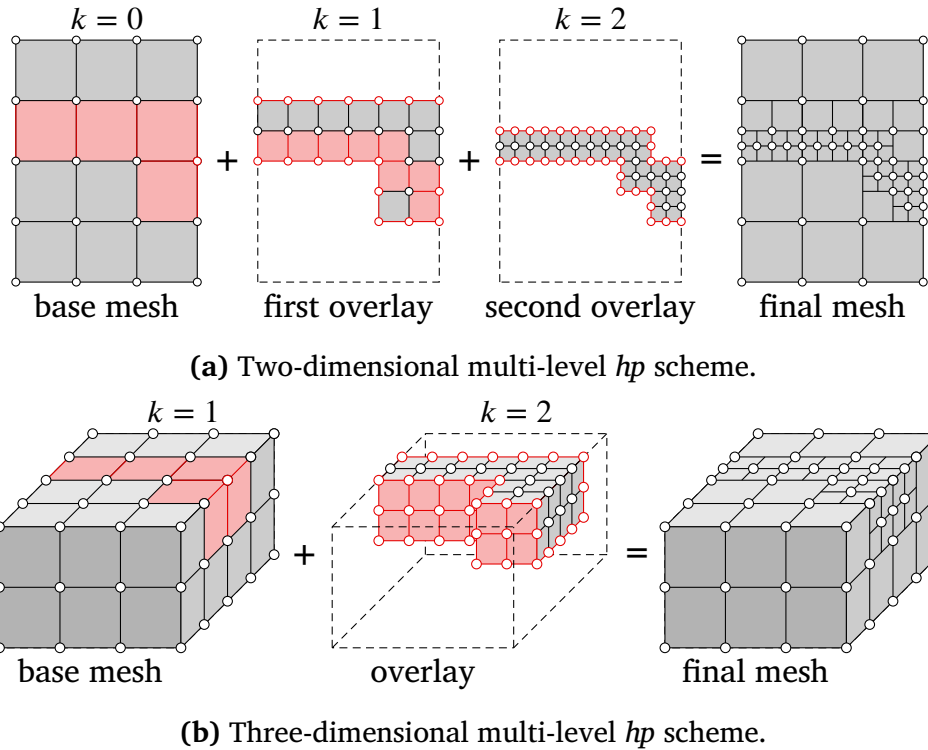


**Figure 2.9** The multi-level *hp* refinement technique in higher dimensions. Topological components (volumes, faces, edges and vertices) colored in red are deactivated in a sense that that their respective mode is removed from the element's shape function space to ensure continuity and linear independence [Schmäke, 2023].

such that continuity can be assured. Over time, the method was further developed, and a hierachic version was proposed in [Schillinger et al., 2012] where the refined element can not only contain one but multiple linear overlays, as depicted in Figure 2.8b. Here, the overlays are bisections of the underlying element and can bisect themselves even further to generate exceptionally fine meshes at regions of interest. The third and final version of the overlay refinement strategy is shown in Figure 2.8c. While the bisection scheme of the refinements remains identical to the hierachic *hp-d* approach, the overlays are allowed to contain high-order shape functions in the multi-level *hp* version. Besides the requirement of continuity, the overlap of identical high-order shape functions produces linear dependent equations in the system of equations (2.29). To avoid linear dependency, the high order shape functions of the lower levels, which are further refined, are omitted.

Extending overlays to the two- and three-dimensional space follows the same principle and requirements of continuity and linear independence among the shape functions. As Figure 2.9 depicts, that certain topological components need to be deactivated in a sense that their corresponding shape function is ignored in the interpolation space. The global  $C^0$  continuity is preserved by deactivating all topologies of the overlay mesh which are located on the internal boundaries, that is boundaries that do not coincide

with the boundaries of the layer below. This ensures that the respective overlay has no contribution to the sum of all shape functions along these boundaries during the interpolation. To retain linear independence each topological component that has an overlay of the same type which is not deactivated by the continuity preservation, needs to be deactivated.

The multi-level *hp* method following [Zander et al., 2015, Zander et al., 2016, Zander, 2017] will be used throughout this work. Since its development and implementation are not part of this work, the reader is referred to [Schmäke, 2023] for the foundation that this work aims to extend. However, the fundamentals are provided for the sake of completeness.

The power of multi-level *hp*-FEM lies in the accuracy for problems with abrupt small-scale events which an ordinary yet high-order element fails to capture. A simple one-dimensional example with a non-smooth solution is used for the demonstration. Smooth problems are differentiable in every location, whereas non-smooth problems are characterized by one or more singular locations where the derivative is undefined. The elastic rod from the previous section in Figure 2.4 shall be considered, but this time a point load  $f = 1/5$  at  $x = 2/3$  is additionally applied. The point load will produce a kink in the displacement solution at  $x = 2/3$  which causes a jump in the gradient. A reference solution can be obtained analogously to the smooth problem by considering the updated boundary conditions

$$u(x) = \frac{1}{8} \left( \frac{\sin(8x)}{8} - \cos(8) \cdot x \right) + \begin{cases} x/5, & x \leq 2/3 \\ 2/15, & x > 2/3 \end{cases} \quad (2.39)$$

providing the gradient by straightforward differentiation

$$\nabla u = \frac{du}{dx} = \frac{1}{8} \left( \cos(8x) - \cos(8) \right) + \begin{cases} 1/5, & x \leq 2/3 \\ 0, & x > 2/3 \end{cases}. \quad (2.40)$$

Figure 2.10 shows the approximation of the gradient for different meshes in blue along with the analytic reference solution in black. On the upper left plot, the domain is interpolated by a single element of polynomial degree  $p = 10$ , which results in an approximation of poor quality since the jump is not characterized in any way. Increasing the polynomial degree to  $p = 30$ , as shown in the lower left plot, leads to an approximation that smoothly tries to represent the jump. However, due to its  $C^\infty$  continuity on the element domain, a smooth polynomial cannot sufficiently represent a discontinuity, like a jump. In addition, using very high polynomial degrees leads to oscillating approximations, which can be seen here in the smooth regions of the analytic solution. On the right-hand side, the element is locally refined towards the point load location. Using an element with  $p = 10$  and performing  $k = 9$  bisectional refinement levels enables the approximated gradient to accurately lie on the smooth

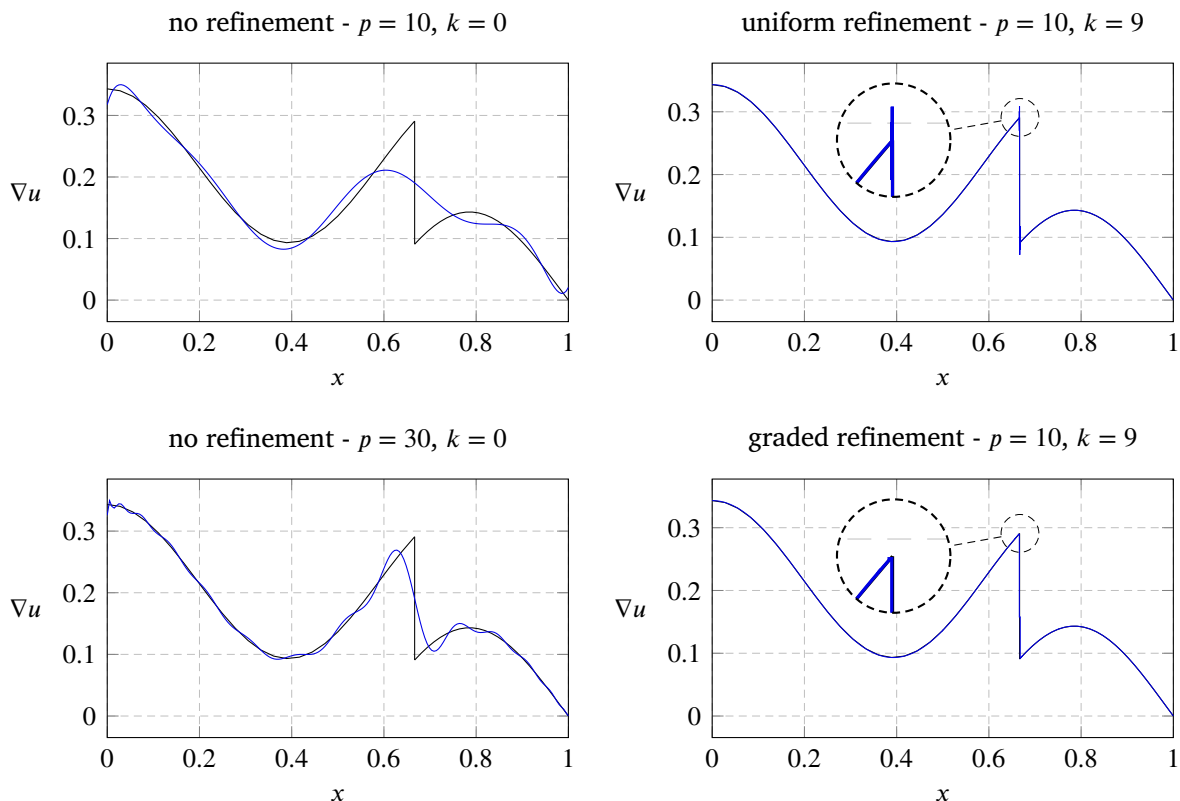


**Figure 2.10** Displacement gradient of the one-dimensional rod with a non-smooth solution using a single element. The  $p$ -FEM on left is compared to the multi-level  $hp$ -FEM on the right with uniform ( $p_k = p_0$ ) and graded ( $p_k = p_0 - k$ ) refinement [Schmäke, 2023].

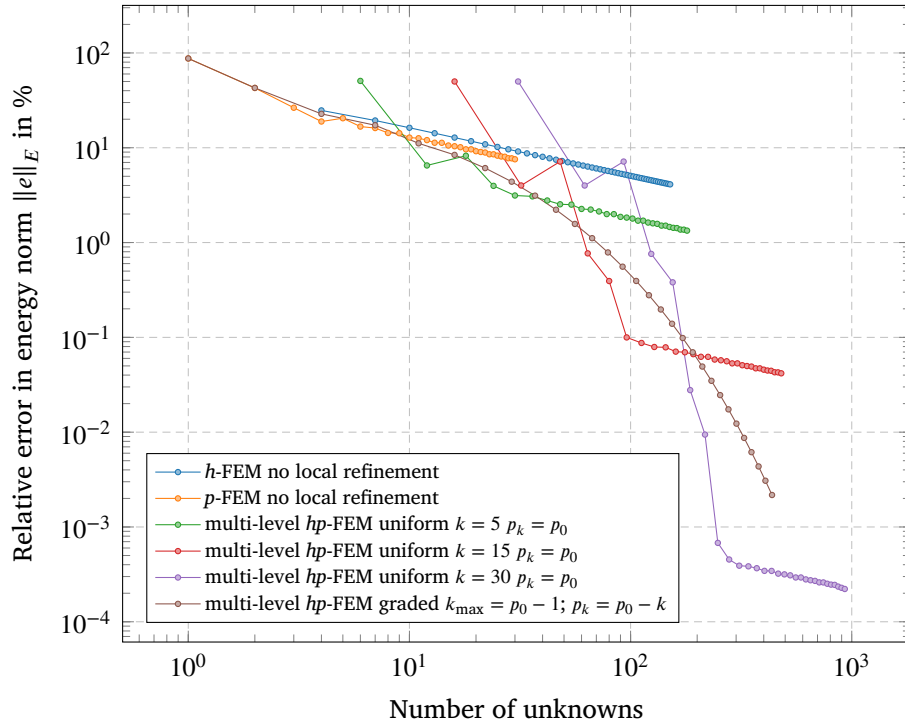


**Figure 2.11** Convergence curves of the different refinement strategies measured in relative error in energy norm. [Schmäke, 2023].

regions while capturing the jump. The term *uniform* refers to the overlay refinements being of the same polynomial degree in all  $k$  levels. This is what causes the overshoot at the jump, since the high-order elements of the refined overlays are oscillating. To circumvent this issue, the lower left plot shows a strategy where the polynomial degree is reduced in a *graded* fashion, namely the polynomial degree of the overlay  $k$  is reduced by one for each level  $p_k = p_0 - k$ . The reduction of the polynomial degree in this case leads to linear shape functions in the finest overlay by defining  $k_{\max} = p_0 - 1$ . Since the derivative of a linear shape function is constant, there is no potential for oscillation. The graded overlay refinement has produced an approximation of very high accuracy which is hardly distinguishable from the exact gradient by visual assessment.

Figure 2.11 depicts the convergence of the non-smooth problem. The reference energy based on the analytically derived gradient is

$$\mathcal{B}(u, u) = 2 \cdot 1.749918889015865 \cdot 10^{-2}. \quad (2.41)$$

Refining the whole rod domain by following the  $h$ - or  $p$ -extension, yields an algebraic convergence behavior from the coarsest mesh onwards with a similar rate of convergence while the  $p$ -FEM produces a slightly smaller error for the same computational effort. Hence, the  $p$ -extension lost its exponential rate of convergence typically associated with smooth problems. The three uniform multi-level  $hp$ -refinements are indicated by using a constant number of overlay refinements while increasing the polynomial

degree uniformly. The term *uniform* still corresponds to the polynomial degree being identical for all layers, namely  $p_k = p_0$ . All three refinements show the behavior of starting with a high convergence rate before changing over to a linear convergence rate. While their linearly converging part has a slope, which is also similar to the slope of the  $h$ - and  $p$ -refinements, the magnitude of error decreases significantly for the same number of unknowns when increasing the number of overlays from over 1% to under  $10^{-3}\%$ . Additionally, the increasing refinement  $k = 5, 15, 30$  also increases the number of  $p$ -refinements where the error converges with a high rate. Lastly, the graded refinement with polynomial degree  $p_k = p_0 - k$  on layer  $k$  and with  $k_{\max} = p_0 - 1$  layers maximum, can maintain an exponential rate of convergence with no sign of disturbance. Nonetheless, the graded refinement technique does not necessarily result in the smallest error for the same number of unknowns, as this model demonstrates.

## 2.2 The finite cell method

The underlying principle of the finite cell method stems from so-called *fictitious domain methods*. They were first introduced in the 1980s, see [Rank and Werner, 1986, Marchuk et al., 1986], aiming to introduce an alternative way to the generic body-fitted mesh generation, which can take up to 80% of the total analysis time [Cottrell et al., 2009]. As depicted in Figure 2.12, the typically complex domain of interest, the *physical domain*  $\Omega_{\text{phy}}$ , is embedded in a *fictitious domain* of primitive geometry  $\Omega_{\text{fict}}$  to be discretized by axis aligned cells. Because the physical boundary  $\partial\Omega_{\text{phy}} = \Gamma_D \cup \Gamma_N$  is now located within the mesh and no longer necessarily coincides with the mesh boundary, they are also referred to as *immersed boundary methods*. While the generation of the axis aligned discretization is computationally cheap, the cells which are cut by the boundary of  $\Omega_{\text{phy}}$ , so-called *cut-cells*, have suffered from highly inaccurate results. Over time, it has become apparent that the solution accuracy can be significantly increased by integrating the cut cells more carefully since their integrand is discontinuous along the domain boundary. With the awareness of accurate cut-cell integration, the fictitious domain methods became increasingly attractive in the field of computational continuum mechanics.

### 2.2.1 Basic concept

The combination of *fictitious domain methods* with the  $p$ -extension of the finite element method was introduced in [Parvizian et al., 2007] for two-dimensional problems and in [Düster et al., 2008] for three-dimensional problems under the name of the finite cell method. The change in terminology from *element* to *cell* originates from the non-body-fitted discretization, that is the fact that the union of all cell domains does not yield the approximation of the physical domain, unlike the elements do in the FEM. Some cells may be completely located outside the physical domain while cut-cells contribute to both domains. The fundamental idea of this approach is, to bypass the computationally

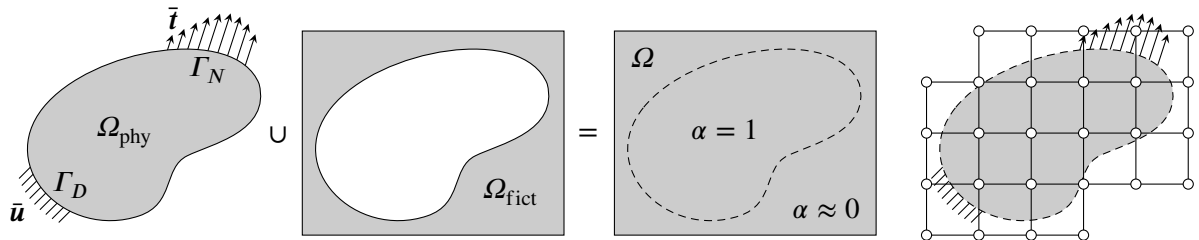


**Figure 2.12** The *fictitious domain approach*. The physical domain of the problem  $\Omega_{\text{phy}}$  is embedded in a fictitious domain  $\Omega_{\text{fict}}$  of primitive geometry. Their union forms the solution domain  $\Omega$  where the physical domain is described by the indicator function  $\alpha(\mathbf{x})$ . The axis aligned cells are only generated if they contain a physical contribution.

demanding mesh generation of discretizing the geometric domain while yielding high-order convergence rates on non-body-fitted meshes. So far, the FCM has been applied to a large variety of problems and geometric data. A review of the application of the FCM in different high-order approximation spaces like B-splines and NURBs for CAD-based models, in small and finite deformation analysis, local refinements and adaptivity, image-based geometric models, e.g. application to X-ray or computer tomography scans, can be found in [Schillinger and Ruess, 2015], as well as its application in fluid mechanics in [Xu et al., 2016]. Especially for image-based geometric models, the FCM profits from its functionality, since pixel- and voxel-based geometries have no surface description to which a mesh can be fitted. As a consequence, an intermediate step of generating a surface description of the image-based geometry is required, while the FCM requires neither the surface data nor the mesh generation.

## 2.2.2 Adaption of the weak formulation

The fundamental concept of the finite element method remains the same for the finite cell method. However, they differ in the finite-dimensional spaces of trial and weight functions which are redefined to serve the purpose of finding an approximation to the weak solution in

$$\begin{aligned}\mathcal{T}^h \subset \mathcal{T} &= \{u \mid u \in \mathcal{H}^1(\Omega_{\text{phy}}), u = \bar{u} \ \forall \mathbf{x} \in \Gamma_D\} \\ \mathcal{V}^h \subset \mathcal{V} &= \{v \mid v \in \mathcal{H}^1(\Omega_{\text{phy}}), v = 0 \ \forall \mathbf{x} \in \Gamma_D\}\end{aligned}\tag{2.42}$$

rather than in the Sobolev space on the unified domain  $\mathcal{H}^1(\Omega)$ . Nonetheless, the physical problem at hand is still solved on the unified domain of primitive geometry, which requires a geometric indication of whether a point is located in the physical or fictitious domain. To recover the embedded physical domain, an *indicator function*

$$\alpha(\mathbf{x}) = \begin{cases} 1 & \forall \mathbf{x} \in \Omega_{\text{phy}} \\ 0 \approx 10^{-\tau} & \forall \mathbf{x} \in \Omega_{\text{fict}} \end{cases}\tag{2.43}$$

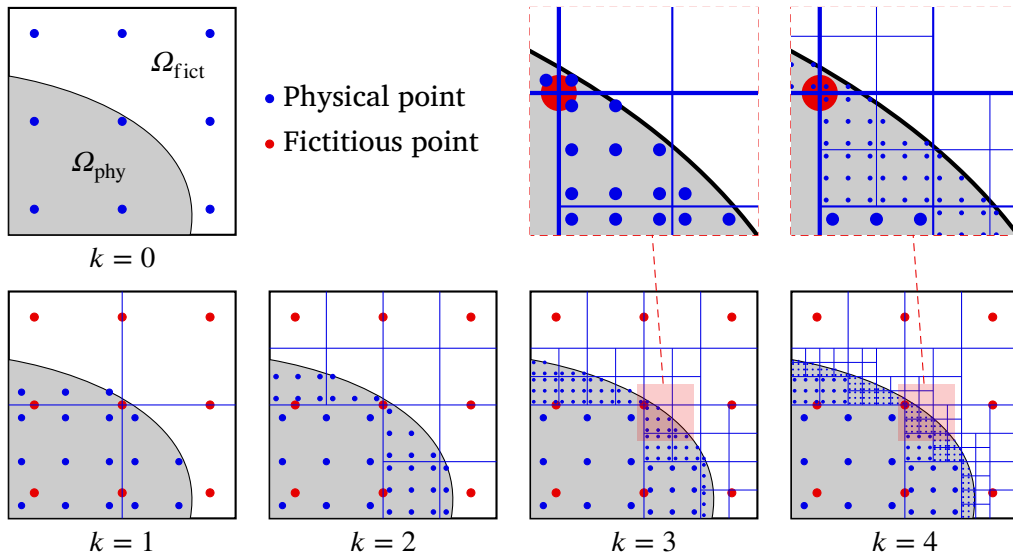


**Figure 2.13** Adaptive quadtree integration scheme showing the sub-cells for the tree depths  $k = 0, \dots, 4$ .

is introduced to the weak form where  $\tau$  is a positive integer ranging typically between  $\tau = 8, \dots, 14$ . While a zero-valued field on the fictitious domain yields mathematical validity of the concept, it causes a loss of numerical stability in the solving process of the algebraic equations due to an ill-conditioned system matrix [Parvizian et al., 2007, Düster et al., 2008]. Considering the weak form of stationary heat conduction, the bilinear and the linear functional change to

$$\mathcal{B}(v, u) := \int_{\Omega} \alpha \cdot \nabla v \cdot \kappa \cdot \nabla u \, d\Omega \quad (2.44a)$$

$$\mathcal{F}(v) := \int_{\Omega} \alpha \cdot v \cdot s \, d\Omega + \int_{\Gamma_D} v \cdot q \, d\Gamma + \int_{\Gamma_N} v \cdot \bar{q} \, d\Gamma. \quad (2.44b)$$

### 2.2.3 Integration of cut-cells

As previously introduced, one key challenge and the main computational demand is the integration of the element stiffness matrices. The indicator function produces discontinuous integrands in cut-cells for which an accurate numerical integration employing the Gaussian quadrature rule is not directly applicable [Hughes, 2012]. Different approaches have been proposed to tackle discontinuous integrands [Abedian et al., 2013], from which a simple yet effective method is commonly used in the FCM. Figure 2.13 shows this integration scheme based on so-called *quadtree* methods in two dimensions, where the cut-cells are recursively refined by bisection. The generally termed *spacetree* methods are based on the idea of *k-dimensional tree* or short *k-d tree* methods [De Berg, 2000]. To identify cut cells, a simple test of whether points are inside or outside the physical domain is sufficient to induce a bisection of the cell in

each direction leading to four (*quadtree* in 2D) or eight (*octree* in 3D) smaller sub-cells. These sub-cells are not local finite element refinements with additional shape functions, they only serve the purpose of generating a higher resolution of continuous integration domains along the boundary.

For the integration procedure of cut-cells, the fictitious domain is typically represented by the original quadrature points of the cell at  $k = 0$  multiplied by  $10^{-\tau}$  to retain numerical stability. The physical part of the cell is integrated by summing up all the integrals of the integration sub-cells over their physical quadrature points multiplied by  $1 - 10^{-\tau}$ . The general case of integrating an arbitrary integrand  $f(\mathbf{x})$  over a cut-cell then reads

$$\begin{aligned} \int_{\Omega_e} \alpha(\mathbf{x}) \cdot f(\mathbf{x}) d\Omega &= 10^{-\tau} \cdot \int_{\Omega_\xi} f(\mathbf{x}(\xi)) \cdot |\mathbf{J}(\xi)| d\Omega \\ &+ [1 - 10^{-\tau}] \cdot \sum_{i=1}^{n_e^{\text{sc}}} \int_{\Omega_\xi^i} f(\mathbf{x}(\xi)) \cdot |\mathbf{J}(\xi)| d\Omega \\ &\approx 10^{-\tau} \cdot \sum_{k=1}^{n_e^{\text{qp}}} f(\mathbf{x}(\xi_k)) \cdot |\mathbf{J}(\xi_k)| \cdot w_k \\ &+ [1 - 10^{-\tau}] \cdot \sum_{i=1}^{n_e^{\text{sc}}} \sum_{k=1}^{n_e^{\text{qp}}} f(\mathbf{x}(\xi(\zeta_k))) \cdot |\mathbf{J}(\xi(\zeta_k))| \cdot \tilde{w}_k \end{aligned} \quad (2.45)$$

where  $n_e^{\text{sc}}$  is the number of integration sub-cells in the cell and  $\Omega_\xi^i$  are the mapped reference domains of the integration sub-cells together with their mapped quadrature points  $\xi(\zeta_k)$  and weights  $\tilde{w}_k$ . For the sake of efficiency, sub-cells without a physical contribution, that is without physical quadrature points, are removed.

Since the boundary of the physical domain no longer necessarily coincides with the boundary of the cells, Dirichlet boundary conditions can no longer be prescribed at the corresponding degrees of freedom straightforwardly as in the conventional FEM. However, by employing penalty methods or using Lagrange multipliers, robustly the degrees of freedom can be constrained to weakly enforce the essential boundary conditions along the immersed boundary [Bathe, 2006]. This work will not make use of essential boundary conditions that do not coincide with the mesh boundary and therefore won't elaborate the weak enforcement further. For the established Nitsche method to tackle weakly enforced essential boundary conditions, the reader shall be referred to [Zander et al., 2012] in application to thermoelastic problems or [Hansbo, 2005, Nitsche, 1971] for deeper insights.



# Chapter 3

## Efficient integration of cut-cells

In Section 2.2 the finite cell method was introduced with its benefits of bypassing the mesh generation but also the upcoming challenge of accurate integration of the discontinuous integrands of the cut-cells. While the presented numerical integration of the cut-cells using an adaptive spacetree scheme is very robust and does not involve a complex implementation, it comes with a large number of quadrature points for sufficient accuracy. Hence, the system matrix integration becomes quite expensive, especially for complex or even porous geometric models. Over time, different proposals in various directions were made to increase the efficiency of the integration process.

In [Petö et al., 2020, Petö et al., 2021] is suggested to use methods from image compression to improve the adaptive spacetree. Sub-cells that are completely located in the physical domain are compressed which yields a much lower number of quadrature points. Another approach is to combine the adaptive spacetree with node relocations and high-order polynomials [Kudela et al., 2015, Kudela et al., 2016]. By doing so, the geometry is accurately represented with fewer recursive cycles and thereby naturally fewer quadrature points. Going in another direction, the authors of [Ventura, 2006, Ventura and Benvenuti, 2015, Abedian and Düster, 2019] propose to transform the discontinuous integrand to a smooth integrand through equivalent Legendre polynomials, such that the accuracy of the Gauss-Legendre quadrature rule is recovered.

Besides this selection of alternative integration schemes, another technique has been actively researched in the past. The so-called moment fitting quadrature rules are generally based on the idea of placing quadrature points arbitrarily, but typically uniformly or in the region of interest, and calculating their weight such that they are exact for a given polynomial order [Müller et al., 2013, Sudhakar and Wall, 2013]. Despite the adaptive spacetree approach, the moment fitting quadrature is used in this work to identify its efficiency potential in presented problems.

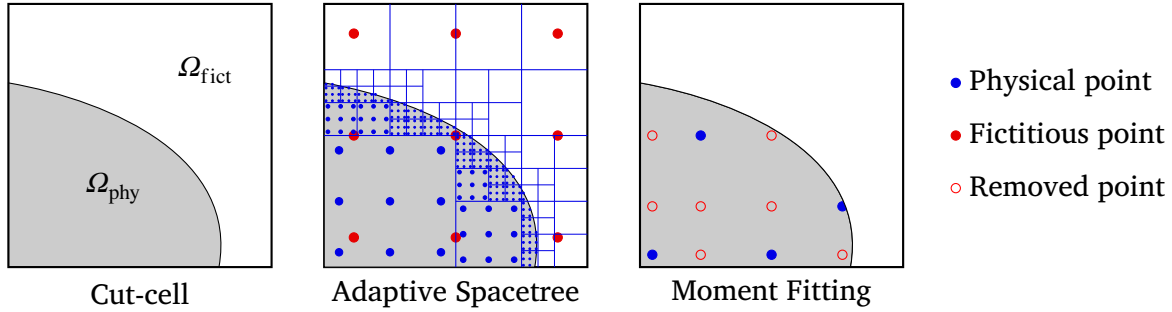


**Figure 3.1** Strategies to numerically integrate cut-cells. The initial point locations for the moment fitting quadrature are chosen to be  $5 \times 5$  Gauss-Legendre points here. Multiple quadrature points were identified as optimal while others were omittable and therefore removed.

### 3.1 Moment fitting quadrature

Considering the moment fitting approach in its most general form, the ultimate goal is to find the optimal set of quadrature points and corresponding weights that integrates the contributions of an element or cell exactly. It is sufficient for the fitting to integrate not the actual integrand regarding the physics, but any function of the same polynomial order. Thus, the integrand can be simply chosen to be the shape functions used to compute the governing integrals, e.g. (2.11) and (4.25), which are much cheaper to evaluate. As shown by [Joulaian et al., 2016], integrated Legendre polynomials and the moment fitting equations work well together. Mathematically spoken, the nonlinear problem

$$\mathbf{A} \cdot \mathbf{w} = \mathbf{b}$$

$$\begin{bmatrix} N_1(\xi_1) & \dots & N_1(\xi_i) & \dots & N_1(\xi_n) \\ \vdots & \ddots & \vdots & & \vdots \\ N_j(\xi_1) & \dots & N_j(\xi_i) & \dots & N_j(\xi_n) \\ \vdots & & \vdots & \ddots & \vdots \\ N_m(\xi_1) & \dots & N_m(\xi_i) & \dots & N_m(\xi_n) \end{bmatrix} \cdot \begin{bmatrix} w_1 \\ \vdots \\ w_i \\ \vdots \\ w_n \end{bmatrix} = \begin{bmatrix} \int_{\Omega_e} N_1(\xi) d\Omega \\ \vdots \\ \int_{\Omega_e} N_j(\xi) d\Omega \\ \vdots \\ \int_{\Omega_e} N_m(\xi) d\Omega \end{bmatrix} \quad (3.1)$$

shall be solved for the number  $n$ , the position  $\xi_i$  and the weight  $w_i$  of an optimal quadrature set  $\{\xi_i, w_i\}$ ,  $i = 1, \dots, n$  which integrate the shape functions  $N_j(\xi)$  over  $\Omega_e$  exactly. The vector  $\mathbf{b}$  contains the integrals of the shape function which are called *moments*. The coefficient matrix  $\mathbf{A}$  is non-symmetric and in general non-square. To simplify the solution process, the system can be linearized by predetermining the quadrature point locations. Now, the system's unknowns are only the weights in  $\mathbf{w}$  which are to be determined individually for the cut cells.

For linear problems, several versions of the moment fitting quadrature have been applied to the finite cell method [Joulaian et al., 2016, Hubrich and Düster, 2019, Düster and Hubrich, 2020, Düster and Allix, 2020]. Following the idea of the FCM, the moment

fitting is subjected to quadrature points which are only distributed in the physical domain followed by a linear least square solver to provide the weights. Using Gauss-Legendre quadrature points and allowing them to be also present in the fictitious domain results in well-conditioned moment fitting equations even for high-order functions. However, applied to nonlinear problems, the moment fitting quadrature turns out to worsen the stability of the governing nonlinear solution procedure, caused by the existence of generated integration points with negative weights. Applied to the Newton-Raphson method, the solution diverges during the incremental-iterative procedure. In [Hubrich and Düster, 2019, Düster and Allix, 2020], an adaptive version of the moment fitting scheme is applied together with adaptive spacetime where the moment fitting is either applied on a cell or sub-cell depending on the volume fraction of the cut-cell. While the robustness was improved, the number of generated quadrature points through the moment fitting was too large compared to standard moment fitting. In [Huybrechs, 2009], the author suggests constraining the solution of the moment fitting (3.1) to be strictly positive. This *non-negative moment fitting* was originally proposed in one-dimensional space but recently got extended to two [Legrain, 2021] and three dimensions [Garhuom and Düster, 2022].

### 3.1.1 Non-negative moment fitting

According to *Tchakaloff's theorem* [Tchakaloff, 1957], the nonlinear moment fitting equation (3.1) has solutions with  $n = m$  quadrature points on  $\Omega_e$  and all positive weights [Davis, 1967, Davis, 1969]. Due to the introduced linearization using fixed Gauss-Legendre points, it may not be possible to find those solutions. However, within the linear moment fitting equation, it is still possible to find  $n \geq m$  points with positive weights [Davis, 1969, Huybrechs, 2009]. Aiming for those points, equation (3.1) is minimized subject to inequality constraints enforcing non-negative weights, which yields the *non-negative least square problem*

$$\begin{aligned} \min \quad & \| \mathbf{A} \cdot \mathbf{w} - \mathbf{b} \|_2 \\ \text{subject to} \quad & w_i \geq 0, \quad i = 1, \dots, n. \end{aligned} \tag{3.2}$$

Optimization solvers like TRON (trust region newton method) could be employed to solve the problem, but provide *non-sparse* solutions and require a large number of quadrature points  $n \gg m$  to ensure the existence of a positive solution. The term *sparse* in this context implies a solution with close or equal to  $m$  quadrature points. The existence of *sparse* solutions has been proven, provided that  $n$  is sufficiently large [Davis, 1967]. Davis' theorem says that if a quadrature rule of order  $p$  exists with  $n \geq m$  points and non-negative weights  $w_i \geq 0$ , then a quadrature rule of same order  $p$  and with the same points exists, which has only  $n = m$  non-zero and positive weights  $w_i > 0$ .

To solve the problem, the non-negative least square solver (NNLS) proposed by [Lawson and Hanson, 1995] has been proven to be convergent, finite and provides a *sparse*

solution [Legrain, 2021, Garhuom and Düster, 2022]. The solver is based on an *active set* strategy which approaches the inequality-constrained problem (3.2) by identifying the active constraints in the set of all inequality constraints. If the active constraints are known, they can be expressed as equality constraints. Equality-constrained problems are much simpler to treat and can be solved by means of Lagrange multipliers. As shown in Algorithm 3.1, the NNLS introduces a passive set  $\mathcal{P}$  and an active set  $\mathcal{A}$  which contain the indices corresponding to the unknown weights in  $\mathbf{w}$ . An index can either be exclusively in  $\mathcal{P}$  or  $\mathcal{A}$ . Weights that are indexed in  $\mathcal{P}$  can take arbitrary values, but will be corrected during the iterations if they become negative. All the weights which are indexed in  $\mathcal{A}$  are set to zero. The Lagrange multipliers are computed by

$$\mathbf{v} = \mathbf{A}^\top \cdot [\mathbf{b} - \mathbf{A} \cdot \mathbf{w}] \quad (3.3)$$

and the goal of the algorithm is to converge to the state

$$\begin{aligned} v_j &= 0 \quad \forall j \in \mathcal{P} \quad \wedge \quad v_j < 0 \quad \forall j \in \mathcal{A} \\ w_j &> 0 \quad \forall j \in \mathcal{P} \quad \wedge \quad w_j = 0 \quad \forall j \in \mathcal{A} \end{aligned} \quad (3.4)$$

such that all weights which are indexed in  $\mathcal{P}$  are positive while all weights in  $\mathcal{A}$  are zero and can be filtered out. The sets are initialized with  $\mathcal{P} = \emptyset$  and  $\mathcal{A} = 1, \dots, n$ , hence all indices are in the active set. The algorithm then successively picks the maximum Lagrange multiplier indexed in the active set and moves it from the active to the passive set until all Lagrange multipliers are smaller or equal to zero. To reach convergence, the weights are modified as follows. An auxiliary vector  $\mathbf{z}$  is split into its entries which are indexed in the passive set  $\mathbf{z}^{\mathcal{P}}$  and in the active set  $\mathbf{z}^{\mathcal{A}}$ . First, the passive part is computed by solving

$$\begin{aligned} \mathbf{A}^{\mathcal{P}} \cdot \mathbf{z}^{\mathcal{P}} &= \mathbf{b} \\ \mathbf{Q} \cdot \mathbf{R} \cdot \mathbf{z}^{\mathcal{P}} &= \mathbf{b} \\ \mathbf{Q}^\top \cdot \mathbf{Q} \cdot \mathbf{R} \cdot \mathbf{z}^{\mathcal{P}} &= \mathbf{Q}^\top \cdot \mathbf{b} \\ \mathbf{R} \cdot \mathbf{z}^{\mathcal{P}} &= \mathbf{Q}^\top \cdot \mathbf{b} \end{aligned} \quad (3.5)$$

employing the QR-factorization with  $\mathbf{Q}$  being an orthogonal matrix ( $\mathbf{Q}^\top \mathbf{Q} = \mathbf{I}$ ) and  $\mathbf{R}$  a right triangular matrix [Lawson and Hanson, 1995]. The passive coefficient matrix  $\mathbf{A}^{\mathcal{P}}$  contains the columns that are indexed in the passive set. The active part of the auxiliary vector is  $\mathbf{z}^{\mathcal{A}} = \mathbf{0}$  and unified with the passive part, denoted by  $\mathbf{z} = \mathbf{z}^{\mathcal{P}} \cup \mathbf{z}^{\mathcal{A}}$ . To update the weights, a scaling factor  $0 < \beta \leq 1$  is considered

$$\mathbf{w} = \mathbf{w} + \beta \cdot [\mathbf{z} - \mathbf{w}] \quad (3.6)$$

which is computed based on the largest negative value in  $\mathbf{z}^{\mathcal{P}}$

$$\beta = \min \left\{ \frac{w_i}{w_i - z_i}, \forall i \in \mathcal{P} \wedge \forall z_i \leq 0 \right\}. \quad (3.7)$$

After that, all non-positive weights  $w_j \leq 0$  are moved from the passive to the active set and the update scheme iterates until all values of  $\mathbf{z}^{\mathcal{P}}$  are non-positive. If this is fulfilled, the Lagrange multipliers are updated by (3.3) and the next maximum entry of  $\mathbf{z}^{\mathcal{A}}$  is considered to move into  $\mathcal{P}$  until the maximum Lagrange multiplier is not larger than a user-defined tolerance  $\epsilon \approx 0$  or the active set is empty.

---

**Algorithm 3.1** Non-negative least square solver (NNLS) of [Lawson and Hanson, 1995] with coefficient matrix  $\mathbf{A} \in \mathbb{R}^{m \times n}$ , moments  $\mathbf{b} \in \mathbb{R}^{m \times 1}$  and tolerance  $0 < \epsilon \lll 1$  as input variables. The auxiliary vector  $\mathbf{z} = \mathbf{z}^{\mathcal{P}} \cup \mathbf{z}^{\mathcal{A}}$  holds a passive and an active part with corresponding indices of the weights  $\mathbf{w}$ .

---

```

1  $\mathbf{w} = \mathbf{0}, \mathbf{z} = \mathbf{0}, \mathcal{P} = \emptyset, \mathcal{A} = \{1, \dots, n\}$ 
2  $\mathbf{v} = \mathbf{A}^T \cdot [\mathbf{b} - \mathbf{A} \cdot \mathbf{w}]$ 
3 while  $\mathcal{A} \neq \emptyset \wedge \max\{v_i, i = 1, \dots, n\} > \epsilon$ 
4   Find  $j \in \mathcal{A}$  of  $\max\{v_j, j = 1, \dots, n\}$ 
5   Move  $j$  from  $\mathcal{A}$  to  $\mathcal{P}$ 
6    $\mathbf{z}^{\mathcal{P}} = \mathbf{0}$ 
7   while  $\min\{z_i^{\mathcal{P}}, i \in \mathcal{P}\}$ 
8      $\mathbf{A}^{\mathcal{P}} = A_{ij}, i = 1, \dots, m, j \in \mathcal{P}$ 
9      $\mathbf{A}^{\mathcal{P}} \cdot \mathbf{z}^{\mathcal{P}} = \mathbf{b} \rightarrow \mathbf{R} \cdot \mathbf{z}^{\mathcal{P}} = \mathbf{Q}^T \cdot \mathbf{b}$ 
10     $\mathbf{z} = \mathbf{z}^{\mathcal{P}} \cup \mathbf{z}^{\mathcal{A}}, \mathbf{z}^{\mathcal{A}} = \mathbf{0}$ 
11    if  $z_j^{\mathcal{P}} > 0, \forall j \in \mathcal{P}$ 
12       $\mathbf{w} = \mathbf{z}$ 
13      break
14    endif
15     $\beta = \min \left\{ \frac{w_i}{w_i - z_i}, \forall i \in \mathcal{P} \wedge \forall z_i \leq 0 \right\}, \beta \in [0, 1]$ 
16     $\mathbf{w} = \mathbf{w} + \beta \cdot [\mathbf{z} - \mathbf{w}]$ 
17    Find every  $j \in \mathcal{P}$  of  $w_j \leq 0, j = 1, \dots, n$ 
18    Move every  $j$  from  $\mathcal{P}$  to  $\mathcal{A}$ 
19  endwhile
20   $\mathbf{v} = \mathbf{A}^T \cdot [\mathbf{b} - \mathbf{A} \cdot \mathbf{w}]$ 
21 endwhile

```

---

### 3.1.2 Adaptive algorithm

Whether the non-negative moment fitting employing the NNLS from Algorithm 3.1 results in an accurate and *sparse* quadrature rule is dominantly influenced by the distribution of tentative quadrature points in the physical domain. If the number of tentative quadrature points is too low, there might not be a chance to find non-negative weights for the given locations and if it is too large, the computational effort of solving the constrained least square problem outruns the efficiency benefit of the whole method. Hence, the tentative set of quadrature points shall be chosen carefully. The approach of [Garhuom and Düster, 2022] is followed in this work and suggests applying an adaptive scheme based on the adaptive spacetree (AST) to find a suitable set of tentative Gauss-Legendre points. This set with  $n$  points should be larger than the number of moments  $m$  to obtain convergence [Legrain, 2021], where  $m$  is determined by the polynomial degree of the shape functions with  $m = (p + 1)^d$ .

**Algorithm 3.2** Non-negative moment fitting (NNMF) using an adaptive algorithm for each cut-cell based on an adaptive spacetree (AST) [Garhuom and Düster, 2022]. The tree depth of the standard adaptive spacetree  $k_{\text{AST}}$ , the tolerance  $0 < \epsilon \lll 1$ , the factor  $L$ , the maximum number of Gauss-Legendre points per sub-cell  $n_{\max}^{\text{GL}}$  and the loop limits  $i_{\max}$  and  $j_{\max}$  are user-defined input values.

---

```

1   $m = [p + 1]^d$ 
2  Apply AST with  $k_{\text{AST}}$  and  $\left[\frac{p+1}{2}\right]^d$  G.-L. points per sub-cell on  $\Omega_{\text{phy}}$ 
3  Integrate moments  $\mathbf{b}$  from AST
4   $r = 0$ ,  $k_{\text{NNMF}} = 0$ ,  $i = 0$ ,  $j = 0$ 
5  while  $\|\mathbf{r}\|_2 > \epsilon \wedge j \leq j_{\max}$ 
6     $r = r + 1$ ,  $i = i + 1$ 
7     $n^{\text{GL}} = \min \left\{ r \cdot \frac{p+1}{2}, n_{\max}^{\text{GL}} \right\}$ 
8    Apply AST with  $k_{\text{NNMF}}$  and  $[n^{\text{GL}}]^d$  G.-L. points per sub-cell on  $\Omega_{\text{phy}}$ 
9    Get total number of quadrature points  $n$ 
10   if  $n < L \cdot m \wedge i < i_{\max}$ 
11     if  $n^{\text{GL}} = n_{\max}^{\text{GL}} \wedge k_{\text{NNMF}} < k_{\text{AST}}$ 
12        $k_{\text{NNMF}} = k_{\text{NNMF}} + 1$ 
13        $r = 6$ 
14     endif
15     continue
16   endif
17    $j = j + 1$ 
18   Assemble coefficient matrix  $\mathbf{A} \in \mathbb{R}^{m \times n}$ 
19   Solve  $\mathbf{A} \cdot \mathbf{w} = \mathbf{b}$  with Algorithm 3.1
20    $\|\mathbf{r}\|_2 = \|\mathbf{A} \cdot \mathbf{w} - \mathbf{b}\|_2$ 
```

---

```

21 endwhile
22 Remove every quadrature point and weight  $\{\xi_i, w_i\}$  for which  $w_i = 0, i = 1, \dots, n$ 

```

---

The proposed adaptive algorithm is shown in Algorithm 3.2 and starts with the computation of the moments  $\mathbf{b}$  using the adaptive spacetree integration scheme with

$$n = \left[ \frac{p+1}{2} \right]^d \quad (3.8)$$

Gauss-Legendre quadrature points, which can integrate a polynomial up to order  $p$  exactly. To build the coefficient matrix  $\mathbf{A}$ , the first try is to apply the AST with  $k_{\text{NNMF}} = 0$  and  $r \cdot [(p+1)/2]^d$  Gauss-Legendre points in the physical domain. To ensure a sufficiently large number of tentative quadrature points,  $r$  is increased until a minimum of  $n \geq L \cdot m$  points is obtained. The factor  $L$  should be in the range of  $3, \dots, 6$ . If a maximum number of quadrature points per sub-cell  $n_{\max}^{\text{GL}}$  is reached, but  $n$  is still  $< L \cdot m$ , the tree depth of the AST  $k_{\text{NNMF}}$  is increased as well up to  $k_{\text{NNMF}} = k_{\text{AST}}$  and  $r$  is reset to 6. After reaching a sufficiently large tentative set of quadrature points, the system  $\mathbf{A} \cdot \mathbf{w} = \mathbf{b}$  is solved by Algorithm 3.1 for the non-negative weights. If the residual norm  $\|\mathbf{r}\|_2 = \|\mathbf{A} \cdot \mathbf{w} - \mathbf{b}\|_2$  of the least square problem (3.2) is smaller than the user-defined tolerance  $\varepsilon \approx 0$ , the quadrature rule is considered to be converged. If the residual norm is too large,  $r$  is further increased and  $\mathbf{A}$  is rebuilt with more quadrature points. By defining the variables  $i_{\max}$  and  $j_{\max}$ , the number of NNLS applications and the number of increments of  $r$  can be limited. In a successful application of the algorithm, *Tchakaloff's theorem* is satisfied and the NNLS returns a *sparse* vector where many quadrature points  $w_j = 0, \forall j \in \mathcal{A}$  are filtered out. It shall be noted that an increase in the number of tentative quadrature points does not increase the cost of the final moment fitting quadrature rule since the algorithm will always find the  $n = m$  best quadrature points. Although it contradicts *Tchakaloff's theorem*, there eventually will be cases with even  $n < m$  due to the numerical tolerances used in the algorithm [Legrain, 2021].

## 3.2 Numerical results

To show the concept of the non-negative moment fitting quadrature and verify its implementation two small tests on a unit cell are presented.

### 3.2.1 Recovery of the Gauss-Legendre quadrature

To work properly, the moment fitting quadrature rule should recover the Gauss-Legendre weights if the Gauss-Legendre point locations are used as initial coordinates. This recovery is modeled for different polynomial integrands of order  $p$  on an uncut unit cell given  $[p+1]^3$  Gauss-Legendre points. Figure 3.2 depicts the error of the moment

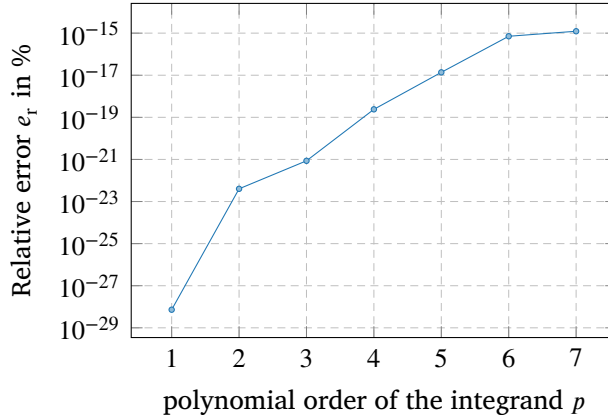


**Figure 3.2** Relative error of the quadrature points obtained from non-negative moment fitting given an uncut unit cell with  $n = (p + 1)^3$  standard Gauss-Legendre points. The moment fitting can recover the Gauss-Legendre weights up to machine precision.

fitting weights  $w_i^{\text{MF}}$  to the standard Gauss-Legendre weights  $w_i^{\text{GL}}$  over the polynomial order of the integrand. The error is defined as

$$e_w = \frac{1}{n} \cdot \sqrt{\sum_{i=1}^{(p+1)^3} \left[ \frac{w_i^{\text{GL}} - w_i^{\text{MF}}}{w_i^{\text{GL}}} \right]^2}. \quad (3.9)$$

As the graph depicts, the Gauss-Legendre weights are recovered up to machine precision by the non-negative moment fitting rule described in this section. The quadrature rule shows an increase in the error for higher order integrands. However, the error is at  $10^{-15}\%$  at  $p = 7$  which still has no significant impact on numerical computations.

### 3.2.2 Sphere-cut unit cell

Since the non-negative moment fitting rule shall be applied on cut-cells, a single unit cell with  $\mathbf{x} \in [0, 1]^3$  is considered with a spherical indicator function  $\alpha(\mathbf{x}) = \|\mathbf{x}\| \leq 1.55$  to test the accuracy and reduction of quadrature points for different polynomial integrands. Figure 3.3 depicts the indicator that cuts a corner of the unit cell. Using the spacetree quadrature technique with a tree depth of  $k = 5$  on a shape function space with  $p = 6$ , a total of 48 250 physical quadrature points is generated to integrate the single cell, even though only a fairly small area is affected by the cut. As one can even visually assess, the non-negative moment fitting accomplishes the same quadrature setup for the cell with far fewer quadrature points, that is a number of 175 physical points. Naturally, the moment fitting is a computationally more expensive setup of the quadrature and in this case, takes around 6.5 times the time required by the spacetree quadrature. In linear analyses where the equations only have to be integrated once, the moment fitting would not be a smart choice in this case. However, as it will be demonstrated later on in this work, in nonlinear analysis where the equations have to be integrated over

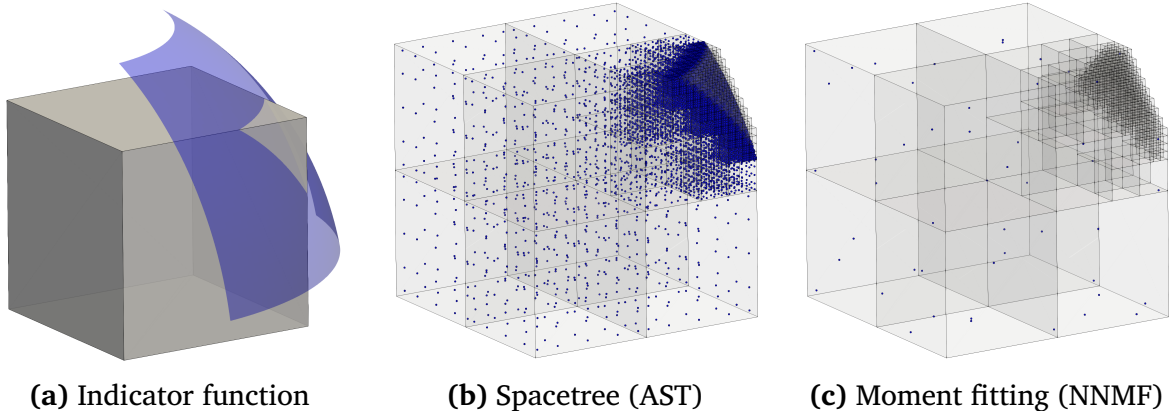


**Figure 3.3** Quadrature points of the unit cell with  $p = 6$  basis. The cell with domain  $\mathbf{x} \in [0, 1]^3$  is cut by a sphere with radius 1.55. The AST uses 48 250 and the NNMF 175 physical points.

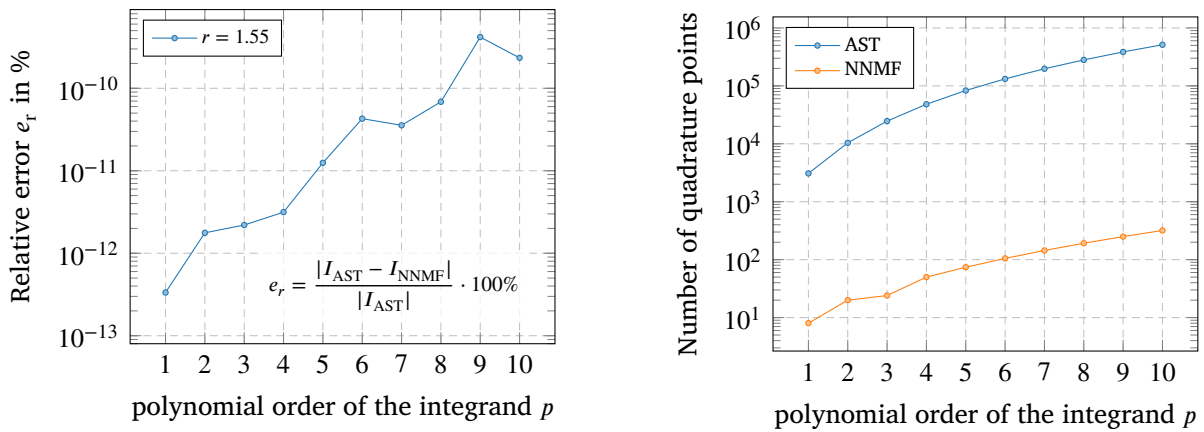


**Figure 3.4** Relative error of the integral computed by the non-negative moment fitting quadrature (NNMF) to the integral computed via an adaptive spacetree decomposition (AST).

and over again in the linearized steps, the efficiency of having fewer quadrature points trades off their expensive setup. Figure 3.4 shows the relative error of the integral value between the spacetree and moment fitting quadrature where a similar behavior can be seen as for the Gauss-Legendre point recovery. The error increases with increasing polynomial order of the integrand but is still only at around  $4 \cdot 10^{-10}\%$  for a polynomial integrand of order  $p = 10$ . On the right-hand side of Figure 3.4, the number of points required for the spacetree quadrature is constantly around 2.5 - 3 orders of magnitude larger than the number of points required by the non-negative moment fitting for the respective polynomial order of the integrand.



# Chapter 4

## Linear thermoelasticity

After stating the fundamental principles of finite elements, this chapter introduces the coupling of different solution fields. The multi field problem will be the phenomenon of linear thermoelasticity, where the thermal field holds the temperature  $T$  and the elastic field the displacement  $\mathbf{u}$  as the unknown variable.

### 4.1 Linear elasticity

Before introducing the multi field coupling, the theory of linear elasticity shall be presented [Anand and Govindjee, 2020, Sadd, 2009]. In continuum mechanics, linear elasticity is widely used due to its simplicity in the theory and application as well as its accuracy in the framework of its assumptions.

#### 4.1.1 Kinematics of deformation

To describe the deformation of a body over time, an initial and typically unstressed configuration of the body is taken as the *reference configuration* at time zero denoted by  $\Omega$ . A point in  $\Omega$  shall be called *material point* and is characterized by its position vector  $\mathbf{x}$ . The single coordinates of the material point are obtained by the scalar product  $x_i = \mathbf{e}_i \cdot \mathbf{x}$ , where  $\mathbf{e}_i$ ,  $i = 1, 2, 3$  are the three mutually orthogonal unit base vectors of the three-dimensional Cartesian coordinate system. At a later instant in time, the material point  $\mathbf{x} \in \Omega$  would have moved to another position  $\hat{\mathbf{x}}$  in the *deformed configuration* or *instant configuration*  $\hat{\Omega}$ . The deformed components of the material point are now  $\hat{x}_i = \mathbf{e}_i \cdot \hat{\mathbf{x}}$ . The motion the continuum during the deformation of the body at time instant  $t$  follows the mathematical description of a *deformation mapping*

$$\hat{\mathbf{x}} = \chi(\mathbf{x}, t), \quad \chi(\mathbf{x}, 0) = \mathbf{x}, \quad \mathbf{x} = \chi^{-1}(\hat{\mathbf{x}}, t). \quad (4.1)$$

The *displacement vector* of  $\mathbf{x}$  follows from the mapping with

$$\mathbf{u}(\mathbf{x}, t) = \hat{\mathbf{x}} - \mathbf{x} = \chi(\mathbf{x}, t) - \mathbf{x}. \quad (4.2)$$

Considering a material point  $P \in \Omega$  at  $\mathbf{x}$  and a point  $Q \in \Omega$  neighboring  $P$ , then the position of  $Q$  reads  $\mathbf{x} + \Delta\mathbf{x}$  with  $\Delta\mathbf{x}$  being the vector connecting  $P$  and  $Q$ . Consequently, the material points in the deformed configuration are  $\hat{P} \in \hat{\Omega}$  at  $\hat{\mathbf{x}}$  and  $\hat{Q} \in \hat{\Omega}$  at  $\hat{\mathbf{x}} + \Delta\hat{\mathbf{x}}$ . Assuming that the vectors  $\Delta\mathbf{x}$  and  $\Delta\hat{\mathbf{x}}$  are infinitesimally small, then they can be expressed by  $d\mathbf{x}$  and  $d\hat{\mathbf{x}}$  which allows

$$\begin{aligned} \hat{\mathbf{x}} + d\hat{\mathbf{x}} &= \mathbf{x} + d\mathbf{x} + \mathbf{u}(\mathbf{x} + d\mathbf{x}) \\ d\hat{\mathbf{x}} &= [\mathbf{x} - \hat{\mathbf{x}}] + d\mathbf{x} + \mathbf{u}(\mathbf{x} + d\mathbf{x}) \\ d\hat{\mathbf{x}} &= d\mathbf{x} + [\mathbf{u}(\mathbf{x} + d\mathbf{x}) - \mathbf{u}(\mathbf{x})] \\ d\hat{\mathbf{x}} &= d\mathbf{x} + d\mathbf{u} \end{aligned} \quad (4.3)$$

where a Taylor series expansion around  $P$ , which neglects higher-order terms, can approximate  $\mathbf{u}(\mathbf{x} + d\mathbf{x}) = \mathbf{u}(\mathbf{x}) + d\mathbf{u} \approx \mathbf{u}(\mathbf{x}) + \nabla\mathbf{u} \cdot d\mathbf{x}$  which leads to

$$\begin{aligned} d\hat{\mathbf{x}} &= d\mathbf{x} + \nabla\mathbf{u} \cdot d\mathbf{x} \\ d\hat{\mathbf{x}} &= [\nabla\mathbf{u} + \mathbf{I}] \cdot d\mathbf{x} \\ d\hat{\mathbf{x}} &= \mathbf{F} \cdot d\mathbf{x} \end{aligned} \quad (4.4)$$

introducing the *deformation gradient* tensor

$$\mathbf{F}(\mathbf{x}, t) = \nabla\chi = \frac{\partial\chi}{\partial\mathbf{x}} = \frac{\partial}{\partial\mathbf{x}}[\mathbf{u} + \mathbf{x}] = \nabla\mathbf{u} + \mathbf{I} = \mathbf{H} + \mathbf{I} \quad (4.5)$$

wherein the *displacement gradient* tensor is

$$\mathbf{H}(\mathbf{x}, t) = \nabla\mathbf{u} = \frac{\partial\mathbf{u}}{\partial\mathbf{x}} = \mathbf{F} - \mathbf{I}. \quad (4.6)$$

The deformation gradient  $\mathbf{F}$  composes a rigid rotation of the body and a deformation part which induces strain in the body. Therefore, it is convenient to define strain measures that use a rotation-independent tensor. Since a rotation  $\mathbf{R}$  multiplied with its transpose yields no rotation, namely  $\mathbf{R}\mathbf{R}^T = \mathbf{R}^T\mathbf{R} = \mathbf{I}$ , the deformation gradient tensor can be made rotation-independent by multiplying  $\mathbf{F}$  with its transpose. This leads to the most popular strain measure in solid mechanics, the (*right*) *Cauchy-Green deformation gradient* tensor [Green, 1839]

$$\mathbf{U}^2 = \mathbf{F}^T \mathbf{F}. \quad (4.7)$$

This tensor can be reestablished by defining the *Green-Lagrange finite strain tensor* from the fundamental definition of strain being a measure on how much a displacement differs locally from a rigid body displacement. Mathematically, this means that difference

between  $d\mathbf{x}$  and  $d\hat{\mathbf{x}}$  is taken, or more specifically their square to eliminate directional influence, which yields

$$\begin{aligned} d\hat{\mathbf{x}}^\top d\hat{\mathbf{x}} - d\mathbf{x}^\top d\mathbf{x} &= [\mathbf{F}d\mathbf{x}]^\top \mathbf{F}d\mathbf{x} - d\mathbf{x}^\top d\mathbf{x} \\ &= d\mathbf{x}^\top \mathbf{F}^\top \mathbf{F}d\mathbf{x} - d\mathbf{x}^\top d\mathbf{x} \\ &= d\mathbf{x}^\top [\mathbf{F}^\top \mathbf{F} - \mathbf{I}]d\mathbf{x} \\ &= d\mathbf{x}^\top [\mathbf{U}^2 - \mathbf{I}]d\mathbf{x} \end{aligned} \quad (4.8)$$

where the *Green-Lagrange finite strain tensor* is defined by

$$\begin{aligned} 2\mathbf{E} &:= \mathbf{U}^2 - \mathbf{I} \\ \mathbf{E} &= \frac{1}{2}[\mathbf{U}^2 - \mathbf{I}] = \frac{1}{2}[\mathbf{F}^\top \mathbf{F} - \mathbf{I}] = \frac{1}{2}[\mathbf{H} + \mathbf{H}^\top + \mathbf{H}^\top \mathbf{H}] \end{aligned} \quad (4.9)$$

Note that for a pure rotation  $\mathbf{E}$  vanishes, since then  $\mathbf{F}^\top \mathbf{F} = \mathbf{I}$ . In linear elasticity, the assumption is made that the deformations will be small in a sense that the displacement gradient  $\mathbf{H}$  will be small. Following this, the *finite strain tensor* can be linearized by neglecting the higher order term to get the *infinitesimal strain tensor* or *small strain tensor*

$$\boldsymbol{\epsilon} := \text{Lin}_x \mathbf{E}(\mathbf{H}) = \frac{1}{2}[\mathbf{H} + \mathbf{H}^\top] = \frac{1}{2}[\nabla \mathbf{u} + [\nabla \mathbf{u}]^\top] = \nabla^{\text{sym}} \mathbf{u}. \quad (4.10)$$

where  $\nabla^{\text{sym}}(\bullet) = \mathbf{I}^{\text{sym}} : \nabla(\bullet)$  is the symmetric part of the gradient of  $(\bullet)$ , see (5.90).

### 4.1.2 Balance of forces and momentum

According to *Newton's second law of motion*, the temporal change of the linear momentum  $m \cdot \dot{\mathbf{x}}$ , defined by mass and velocity of the particle at  $\mathbf{x}$ , is equal to the vector sum of all occurring forces acting on the body [Goldstein et al., 2002]. Various types of forces can act on the body which can be categorized in body forces  $\mathbf{b}$  acting on the internal domain of  $\Omega$  and traction forces  $\mathbf{t}$  acting on the boundary  $\Gamma = \partial\Omega$  of the body. Mathematically spoken, the balance equation reads

$$\frac{\partial}{\partial t} \left[ m \cdot \frac{\partial \mathbf{x}}{\partial t} \right] = \int_{\Omega} \mathbf{b} d\Omega + \int_{\Gamma} \mathbf{t} d\Gamma. \quad (4.11)$$

Cauchy's theorem of stress postulates the existence of a stress tensor  $\boldsymbol{\sigma}$  which can express the traction forces acting on any surface of the continuum by means of the surface normal vector  $\mathbf{n}$

$$\mathbf{t} = \boldsymbol{\sigma} \cdot \mathbf{n} \quad (4.12)$$

where the *Cauchy stress tensor* holds the normal stresses  $\sigma_{ii}$  and shear stresses  $\sigma_{ij}$ ,  $i \neq j$  in a second order tensor

$$\boldsymbol{\sigma} = \begin{bmatrix} \sigma_{11} & \sigma_{12} & \sigma_{13} \\ \sigma_{21} & \sigma_{22} & \sigma_{23} \\ \sigma_{31} & \sigma_{32} & \sigma_{33} \end{bmatrix}, \quad \boldsymbol{\sigma} = \boldsymbol{\sigma}^\top. \quad (4.13)$$

The symmetry originates from the conservation of angular momentum [Anand and Govindjee, 2020]. The differential equation of motion (4.11) can now be rewritten in terms of stresses

$$\frac{\partial}{\partial t} \left[ m \cdot \frac{\partial \mathbf{x}}{\partial t} \right] = \int_{\Omega} \mathbf{b} d\Omega + \int_{\Gamma} \boldsymbol{\sigma} \cdot \mathbf{n} d\Gamma. \quad (4.14)$$

In the case of an elastostatic consideration, the temporal change of linear moment equals zero, which will be assumed throughout this work. Further, the *divergence theorem* can be applied to the integrals such that

$$\int_{\Omega} [\nabla \cdot \boldsymbol{\sigma} + \mathbf{b}] d\Omega = 0. \quad (4.15)$$

Naturally, in order to satisfy the equilibrium, the integrand has to be zero in order for the integral to be zero

$$\nabla \cdot \boldsymbol{\sigma} + \mathbf{b} = \mathbf{0}, \quad \forall \mathbf{x} \in \Omega. \quad (4.16)$$

This local form of the *stationary conservation of momentum* needs to be accompanied by a constitutive relation which represents the material behavior of the body in order to relate the kinematics and kinetics of the problem.

### 4.1.3 Constitutive relation

For the case of linear elasticity, *Hooke's law* is generalized to the spatial dimension in order to relate the strain  $\boldsymbol{\epsilon}$  and stresses  $\boldsymbol{\sigma}$

$$\boldsymbol{\sigma} = \mathbf{C} : \boldsymbol{\epsilon} \quad (4.17)$$

where  $\mathbf{C}$  is a fourth order tensor describing the material behavior. For isotropic homogeneous material, the tensor is symmetric and specified by Young's modulus  $E$  and the Poisson ratio  $\nu$

$$\mathbf{C} = \lambda \mathbf{I} \otimes \mathbf{I} + 2\mu \mathbf{I}^{\text{sym}}, \quad \text{with } \mu = \frac{E}{2(1+\nu)} \text{ and } \lambda = \frac{E\nu}{(1+\nu)(1-2\nu)} \quad (4.18)$$

where  $\mathbf{I}$  are second order identity tensors and  $\mathbf{I}^{\text{sym}}$  is the symmetric fourth order identity tensor, see (5.90). Since the stress tensor  $\boldsymbol{\sigma}$  is symmetric, often only the unique stresses are stored for the sake of simplicity. The so-called *Voigt notation* rewrites the second order tensors  $\boldsymbol{\sigma}$  and  $\boldsymbol{\epsilon}$  into vectors

$$\boldsymbol{\epsilon}^T = [\epsilon_{11} \ \epsilon_{22} \ \epsilon_{33} \ \epsilon_{12} \ \epsilon_{23} \ \epsilon_{13}]^T, \quad \boldsymbol{\sigma}^T = [\sigma_{11} \ \sigma_{22} \ \sigma_{33} \ \sigma_{12} \ \sigma_{23} \ \sigma_{13}]^T \quad (4.19)$$

such that the constitutive equation can be written in matrix-vector notation

$$\boldsymbol{\sigma} = \mathbf{C} \cdot \boldsymbol{\epsilon} \quad (4.20)$$

with  $\mathbf{C}$  being a matrix now, containing the material parameters

$$\mathbf{C} = \begin{bmatrix} a & b & b & 0 & 0 & 0 \\ b & a & b & 0 & 0 & 0 \\ b & b & a & 0 & 0 & 0 \\ 0 & 0 & 0 & c & 0 & 0 \\ 0 & 0 & 0 & 0 & c & 0 \\ 0 & 0 & 0 & 0 & 0 & c \end{bmatrix} \quad \begin{aligned} \text{with } a &= \frac{E(1-\nu)}{(1+\nu)(1-2\nu)}, & b &= a \cdot \frac{\nu}{1-\nu} \\ \text{and } c &= a \cdot \frac{1-2\nu}{2(1-\nu)} \end{aligned} \quad (4.21)$$

#### 4.1.4 Strong form

With the equilibrium condition (4.16), the constitutive law (4.20) and the strain definition of small deformations (4.10), the linear elastic problem can be solved for given boundary conditions. On the Dirichlet boundary  $\Gamma_D$ , the displacements are prescribed with  $\bar{\mathbf{u}}$  while on the Neumann boundary  $\Gamma_N$  tractions  $\bar{\mathbf{t}}$  are predefined. Summarizing all ingredients yields the *strong form of linear elasticity*

$$\nabla \cdot \boldsymbol{\sigma} + \mathbf{b} = \mathbf{0} \quad \forall \mathbf{x} \in \Omega \quad (4.22a)$$

$$\boldsymbol{\sigma} = \mathbf{C} : \boldsymbol{\epsilon} \quad \forall \mathbf{x} \in \Omega \quad (4.22b)$$

$$\boldsymbol{\epsilon} = \frac{1}{2} \left[ \nabla \mathbf{u} + [\nabla \mathbf{u}]^T \right] \quad \forall \mathbf{x} \in \Omega \quad (4.22c)$$

$$\mathbf{u} = \bar{\mathbf{u}} \quad \forall \mathbf{x} \in \Gamma_D \quad (4.22d)$$

$$\boldsymbol{\sigma} \cdot \mathbf{n} = \bar{\mathbf{t}} \quad \forall \mathbf{x} \in \Gamma_N. \quad (4.22e)$$

#### 4.1.5 Weak form

Following Galerkin's method of weighted residuals from Section 2.1.2, the integral equation of the weighted residuals reads

$$\int_{\Omega} \mathbf{v} \cdot [\nabla \cdot \boldsymbol{\sigma} + \mathbf{b}] d\Omega + \int_{\Gamma_D} \mathbf{v} \cdot [\mathbf{u} - \bar{\mathbf{u}}] d\Gamma + \int_{\Gamma_N} \mathbf{v} \cdot [\boldsymbol{\sigma} \cdot \mathbf{n} - \bar{\mathbf{t}}] d\Gamma = \mathbf{0}. \quad (4.23)$$

Note that (4.22b) and (4.22c) do not build a residual since they are satisfied a priori. After some rearrangement and integration by parts, the *extended principle of virtual displacements* is

$$\int_{\Omega} \boldsymbol{\epsilon}(\boldsymbol{v}) : \mathbf{C} : \boldsymbol{\epsilon}(\boldsymbol{u}) d\Omega = \int_{\Omega} \boldsymbol{v} \cdot \mathbf{b} d\Omega + \int_{\Gamma_N} \boldsymbol{v} \cdot \bar{\mathbf{t}} d\Gamma + \int_{\Gamma_D} \boldsymbol{v} \cdot \mathbf{t} d\Gamma \\ \wedge \quad \boldsymbol{u} = \bar{\boldsymbol{u}} \quad \forall \mathbf{x} \in \Gamma_D. \quad (4.24)$$

The bilinear functional and linear functional of the linear elastic problem are therefore identified to be

$$\mathcal{B}(\boldsymbol{v}, \boldsymbol{u}) := \int_{\Omega} \boldsymbol{\epsilon}(\boldsymbol{v}) : \mathbf{C} : \boldsymbol{\epsilon}(\boldsymbol{u}) d\Omega, \quad \mathcal{B}(\boldsymbol{v}, \boldsymbol{u}) = \mathcal{B}(\boldsymbol{u}, \boldsymbol{v}) \quad (4.25a)$$

$$\mathcal{F}(\boldsymbol{v}) := \int_{\Omega} \boldsymbol{v} \cdot \mathbf{b} d\Omega + \int_{\Gamma_D} \boldsymbol{v} \cdot \mathbf{t} d\Gamma + \int_{\Gamma_N} \boldsymbol{v} \cdot \bar{\mathbf{t}} d\Gamma. \quad (4.25b)$$

Applying the same variational approach to define the finite-dimensional space of trial functions  $\boldsymbol{u}^h \in \mathcal{T}^h$  and weight functions  $\boldsymbol{v}^h = \delta \boldsymbol{u}_i^h \in \mathcal{V}^h$ , the interpolation approach can be generalized to a vector-valued field. The bilinear functional (4.25a) shall be written in a matrix-vector notation on an element level by using the displacement field approximation

$$\boldsymbol{u}^h = \hat{\boldsymbol{u}}_e^\top \cdot \mathbf{N}_e \quad \forall \mathbf{x} \in \Omega_e \quad (4.26)$$

where  $\hat{\boldsymbol{u}}_e^\top$  contains the discrete displacements column-wise for each node of the element and  $\mathbf{N}_e$  is column vector containing the shape functions. The strains in Voigt notation are interpolated from the nodal displacements by

$$\boldsymbol{\epsilon}^h = \mathbf{B}_e \cdot \hat{\boldsymbol{u}}_e \quad \forall \mathbf{x} \in \Omega_e \quad (4.27)$$

where the strain interpolation matrix  $\mathbf{B}_e$  is constructed to match the strain definition (4.22c) and the Voigt notation

$$\mathbf{B}_e = \begin{bmatrix} \dots & \frac{dN_i}{dx_1} & 0 & 0 & \dots \\ \dots & 0 & \frac{dN_i}{dx_2} & 0 & \dots \\ \dots & 0 & 0 & \frac{dN_i}{dx_3} & \dots \\ \dots & \frac{dN_i}{dx_2} & \frac{dN_i}{dx_1} & 0 & \dots \\ \dots & 0 & \frac{dN_i}{dx_3} & \frac{dN_i}{dx_2} & \dots \\ \dots & \frac{dN_i}{dx_3} & 0 & \frac{dN_i}{dx_1} & \dots \end{bmatrix}, \quad i = 1, \dots, n_e^{\text{no}} \quad (4.28)$$

with  $n_e^{\text{no}}$  being the number of element nodes. At this point, it is important to notice that the multiplication of the displacements with the  $\mathbf{B}_e$  matrix yields the so-called *engineering strains* which can be converted to and from the *physical strains* by

$$\boldsymbol{\varepsilon} = \begin{bmatrix} \varepsilon_{11} & \varepsilon_{12} & \varepsilon_{13} \\ \varepsilon_{21} & \varepsilon_{22} & \varepsilon_{13} \\ \varepsilon_{31} & \varepsilon_{31} & \varepsilon_{33} \end{bmatrix} \quad \longleftrightarrow \quad \boldsymbol{\varepsilon}^\top = [\varepsilon_{11} \ \varepsilon_{22} \ \varepsilon_{33} \ 2 \cdot \varepsilon_{12} \ 2 \cdot \varepsilon_{23} \ 2 \cdot \varepsilon_{13}] \quad (4.29)$$

or short  $[\varepsilon]_{ij} = 2 \cdot [\boldsymbol{\varepsilon}]_{ij}$ ,  $i \neq j$ . The reason for the conversion is, that in this way, the internal product between strain and stress tensors can be computed by vector and matrix-vector multiplications respectively

$$\begin{aligned} \boldsymbol{\varepsilon} : \boldsymbol{\sigma} &= \boldsymbol{\varepsilon}^\top \cdot \boldsymbol{\sigma} \\ \boldsymbol{\varepsilon} : \mathbf{C} : \boldsymbol{\varepsilon} &= \boldsymbol{\varepsilon}^\top \cdot \mathbf{C} \cdot \boldsymbol{\varepsilon}. \end{aligned} \quad (4.30)$$

Substituting the approximation in (4.25a) yields the algebraic system of equations

$$\mathbf{K} \cdot \hat{\mathbf{u}} = \mathbf{f}, \quad \mathbf{K} = \bigwedge_e^{n_e} \mathbf{K}_e, \quad \mathbf{f} = \bigwedge_e^{n_e} \mathbf{f}_e \quad (4.31)$$

and in terms of the element domain gives the element stiffness matrix

$$\mathbf{K}_e = \int_{\Omega_e} \mathbf{B}_e^\top \cdot \mathbf{C} \cdot \mathbf{B}_e d\Omega \quad (4.32)$$

and the element load vector

$$\mathbf{f}_e = \int_{\Omega_e} \tilde{\mathbf{N}}_e \cdot \mathbf{b} d\Omega + \int_{\Gamma_e \cap \Gamma_D} \tilde{\mathbf{N}}_e \cdot \mathbf{t} d\Gamma + \int_{\Gamma_e \cap \Gamma_N} \tilde{\mathbf{N}}_e \cdot \bar{\mathbf{t}} d\Gamma \quad (4.33)$$

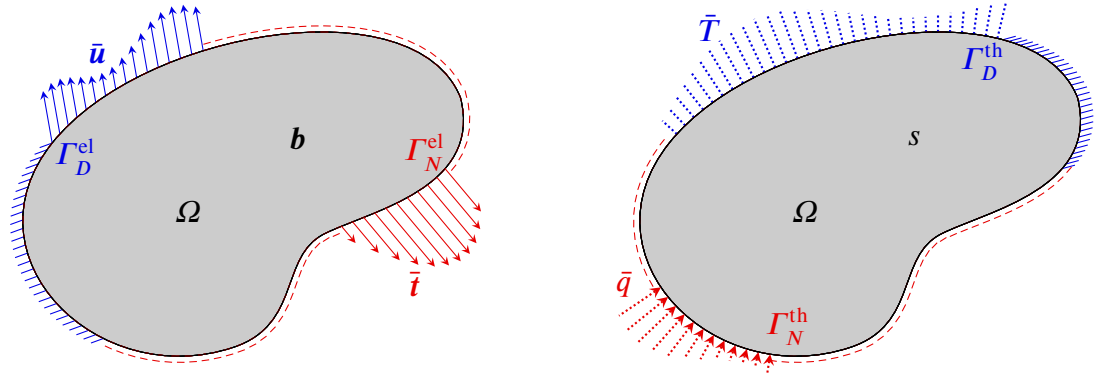
where  $\tilde{\mathbf{N}}_e$  are the element shape functions in a matrix ordering

$$\tilde{\mathbf{N}}_e^\top = \begin{bmatrix} \dots & N_i & 0 & 0 & \dots \\ \dots & 0 & N_i & 0 & \dots \\ \dots & 0 & 0 & N_i & \dots \end{bmatrix}, \quad i = 1, \dots, n_e^{\text{no}}. \quad (4.34)$$

The remaining produce of assembling the system of equations and integrate the element contributions for the system matrix and vector apply analogous to Section 2.1.5.

## 4.2 Formulation of the multi field problem

The multi field problem of thermoelasticity belongs to the class of volume coupled problems where the physical fields of displacements  $\mathbf{u}$  and temperatures  $T$  interact



- (a)** The elastic sub-problem: On the Neu-mann boundary  $\Gamma_N^{\text{el}}$  the tractions  $t = \bar{t}$  are applied and on the Dirichlet boundary  $\Gamma_D^{\text{el}}$  displacements  $u = \bar{u}$  are prescribed. The domain  $\Omega$  is subjected to a body force  $b$ .
- (b)** The thermal sub-problem: On the Neu-mann boundary  $\Gamma_N^{\text{th}}$  the heat flux  $q = \bar{q}$  is applied and on the Dirichlet boundary  $\Gamma_D^{\text{th}}$  temperatures  $T = \bar{T}$  are prescribed. The domain  $\Omega$  is subjected to a heat source  $s$ .

**Figure 4.1** The coupled sub-problems of linear thermoelasticity. Both fields share the same domain  $\Omega$  and corresponding boundary  $\Gamma = \partial\Omega$ .

on a (partially) shared volume. In this work only the case of a fully shared volume is considered, or in other words, the single field domains have no symmetric difference  $\Omega^{\text{el}} \Delta \Omega^{\text{th}} = \emptyset$ . As Figures 4.1a and 4.1b depict, both, the mechanical and thermal field share the same domain  $\Omega$  with naturally the same boundary  $\Gamma = \partial\Omega$ . Topologically, they only differ in the partition of the boundary  $\Gamma$  into the Dirichlet boundaries  $\Gamma_D^{\text{el}}$  and  $\Gamma_D^{\text{th}}$  and the Neumann boundary  $\Gamma_N^{\text{el}}$  and  $\Gamma_N^{\text{th}}$ .

Typically, all fields of a multi field problem interact with each other and no sub problem can be solved independently. Through the first and second law of thermodynamics, a coupling of the elastic and thermal field which influence each other in both directions leads to a nonlinear description of thermoelasticity [Nowacki, 2013, Hetnarski et al., 2009]. However, since a small deformation theory is followed for the linear elastic sub problem, the temperature change due to displacements is neglectable. The interaction between the fields can therefore be decoupled in a pre-step of solving for the temperatures and subsequently solving the linear elastic problem with an additional thermal coupling condition. To account for the deformation of a body due to a change in temperature, an isotropic expansion of the continuum is assumed [Carlson, 1973]. The thermally induced deformation can be accounted as an additional strain, yielding the decomposition of the total strain in

$$\boldsymbol{\epsilon} = \boldsymbol{\epsilon}^{\text{el}} + \boldsymbol{\epsilon}^{\text{th}} \quad (4.35)$$

where the thermal strains are

$$\boldsymbol{\epsilon}^{\text{th}} = \gamma \cdot [T - T_0] \cdot \mathbf{I} \quad (4.36)$$

characterized by the thermal expansion coefficient  $\gamma$  and the temperature difference of the current temperature  $T$  at  $x$  and reference temperature  $T_0$  at the same  $x$  in an initial unstressed state. For the sake of simplicity in the notation, it is assumed that  $T_0$  is zero everywhere, such that the thermal strains can be rewritten by

$$\boldsymbol{\varepsilon}^{\text{th}} = \gamma \cdot T \cdot \mathbf{I}. \quad (4.37)$$

Using the linear measure of strains (4.10), the total strains read

$$\boldsymbol{\varepsilon} = \frac{1}{2} \left[ \nabla \mathbf{u} + [\nabla \mathbf{u}]^\top \right] \quad (4.38)$$

and with (4.35), the elastic strains become

$$\boldsymbol{\varepsilon}^{\text{el}}(\mathbf{u}, T) = \boldsymbol{\varepsilon}(\mathbf{u}) - \boldsymbol{\varepsilon}^{\text{th}}(T). \quad (4.39)$$

Consequently, the strain decomposition entails the stress decomposition

$$\boldsymbol{\sigma}^{\text{tot}} = \boldsymbol{\sigma}^{\text{el}} + \boldsymbol{\sigma}^{\text{th}} \quad \Leftrightarrow \quad \boldsymbol{\sigma}^{\text{el}}(\mathbf{u}, T) = \boldsymbol{\sigma}^{\text{tot}}(\mathbf{u}) - \boldsymbol{\sigma}^{\text{th}}(T) \quad (4.40)$$

and with Hook's generalized law (4.17), the elastic strains are calculated by

$$\boldsymbol{\sigma}^{\text{el}} = \mathbf{C} : \boldsymbol{\varepsilon}^{\text{el}} = \mathbf{C} : [\boldsymbol{\varepsilon} - \boldsymbol{\varepsilon}^{\text{th}}] = \mathbf{C} : \boldsymbol{\varepsilon} - \mathbf{C} : \boldsymbol{\varepsilon}^{\text{th}} = \boldsymbol{\sigma}^{\text{tot}} - \boldsymbol{\sigma}^{\text{th}} \quad (4.41)$$

wherein the thermal stresses are obtained from the linearized *Duhamel-Neumann* constitutive relation simply as

$$\boldsymbol{\sigma}^{\text{th}} = \mathbf{C} : \boldsymbol{\varepsilon}^{\text{th}}. \quad (4.42)$$

Recalling the stationary conservation of momentum (4.16) of the linear elastic problem, the forces caused by the internal stresses are of elastic nature. Hence, it is rewritten in terms of the thermoelastic decomposition

$$\begin{aligned} \nabla \cdot \boldsymbol{\sigma}^{\text{el}} + \mathbf{b} &= \mathbf{0} \\ \nabla \cdot [\boldsymbol{\sigma}^{\text{tot}} - \boldsymbol{\sigma}^{\text{th}}] + \mathbf{b} &= \mathbf{0} \\ \nabla \cdot \boldsymbol{\sigma}^{\text{tot}} - \nabla \cdot \boldsymbol{\sigma}^{\text{th}} + \mathbf{b} &= \mathbf{0} \\ \nabla \cdot \boldsymbol{\sigma}^{\text{tot}}(\mathbf{u}) + \mathbf{b} - \mathbf{b}^{\text{th}}(T) &= \mathbf{0} \end{aligned} \quad (4.43)$$

leading to the thermal body force

$$\mathbf{b}^{\text{th}} = \nabla \cdot \boldsymbol{\sigma}^{\text{th}} \quad (4.44)$$

which is known from the thermal pre-step. Further, recalling the surface tractions on

the Neumann boundary (4.22e) in terms of the thermoelastic decomposition

$$\begin{aligned}\boldsymbol{\sigma}^{\text{el}} \cdot \mathbf{n} &= \bar{t} \\ \boldsymbol{\sigma}^{\text{tot}} \cdot \mathbf{n} - \boldsymbol{\sigma}^{\text{th}} \cdot \mathbf{n} &= \bar{t} \\ \boldsymbol{\sigma}^{\text{tot}} \cdot \mathbf{n} - \mathbf{t}^{\text{th}} &= \bar{t}\end{aligned}\tag{4.45}$$

providing the known thermal surface traction

$$\mathbf{t}^{\text{th}} = \boldsymbol{\sigma}^{\text{th}} \cdot \mathbf{n}\tag{4.46}$$

in a similar sense as the body force. Summarizing the ingredients from the stationary heat conduction (2.2) and linear elasticity (4.22) together with the derived coupling condition yields the *strong form of linear thermoelasticity*

$$\nabla \cdot \mathbf{q} + s = 0 \quad \forall \mathbf{x} \in \Omega\tag{4.47a}$$

$$\mathbf{q} = -\kappa \cdot \nabla T \quad \forall \mathbf{x} \in \Omega\tag{4.47b}$$

$$T = \bar{T} \quad \forall \mathbf{x} \in \Gamma_D^{\text{th}}\tag{4.47c}$$

$$\mathbf{q} \cdot \mathbf{n} = \bar{q} \quad \forall \mathbf{x} \in \Gamma_N^{\text{th}}\tag{4.47d}$$

$$\nabla \cdot \boldsymbol{\sigma}^{\text{tot}} + \mathbf{b} - \mathbf{b}^{\text{th}} = \mathbf{0} \quad \forall \mathbf{x} \in \Omega\tag{4.47e}$$

$$\boldsymbol{\sigma}^{\text{tot}} = \mathbf{C} : \boldsymbol{\epsilon}^{\text{tot}} \quad \forall \mathbf{x} \in \Omega\tag{4.47f}$$

$$\boldsymbol{\epsilon} = \frac{1}{2} \left[ \nabla \mathbf{u} + [\nabla \mathbf{u}]^T \right] \quad \forall \mathbf{x} \in \Omega\tag{4.47g}$$

$$\mathbf{b}^{\text{th}} = \nabla \cdot \boldsymbol{\sigma}^{\text{th}} \quad \forall \mathbf{x} \in \Omega\tag{4.47h}$$

$$\boldsymbol{\sigma}^{\text{th}} = \mathbf{C} : \boldsymbol{\epsilon}^{\text{th}} \quad \forall \mathbf{x} \in \Omega\tag{4.47i}$$

$$\boldsymbol{\epsilon}^{\text{th}} = \gamma \cdot T \cdot \mathbf{I} \quad \forall \mathbf{x} \in \Omega\tag{4.47j}$$

$$\mathbf{u} = \bar{\mathbf{u}} \quad \forall \mathbf{x} \in \Gamma_D^{\text{el}}\tag{4.47k}$$

$$\boldsymbol{\sigma} \cdot \mathbf{n} = \bar{t} + \mathbf{t}^{\text{th}} \quad \forall \mathbf{x} \in \Gamma_D^{\text{el}}\tag{4.47l}$$

$$\mathbf{t}^{\text{th}} = \boldsymbol{\sigma}^{\text{th}} \cdot \mathbf{n} \quad \forall \mathbf{x} \in \Gamma_N^{\text{el}}.\tag{4.47m}$$

## 4.3 Weak form of linear thermoelasticity

Still, for the thermoelastic problem, the temperature is assumed to be known from a thermal pre-step (4.47a) to (4.47d) through the weak form (2.10). Therefore, the weak form of linear thermoelasticity can be derived in the same manner as shown for linear elastic problem (4.23). Galerkin's method of weighted residuals (Section 2.1.2) leads to the integral equation

$$\int_{\Omega} \boldsymbol{\nu} \cdot [\nabla \cdot \boldsymbol{\sigma}^{\text{tot}} + \mathbf{b} - \mathbf{b}^{\text{th}}] d\Omega + \int_{\Gamma_D^{\text{el}}} \boldsymbol{\nu} \cdot [\mathbf{u} - \bar{\mathbf{u}}] d\Gamma + \int_{\Gamma_N^{\text{el}}} \boldsymbol{\nu} \cdot [\boldsymbol{\sigma} \cdot \mathbf{n} - \bar{t} - \mathbf{t}^{\text{th}}] d\Gamma = \mathbf{0}\tag{4.48}$$

where some rearrangement gives

$$\begin{aligned} \int_{\Omega} \boldsymbol{\nu} \cdot [\nabla \cdot \boldsymbol{\sigma}^{\text{tot}} + \boldsymbol{b}] d\Omega + \int_{\Gamma_D^{\text{el}}} \boldsymbol{\nu} \cdot [\boldsymbol{u} - \bar{\boldsymbol{u}}] d\Gamma + \int_{\Gamma_N^{\text{el}}} \boldsymbol{\nu} \cdot [\boldsymbol{\sigma} \cdot \boldsymbol{n} - \bar{\boldsymbol{t}}] d\Gamma \\ = \int_{\Omega} \boldsymbol{\nu} \cdot \boldsymbol{b}^{\text{th}} d\Omega + \int_{\Gamma_N^{\text{el}}} \boldsymbol{\nu} \cdot \boldsymbol{t}^{\text{th}} d\Gamma. \end{aligned} \quad (4.49)$$

The integral terms on the left-hand side of the equation are identical to the ones of the linear elastic problem (4.23) such that the transformation of these terms into the functionals (4.25) is already known to be

$$\mathcal{B}^{\text{el}}(\boldsymbol{\nu}, \boldsymbol{u}) := \int_{\Omega} \boldsymbol{\epsilon}(\boldsymbol{\nu}) : \mathbf{C} : \boldsymbol{\epsilon}(\boldsymbol{u}) d\Omega \quad (4.50a)$$

$$\mathcal{F}^{\text{el}}(\boldsymbol{\nu}) := \int_{\Omega} \boldsymbol{\nu} \cdot \boldsymbol{b} d\Omega + \int_{\Gamma_D^{\text{el}}} \boldsymbol{\nu} \cdot \boldsymbol{t} d\Gamma + \int_{\Gamma_N^{\text{el}}} \boldsymbol{\nu} \cdot \bar{\boldsymbol{t}} d\Gamma. \quad (4.50b)$$

Additionally, the *bilinear functional of linear thermoelastic coupling* can be identified by applying integration by parts on the right-hand side of the integral equation and considering the relations (4.47h) to (4.47j) and (4.47m)

$$\begin{aligned} \mathcal{B}_{\text{th}}^{\text{el}}(\boldsymbol{\nu}, T) &:= \int_{\Omega} \boldsymbol{\nu} \cdot \boldsymbol{b}^{\text{th}} d\Omega - \int_{\Gamma_N^{\text{el}}} \boldsymbol{\nu} \cdot \boldsymbol{t}^{\text{th}} d\Gamma \\ &= - \int_{\Omega} \boldsymbol{\epsilon}(\boldsymbol{\nu}) : \boldsymbol{\sigma}^{\text{th}} d\Omega + \int_{\Gamma_D^{\text{el}}} \boldsymbol{\nu} \cdot [\boldsymbol{\sigma}^{\text{th}} \cdot \boldsymbol{n}] d\Gamma \\ &= - \int_{\Omega} \boldsymbol{\epsilon}(\boldsymbol{\nu}) : \mathbf{C} : \boldsymbol{\epsilon}^{\text{th}}(T) d\Omega + \int_{\Gamma_D^{\text{el}}} \boldsymbol{\nu} \cdot [\boldsymbol{\sigma}^{\text{th}} \cdot \boldsymbol{n}] d\Gamma \\ &= - \int_{\Omega} \boldsymbol{\epsilon}(\boldsymbol{\nu}) : \mathbf{C} : [\gamma \cdot T \cdot \mathbf{I}] d\Omega + \int_{\Gamma_D^{\text{el}}} \boldsymbol{\nu} \cdot \boldsymbol{t}^{\text{th}} d\Gamma \end{aligned} \quad (4.51)$$

where the last integral term over  $\Gamma_D^{\text{el}}$  represents the surface reaction due to thermal deformation and can be ignored in the step of solving for the displacements. The weak

form can now be summarized to

$$\begin{aligned} \mathcal{B}^{\text{el}}(\boldsymbol{v}, \boldsymbol{u}) &= \mathcal{F}^{\text{el}}(\boldsymbol{v}) - \mathcal{B}_{\text{th}}^{\text{el}}(\boldsymbol{v}, T) \\ \int_{\Omega} \boldsymbol{\epsilon}(\boldsymbol{v}) : \mathbf{C} : \boldsymbol{\epsilon}(\boldsymbol{u}) d\Omega &= \int_{\Omega} \boldsymbol{v} \cdot \mathbf{b} d\Omega + \int_{\Gamma_D^{\text{el}}} \boldsymbol{v} \cdot [\mathbf{t} + \mathbf{t}^{\text{th}}] d\Gamma + \int_{\Gamma_N^{\text{el}}} \boldsymbol{v} \cdot \bar{\mathbf{t}} d\Gamma \\ &\quad + \int_{\Omega} \boldsymbol{\epsilon}(\boldsymbol{v}) : \mathbf{C} : [\boldsymbol{\gamma} \cdot \mathbf{T} \cdot \mathbf{I}] d\Omega. \end{aligned} \quad (4.52)$$

In terms of the algebraic system of equations, the subsequent solving procedure of the multi field problem can be written in matrix-vector notation as

$$\begin{aligned} \begin{bmatrix} \mathbf{K}^{\text{el}} & \mathbf{K}_{\text{th}}^{\text{el}} \\ \mathbf{0} & \mathbf{K}^{\text{th}} \end{bmatrix} \cdot \begin{bmatrix} \hat{\boldsymbol{u}} \\ \hat{\mathbf{T}} \end{bmatrix} &= \begin{bmatrix} \mathbf{f}^{\text{el}} \\ \mathbf{f}^{\text{th}} \end{bmatrix} \\ \mathbf{K}^{\text{el}} \cdot \hat{\boldsymbol{u}} &= \mathbf{f}^{\text{el}} - \mathbf{K}_{\text{th}}^{\text{el}} \cdot \hat{\mathbf{T}} \\ \mathbf{K}^{\text{el}} \cdot \hat{\boldsymbol{u}} &= \mathbf{f}^{\text{el}} - \mathbf{K}_{\text{th}}^{\text{el}} \cdot \underbrace{\left[ [\mathbf{K}^{\text{th}}]^{-1} \cdot \mathbf{f}^{\text{th}} \right]}_{\text{thermal pre-step}} \end{aligned} \quad (4.53)$$

where the linear elastic and stationary heat conduction stiffness matrix  $\mathbf{K}^{\text{el}}$  (4.32) and  $\mathbf{K}^{\text{th}}$ , assembled from (4.32) and (2.32a) respectively, are on the main diagonal and the coupling matrix is the top right connection. Since the interaction is one-way-directed and the displacements  $\boldsymbol{u}$  have no influence on the temperatures  $T$ , the lower left connection is filled with zeros. From the weak form of thermoelasticity (4.52) in discretized form

$$\begin{aligned} \int_{\Omega_e} \mathbf{B}_e^T \cdot \mathbf{C} \cdot \mathbf{B}_e d\Omega \cdot \hat{\boldsymbol{u}} &= \int_{\Omega_e} \tilde{\mathbf{N}}_e \cdot \mathbf{b} d\Omega + \int_{\Gamma_e \cap \Gamma_D^{\text{el}}} \tilde{\mathbf{N}}_e \cdot \mathbf{t} d\Gamma + \int_{\Gamma_e \cap \Gamma_N^{\text{el}}} \tilde{\mathbf{N}}_e \cdot \bar{\mathbf{t}} d\Gamma \\ &\quad + \int_{\Omega_e} \mathbf{B}_e^T \cdot \mathbf{C} \cdot \boldsymbol{\gamma} \cdot \tilde{\mathbf{N}}_e d\Omega \cdot \hat{\mathbf{T}} \end{aligned} \quad (4.54)$$

the *thermoelastic coupling matrix* is identified to be

$$\mathbf{K}_{\text{th}}^{\text{el}} = \mathbf{A} - \int_{\Omega_e} \mathbf{B}_e^T \cdot \mathbf{C} \cdot \boldsymbol{\gamma} \cdot \tilde{\mathbf{N}}_e d\Omega \quad (4.55)$$

where the matrix  $\tilde{\mathbf{N}}_e$  contains the shape functions of the element specifically ordered to match the assumption of isotropic expansion and translates the field variance from

the scalar field  $T(\mathbf{x})$  to the vector field  $\mathbf{u}(\mathbf{x})$

$$\tilde{\mathbf{N}}_e = \begin{bmatrix} \dots & N_i & \dots \\ \dots & N_i & \dots \\ \dots & N_i & \dots \\ \dots & 0 & \dots \\ \dots & 0 & \dots \\ \dots & 0 & \dots \end{bmatrix}, \quad i = 1, \dots, n_e^{\text{no}} \quad (4.56)$$

where  $n_e^{\text{no}}$  is the number of nodes per element. The polynomial degree of the fields can be chosen independently, which can be reasonable when for example solving a rather unspectacular problem of heat conduction, but expecting a more complex elastic reaction. In that case, the strain interpolation matrix  $\mathbf{B}_e$  is based on the elastic shape functions and the matrix  $\tilde{\mathbf{N}}_e$  is based on the thermal shape functions. In order to have completely different approximation spaces, that is not only the polynomial degree, but the mesh too, further field coupling techniques are required which are not used in this work.

## 4.4 Ring plate benchmark

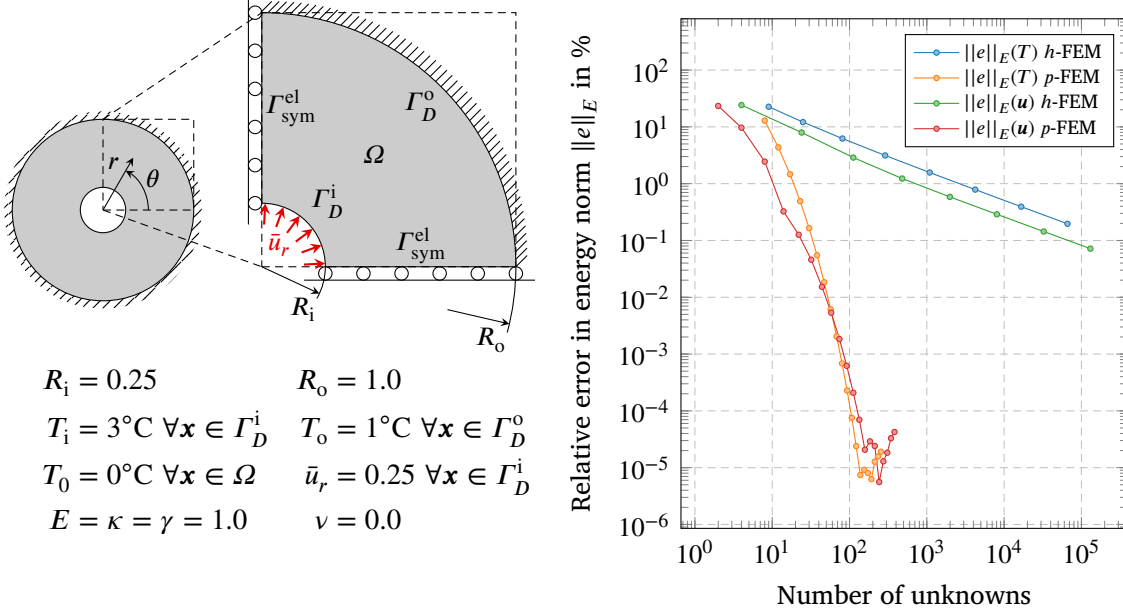
The presented thermoelastic finite element shall be validated with the ring plate benchmark described on the left-hand side of Figure 4.2. Due to its symmetry, only a quarter of the ring is analysed which is achieved by applying symmetry boundary conditions in the elastic sub-problem at  $\Gamma_{\text{sym}}^{\text{el}}$ . The elastic material is lumped to two dimensions assuming a plane stress state. Both fields have prescribed values at the inner and outer Dirichlet boundaries  $\Gamma_D^i$  and  $\Gamma_D^o$ . The elastic sub-problem is pressured from within the ring and constrained at the outer radius. The thermal sub-problem has a higher prescribed temperature on the inner radius than at the outer radius, such that the heat flows outwards. The analytic solution of the displacement components  $u_r(r)$  and  $u_\theta(r)$  as well as the temperature  $T(r)$  along the radius are taken as the exact reference solution with

$$u_r(r) = -\frac{r}{2} \cdot \frac{\ln(r)}{\ln(2)}, \quad u_\theta(r) = 0, \quad T(r) = 1 - \frac{\ln(r)}{\ln(2)}. \quad (4.57)$$

With the exact solutions, the relative errors in energy norm  $\|e\|_E(\bullet)$ , see (2.37), can be calculated for both fields with respect to the exact bilinear functionals

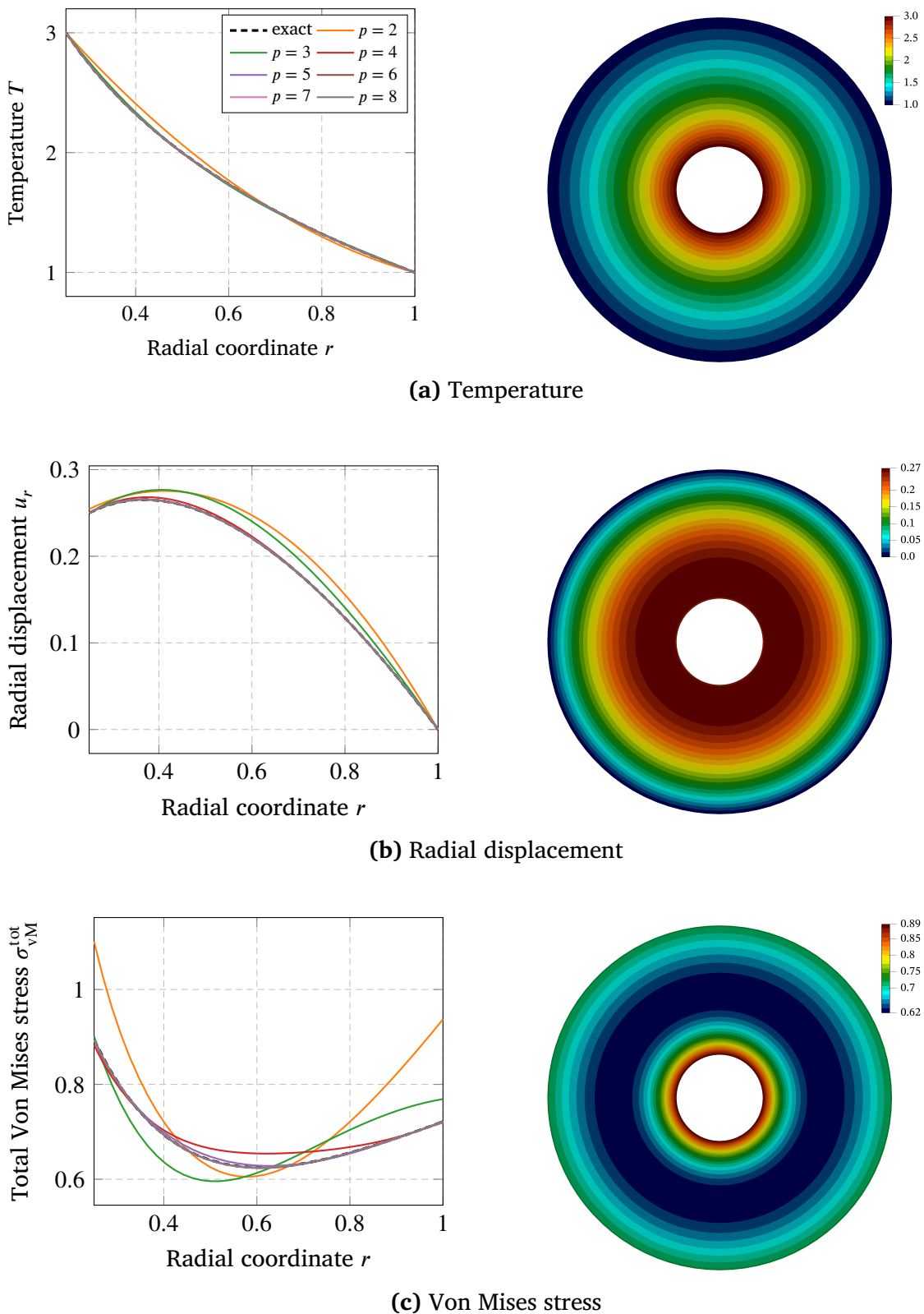
$$\mathcal{B}(\mathbf{u}, \mathbf{u}) = \frac{\pi}{8 \cdot \ln^2(2)} \left[ 1 - \frac{2 \cdot \ln^2(4) + 1}{16} \right] \approx 0.5699176661979298 \quad (4.58a)$$

$$\mathcal{B}(T, T) = \frac{\pi \cdot \kappa}{\ln^2(2)} \cdot [\ln(1.0) - \ln(0.25)] \approx 9.064720283654388 \quad (4.58b)$$



**Figure 4.2** Thermoelastic ring plate benchmark problem: The heat flow problem has prescribed temperatures  $T_i$  on the inner radius  $R_i$  and  $T_o$  on the outer radius  $R_o$ . The elasticity problem has a prescribed radial displacement  $\bar{u}_r$  at  $R_i$  and is constrained in radial direction at  $R_o$ . The plane stress constitutive is used for the material tensor.

using the parameters listed in Figure 4.2. Performing an  $h$ - and  $p$ -FEM convergence study reveals the curves on the right-hand side of Figure 4.2. The  $p$ -refinement provides an accuracy around machine precision for  $p \geq 14$  after an exponential rate of convergence while the  $h$ -refinements converge linearly for both solution fields. The  $p$ -FEM reaches its minimum error of circa  $10^{-5}\%$  at around 200 degrees of freedom where the  $h$ -FEM produces an error of roughly 3% for both fields. In Figure 4.3 the temperature, displacement and von Mises equivalent stress is plotted over the radial coordinate for shape function orders  $p = 2, \dots, 8$  together with the distribution over the domain. While the temperature is approximated visually exactly for  $p \geq 3$ , the displacement requires a polynomial degree of  $p \geq 5$  to be visually not distinguishable from the exact solution. The von Mises stress, which involves the shape function derivatives, is pretty exact for  $p \geq 6$ . Here, it is clearly visible that a satisfying approximation of the primal unknowns  $T$  and  $u$  is achieved with less enrichment of the approximation space than state quantities which may involve derivatives.

**Figure 4.3** Results of ring plate benchmark.



# Chapter 5

## Small strain elastoplasticity

In this chapter, the linear elastic material from Section 4.1 is extended by the theory of small strain plasticity. The presented material model captures both, linear elastic and the nonlinear plastic material behavior from which the term *elastoplasticity* originates. The following mathematical derivation and its numerical application by means of the finite element method follows the mathematical model and its implementation of [de Souza Neto et al., 2011].

### 5.1 Mathematical theory

To introduce the essential phenomena of elastoplasticity, a specimen under uniaxial tension is considered. As shown in Figure 5.1, in response to the tensile straining, the metal rod follows a so-called *stress-strain curve*  $O_0Y_0Z_0O_1Y_1Z_1$  which, in this case, describes a sequence of two loadings. The first segment  $O_0Y_0$  is the linear elastic domain with the Young's modulus  $E$  being the slope. The deformation is fully reversible until it reaches the *initial yield stress*  $\sigma_{y_0}$ . Beyond  $Y_0$  the curve changes its behavior significantly in a nonlinear fashion. From here on, the deformation is irreversible and the material undergoes *plastic yielding* or *plastic flow*, that is, the evolution of plastic strain  $\varepsilon^p$  occurs. Besides the evolution of the plastic strain, an evolution of the yield stress  $\sigma_y$  takes place as well. This phenomenon is called *hardening*, in the sense that the material is strengthened through plastic deformation, also known as *cold-work hardening*. At  $Z_0$  the loading is taken back such that the elastic strains are fully reversed in a new unstressed state  $O_1$ . If the rod is loaded again from this state, linear elastic deformation takes place along  $O_1Y_1$  until, again, a yield stress  $\sigma_{y_1}$  is reached which has increased compared to the initial  $\sigma_{y_0}$  due to hardening. Beyond  $Y_1$  the material continues to accumulate plastic strain up to the end state  $Z_1$ . While the states  $Y_1$  and  $Z_1$  as well as the paths  $Z_0O_1$  and  $O_1Y_1$  do not exactly coincide in realistic materials, their difference is very small and will be neglected in the mathematical model such that  $Y_1 = Z_0$  and  $Z_0O_1 = O_1Y_1$ . To the left of the stress-strain diagram, the hardening process is shown in the space

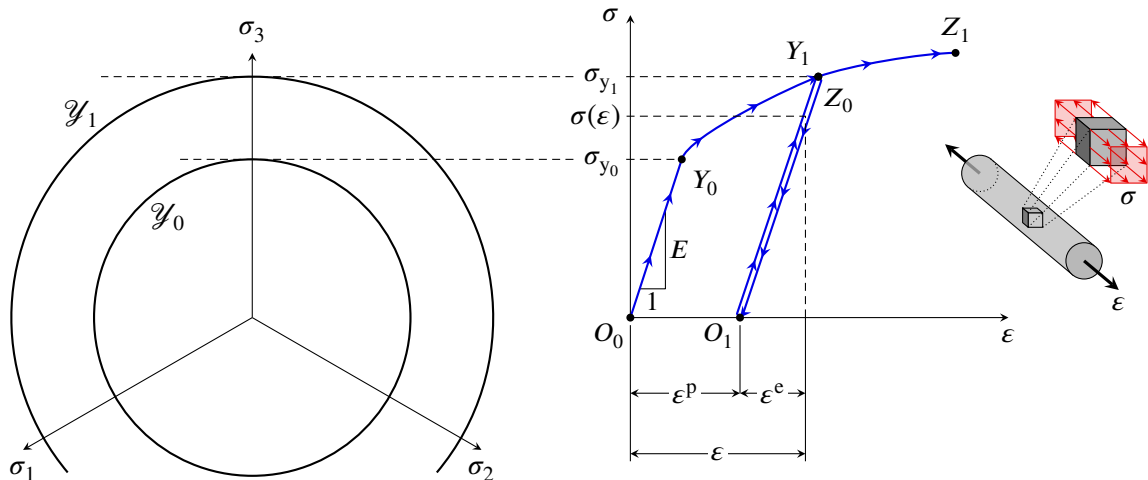


**Figure 5.1** Mathematical model of a uniaxial tensile specimen under elastoplastic deformation.

The *stress-strain diagram* on the right shows two subsequent loadings with the paths  $O_0Y_0Y_1O_1$  and  $O_1Z_0Z_1$ . The hardening of the material can be seen by the increased yield stress  $\sigma_{y_1}$  from an initial yield stress  $\sigma_{y_0}$ . This particular hardening process isotropically scales the radius of the von Mises *yield surface* in the principal stress space  $(\sigma_1, \sigma_2, \sigma_3)$  as shown on the left side.

of principal stresses. All stress states during the first load application that are lying within the cylinder bounded by the von Mises *yield surface*  $\mathcal{Y}_0$  are in the *elastic domain*. Stress states which are located on the yield surface undergo plastic deformation. During plastic deformation, the hardening process leads to an increase of the yield surface in its radius corresponding to the yield stress  $\sigma_y$ . It shall be noted that other definitions of the yield surface exist than the von Mises yield theory also named *J<sub>2</sub> flow theory*. However, for ductile metals, the *J<sub>2</sub>* flow theory has been proven to accurately capture realistic material behavior and other theories are better suited for materials like soil, concrete or rock. Therefore, this work will focus on the *J<sub>2</sub>* flow theory to derive a plasticity model.

A short overview of the mathematical model shall be given, followed by the derivation section by section. A multidimensional elastoplastic model can be summarized by the basic ingredients of

1. the decomposition of the strains in elastic and plastic,

$$\boldsymbol{\epsilon} = \boldsymbol{\epsilon}^e + \boldsymbol{\epsilon}^p$$

2. a free energy potential,

$$\psi(\boldsymbol{\epsilon}^e, \boldsymbol{\alpha})$$

3. constitutive laws covering the elastic and hardening process,

$$\boldsymbol{\sigma} = \rho \cdot \frac{\partial \psi}{\partial \boldsymbol{\epsilon}^e}, \quad \mathbf{A} = \rho \cdot \frac{\partial \psi}{\partial \boldsymbol{\alpha}}$$

4. a yield criterion in form of a yield function,

$$\Phi(\sigma, A)$$

5. a plastic flow rule describing the evolution of the plastic strains

$$\dot{\epsilon}^p = \dot{\gamma} \cdot N(\sigma, A)$$

6. and a hardening law describing the evolution of the yield stress

$$\dot{\alpha} = \dot{\gamma} \cdot H(\sigma, A).$$

### 5.1.1 Strain decomposition

Similar to the thermoelastic strain decomposition (4.35), the strains are decomposed into two differently behaving parts. Here, a reversible (elastic) part  $\epsilon^e$  and an irreversible (plastic) part  $\epsilon^p$  add up to the elastoplastic strain tensor

$$\epsilon = \epsilon^e + \epsilon^p. \quad (5.1)$$

The decomposition further holds for the strain rates

$$\dot{\epsilon} = \dot{\epsilon}^e + \dot{\epsilon}^p \quad (5.2)$$

to describe their evolution over time  $t$ . In this section, rate-independent plasticity is considered, hence  $t$  is rather a pseudo-time and remains during the formulation to indicate a temporal evolution.

### 5.1.2 Free energy potential

The material model will be formulated using the approach of *thermodynamics with internal variables* which hypothesizes that a thermodynamic process can be completely determined by several *state variables*. The current thermodynamic state will only depend on the internal variables at the current time instant and not on their evolution history. For this work, those internal variables will be

$$\{\mathbf{F}, T, \nabla T, \alpha\} \quad (5.3)$$

where  $\mathbf{F}$  is the previously introduced deformation gradient and  $T$  is the temperature. The set  $\alpha$  contains the *internal variables* which generally describe the dissipative phenomena of the process. The first principle of thermodynamics postulates the *conservation of energy*

$$\rho \cdot \dot{e} = \sigma : \mathbf{D} + \rho \cdot r - \nabla \cdot q \quad (5.4)$$

which means that the rate of *internal energy per unit deformed volume*  $\rho \cdot \dot{e}$  must equal the sum of the *stress power*  $\boldsymbol{\sigma} : \mathbf{D}$  and *heat production per unit deformed volume*  $\rho \cdot r$  minus the divergence of the heat flux. The *stretching tensor*  $\mathbf{D}$  is defined by the symmetric part  $\text{sym}(\dot{\mathbf{F}}\mathbf{F}^{-1})$  and describes the rate of deformation. The second principle states the *irreversibility of entropy production*

$$\rho \cdot \dot{s} + \nabla \cdot \frac{\mathbf{q}}{T} - \frac{\rho \cdot r}{T} \geq 0 \quad (5.5)$$

where  $\rho \cdot \dot{s}$  is the rate of *entropy per unit deformed volume*. The combination of the first and second principle yields

$$\rho \cdot \dot{s} + \nabla \cdot \frac{\mathbf{q}}{T} - \frac{1}{T} \cdot [\rho \cdot \dot{e} - \boldsymbol{\sigma} : \mathbf{D} + \nabla \cdot \mathbf{q}] \geq 0. \quad (5.6)$$

Given the identity

$$\nabla \cdot \frac{\mathbf{q}}{T} = \frac{1}{T} \cdot \nabla \cdot \mathbf{q} - \frac{\mathbf{q}}{T^2} \cdot \nabla T \quad (5.7)$$

equation (5.6) can be reformatted to the *Clausius–Duhem inequality*

$$\begin{aligned} \boldsymbol{\sigma} : \mathbf{D} - \rho \cdot \dot{e} + \rho \cdot T \cdot \dot{s} - \frac{1}{T} \cdot \mathbf{q} \cdot \nabla T &\geq 0 \\ \boldsymbol{\sigma} : \mathbf{D} - \rho \cdot [\psi + s \cdot \dot{T}] - \frac{1}{T} \cdot \mathbf{q} \cdot \nabla T &\geq 0 \end{aligned} \quad (5.8)$$

where the (*Helmholtz*) *specific free energy* is introduced with

$$\psi = e - T \cdot s. \quad (5.9)$$

At this point, recalling the introduced internal variables (5.3) yields a specific free energy of the form

$$\psi = \psi(\mathbf{F}, T, \boldsymbol{\alpha}) \quad (5.10)$$

where the dependence on the temperature gradient is not assumed to prevent contradicting the second principle of thermodynamics. The rate of this specific energy is then

$$\dot{\psi}(\mathbf{F}, T, \boldsymbol{\alpha}) = \frac{\partial \psi}{\partial \mathbf{F}} : \dot{\mathbf{F}} + \frac{\partial \psi}{\partial T} \cdot \dot{T} + \frac{\partial \psi}{\partial \boldsymbol{\alpha}} \cdot \dot{\boldsymbol{\alpha}} \quad (5.11)$$

where the multiplication symbol  $\bullet$  indicates an appropriate multiplication depending on the type of internal variable, e.g. scalar, vector or tensor. Substituting this form into the Clausius-Duhem inequality (5.8) and considering the relation  $\boldsymbol{\sigma} : \mathbf{D} = \boldsymbol{\sigma} : \text{sym}(\dot{\mathbf{F}}\mathbf{F}^{-1}) = \boldsymbol{\sigma} \cdot \mathbf{F}^{-\top} : \dot{\mathbf{F}}$  gives

$$\left[ \boldsymbol{\sigma} \cdot \mathbf{F}^{-\top} - \rho \cdot \frac{\partial \psi}{\partial \mathbf{F}} \right] : \dot{\mathbf{F}} - \rho \cdot \left[ s + \frac{\partial \psi}{\partial T} \right] \cdot \dot{T} - \rho \cdot \frac{\partial \psi}{\partial \boldsymbol{\alpha}} \cdot \dot{\boldsymbol{\alpha}} - \frac{1}{T} \cdot \mathbf{q} \cdot \nabla T \geq 0. \quad (5.12)$$

The *thermodynamic determinism* dictates the constitutive relations such that the inequality holds for every thermokinetic process, namely for the pair  $\{\dot{\mathbf{F}}(t), \dot{T}(t)\}$ , which implies that the bracket terms have to be zero. Therefore, the constitutive relations for the stress tensor and the entropy are implied to be

$$\boldsymbol{\sigma} = \rho \cdot \frac{\partial \psi}{\partial \mathbf{F}} \cdot \mathbf{F}^\top \quad \text{and} \quad s = -\frac{\partial \psi}{\partial T} \quad (5.13)$$

Beyond this introduction of thermodynamic basics and notation, only its explicit application to the theory of plasticity models is discussed in this work. The reader is referred to [de Souza Neto et al., 2011] and [Bataille and Kestin, 1977] for deeper insights.

For now, it is assumed that temperature is constant all over the body such that each and every material point behaves identically given its material parameters at the reference temperature. Following the hypothesis of internal variables and considering the strain decomposition, the specific free energy is assumed to be a function of the form

$$\psi = \psi(\boldsymbol{\varepsilon}; \boldsymbol{\varepsilon}^p, \boldsymbol{\alpha}), \quad \boldsymbol{\varepsilon} = \boldsymbol{\varepsilon}^e + \boldsymbol{\varepsilon}^p, \quad \boldsymbol{\varepsilon}^e = \frac{1}{2} [\mathbf{H}(\mathbf{F}) + \mathbf{H}(\mathbf{F})^\top] \quad (5.14)$$

where the plastic strains  $\boldsymbol{\varepsilon}^p$  are considered as an internal variable along with additional internal variables  $\boldsymbol{\alpha}$  which capture the hardening process. Just like the strains, the free energy can be assumed to be decomposable into

$$\begin{aligned} \psi(\boldsymbol{\varepsilon}; \boldsymbol{\varepsilon}^p, \boldsymbol{\alpha}) &= \psi^e(\boldsymbol{\varepsilon} - \boldsymbol{\varepsilon}^p) + \psi^p(\boldsymbol{\alpha}) \\ &= \psi^e(\boldsymbol{\varepsilon}^e) + \psi^p(\boldsymbol{\alpha}) \end{aligned} \quad (5.15)$$

namely an elastic part where the internal variables are the plastic strains through  $\boldsymbol{\varepsilon}^e$  and a plastic part as a function of the internal hardening variables. Considering the decomposed rate of the free energy in the Clausius-Duhem inequality yields

$$\left[ \boldsymbol{\sigma} - \rho \cdot \frac{\partial \psi^e}{\partial \boldsymbol{\varepsilon}^e} \right] : \boldsymbol{\varepsilon}^e + \boldsymbol{\sigma} : \dot{\boldsymbol{\varepsilon}}^p - \rho \cdot \frac{\partial \psi^p}{\partial \boldsymbol{\alpha}} \cdot \boldsymbol{\alpha} \geq 0 \quad (5.16)$$

and thereby implies an elastic constitutive law of the form

$$\boldsymbol{\sigma} = \rho \cdot \frac{\partial \psi^e}{\partial \boldsymbol{\varepsilon}^e} \quad (5.17)$$

denoting the *thermodynamic force* associated with the plastic strains by  $-\boldsymbol{\sigma}$  and the *hardening thermodynamic force* is defined by

$$\mathbf{A} := \rho \cdot \frac{\partial \psi^p}{\partial \boldsymbol{\alpha}}. \quad (5.18)$$

Substituting (5.17) into (5.16) reduces the inequality to the so-called *plastic dissipation*

function

$$Y^p(\boldsymbol{\sigma}, \mathbf{A}; \dot{\boldsymbol{\epsilon}}^p, \dot{\boldsymbol{\alpha}}) := \boldsymbol{\sigma} : \dot{\boldsymbol{\epsilon}}^p - \mathbf{A} \bullet \dot{\boldsymbol{\alpha}} \geq 0. \quad (5.19)$$

### 5.1.3 Elastic material law

The elastic part is considered to be linear and isotropic such that the previously introduced theory of linear elasticity holds. Thus, the elastic contribution to the free energy is covered by the elastic strain energy

$$\begin{aligned} \rho \cdot \psi^e(\boldsymbol{\epsilon}^e) &= \frac{1}{2} \cdot \boldsymbol{\epsilon}^e : \mathbf{C}^e : \boldsymbol{\epsilon}^e \\ &= G \cdot \boldsymbol{\epsilon}_d^e : \boldsymbol{\epsilon}_d^e + \frac{1}{2} \cdot K \cdot [\boldsymbol{\epsilon}_v^e]^2 \end{aligned} \quad (5.20)$$

with  $\mathbf{C}^e$  being the isotropic linear elasticity tensor,  $K$  is the bulk modulus and  $G$  is the shear modulus which are related to the Young's modulus  $E$  and Poisson ratio  $\nu$  by

$$K = \frac{E}{3 \cdot (1 - 2 \cdot \nu)} \quad \text{and} \quad G = \frac{E}{2 \cdot (1 + \nu)}. \quad (5.21)$$

The elastic strains of the second version are split into a purely volumetric contribution  $\boldsymbol{\epsilon}_v^e$  and a volume-preserving contribution  $\boldsymbol{\epsilon}_d^e$

$$\boldsymbol{\epsilon}^e = \boldsymbol{\epsilon}_d^e + \boldsymbol{\epsilon}_v^e \quad (5.22)$$

where the *volumetric strain tensor* is

$$\boldsymbol{\epsilon}_v^e = \frac{1}{3} \cdot \boldsymbol{\epsilon}_v^e \cdot \mathbf{I} = \frac{1}{3} \cdot \text{tr}(\boldsymbol{\epsilon}^e) \cdot \mathbf{I}, \quad \epsilon_v^e = \text{tr}(\boldsymbol{\epsilon}^e) \quad (5.23)$$

where  $\text{tr}(\bullet) = \sum_i (\bullet)_{ii}$  is the trace of  $(\bullet)$ . and the so-called *deviatoric strain tensor* causing pure distortion is naturally given by

$$\boldsymbol{\epsilon}_d^e = \boldsymbol{\epsilon}^e - \boldsymbol{\epsilon}_v^e. \quad (5.24)$$

In addition, the elastic constitutive law in the split format reads

$$\begin{aligned} \boldsymbol{\sigma} &= \rho \cdot \frac{\partial \psi^e(\boldsymbol{\epsilon}^e)}{\partial \boldsymbol{\epsilon}^e} = \mathbf{C}^e : \boldsymbol{\epsilon}^e \\ &= 2 \cdot G \cdot \boldsymbol{\epsilon}_d^e + K \cdot \boldsymbol{\epsilon}_v^e \cdot \mathbf{I} \\ &= \mathbf{s} + p \cdot \mathbf{I} \end{aligned} \quad (5.25)$$

where  $\mathbf{s}$  is called the *deviatoric stress tensor* and  $p$  the *hydrostatic pressure*.

### 5.1.4 Yield criterion

A yield criterion establishes the limit where the material leaves the domain of linear elastic behavior and undergoes so-called *plastic flow* or *plastic yielding* which leads to irreversible deformations of the body. It is convenient to formulate a *yield function*  $\Phi$  which is negative for purely elastic occurrences and zero if plastic flow is obtained. It is further assumed that  $\Phi$  is a scalar function of the stresses and hardening thermodynamic forces. Thus, plastic flow occurs only when

$$\Phi(\boldsymbol{\sigma}, \mathbf{A}) = 0 \quad (5.26)$$

and no positive values are allowed for the yield function. More specifically, an *elastic domain* is defined by

$$\mathcal{E} = \{\boldsymbol{\sigma} \mid \Phi(\boldsymbol{\sigma}, \mathbf{A}) < 0\} \quad (5.27)$$

with a boundary called *yield locus* where plastic yielding occurs. The yield locus is a hypersurface in the stress space and therefore also called *yield surface*, defined by

$$\mathcal{Y} = \{\boldsymbol{\sigma} \mid \Phi(\boldsymbol{\sigma}, \mathbf{A}) = 0\}. \quad (5.28)$$

Any stress state lying within the elastic domain  $\mathcal{E}$  or on its boundary  $\mathcal{Y}$  shall be called *plastically admissible* denoted by

$$\bar{\mathcal{E}} = \mathcal{E} \cup \mathcal{Y} = \{\boldsymbol{\sigma} \mid \Phi(\boldsymbol{\sigma}, \mathbf{A}) \leq 0\}. \quad (5.29)$$

Following the  $J_2$  flow theory, the *von Mises yield criterion* is employed to describe plastic yielding. A note on tensor invariants shall be given first to introduce the yield function. The *Cayley-Hamilton theorem* states that a tensor, here the stress tensor  $\boldsymbol{\sigma}$ , satisfies its characteristic equation

$$\boldsymbol{\sigma}^3 - I_1(\boldsymbol{\sigma}) \cdot \boldsymbol{\sigma}^2 + I_2(\boldsymbol{\sigma}) \cdot \boldsymbol{\sigma} - I_3(\boldsymbol{\sigma}) \cdot \mathbf{I} = \mathbf{0} \quad (5.30)$$

where the characteristic polynomial on the left-hand side has the principal stresses  $\sigma_1$ ,  $\sigma_2$  and  $\sigma_3$  as roots [Anand and Govindjee, 2020]. The polynomial coefficients are the so-called *principal invariants*

$$I_1(\boldsymbol{\sigma}) = \text{tr}(\boldsymbol{\sigma}) \quad (5.31a)$$

$$I_2(\boldsymbol{\sigma}) = \frac{1}{2} \cdot \left[ [\text{tr}(\boldsymbol{\sigma})]^2 - \text{tr}(\boldsymbol{\sigma}^2) \right] \quad (5.31b)$$

$$I_3(\boldsymbol{\sigma}) = \det[\boldsymbol{\sigma}] \quad (5.31c)$$

which hold the property of always having the same value for a given tensor regardless of the coordinate system orientation. It further is convenient to define the invariants of

the *deviatoric stress tensor*

$$\mathbf{s} := \boldsymbol{\sigma} - p \cdot \mathbf{I} = \boldsymbol{\sigma} - \frac{1}{3} \cdot \text{tr}(\boldsymbol{\sigma}) \cdot \mathbf{I} \quad (5.32)$$

where subtraction of the hydrostatic pressure from the normal stresses gives a traceless tensor  $\text{tr}(\mathbf{s}) = 0$ . In the same fashion as the principal invariants (5.31), the *deviatoric stress invariants* are

$$J_1(\mathbf{s}) = \text{tr}(\mathbf{s}) = 0 \quad (5.33a)$$

$$J_2(\mathbf{s}) = \frac{1}{2} \cdot \mathbf{s} : \mathbf{s} = \frac{1}{2} \cdot \|\mathbf{s}\|^2 \quad (5.33b)$$

$$J_3(\mathbf{s}) = \det[\mathbf{s}] \quad (5.33c)$$

where  $\|\mathbf{s}\| = \sqrt{\mathbf{s} : \mathbf{s}}$  denotes the Euclidean norm of  $\mathbf{s}$ . The von Mises yield criterion states that plastic yielding begins if the shear stress magnitude in form of the second deviatoric stress invariant  $J_2$  reaches a critical value. Thus, in its formulation, the von Mises yield criterion is pressure-insensitive, namely the hydrostatic pressure component  $p$  is not regarded in the determination of the plastic flow. In a state of pure shear  $\boldsymbol{\sigma} = \mathbf{s}$ , e.g.  $\sigma_{12} = \sigma_{21} = \tau$ , the  $J_2$  invariant and corresponding yield function are

$$J_2(\mathbf{s}) = \tau^2 \quad \rightarrow \quad \Phi(\boldsymbol{\sigma}, \mathbf{A}) := \sqrt{J_2(\mathbf{s}(\boldsymbol{\sigma}))} - \tau \quad (5.34)$$

where  $\tau = \tau_y(\mathbf{A})$  is introduced as the *shear yield stress* representing the critical value as a function of the hardening thermodynamic forces. Considering an uniaxial state of stress  $\boldsymbol{\sigma} = \sigma$ , e.g.  $\sigma_{11} = \sigma$ , the  $J_2$  invariant and corresponding yield function are

$$J_2(\mathbf{s}) = \frac{1}{3} \cdot \sigma^2 \quad \rightarrow \quad \Phi(\boldsymbol{\sigma}, \mathbf{A}) := \sqrt{3 \cdot J_2(\mathbf{s}(\boldsymbol{\sigma}))} - \sigma \quad (5.35)$$

where  $\sigma = \sigma_y(\mathbf{A})$  is introduced as the *uniaxial yield stress* representing the critical value as a function of the hardening thermodynamic forces. Therefore, the uniaxial and shear yield stress are related by

$$\sigma_y = \sqrt{3} \cdot \tau_y. \quad (5.36)$$

Throughout this work, the uniaxial form of the *von Mises yield function* is used as

$$\Phi(\boldsymbol{\sigma}, \mathbf{A}) := \sigma_v(\mathbf{s}(\boldsymbol{\sigma})) - \sigma_y(\mathbf{A}) \quad (5.37)$$

where  $\sigma_v$  is introduced as the *von Mises equivalent stress*

$$\sigma_v(\mathbf{s}(\boldsymbol{\sigma})) = \sqrt{3 \cdot J_2(\mathbf{s}(\boldsymbol{\sigma}))} = \sqrt{\frac{3}{2} \cdot \|\mathbf{s}(\boldsymbol{\sigma})\|^2}. \quad (5.38)$$

### 5.1.5 Plastic flow rule

As already defined, all plastically admissible stresses lie either within the elastic domain  $\mathcal{E}$  or on the yield surface  $\mathcal{Y}$ . For stress states within  $\mathcal{E}$  only purely elastic strains occur such that

$$\dot{\boldsymbol{\varepsilon}}^p = \mathbf{0} \quad \forall \boldsymbol{\sigma} \in \mathcal{E} \quad (5.39)$$

while on  $\mathcal{Y}$  either *elastic unloading* or *plastic loading* can occur

$$\left. \begin{array}{ll} \dot{\boldsymbol{\varepsilon}}^p = \mathbf{0} & \text{if } \textit{elastic unloading} \\ \dot{\boldsymbol{\varepsilon}}^p \neq \mathbf{0} & \text{if } \textit{plastic loading} \end{array} \right\} \forall \boldsymbol{\sigma} \in \mathcal{Y}. \quad (5.40)$$

Hence, all three cases define the conditions under which plastic flow takes place and shall be used to construct the plastic flow rule. The flow rule of multidimensional plasticity models is usually defined in terms of a *flow potential*  $\Psi(\boldsymbol{\sigma}, \mathbf{A})$ . So-called *associative flow rules*, which are widely used for ductile metals, employ the yield function  $\Phi(\boldsymbol{\sigma}, \mathbf{A})$  to be the flow potential under the assumption that the plastic strain rate is a tensor normal to the yield surface

$$\dot{\boldsymbol{\varepsilon}}^p := \dot{\gamma} \cdot \frac{\partial \Psi}{\partial \boldsymbol{\sigma}} := \dot{\gamma} \cdot \frac{\partial \Phi}{\partial \boldsymbol{\sigma}}, \quad \dot{\gamma} \geq 0. \quad (5.41)$$

An associative formulation of the flow rule is assumed throughout this work. The non-negative scalar  $\dot{\gamma}$  is the so-called *plastic multiplier* and satisfies the *complementary condition*

$$\Phi \cdot \dot{\gamma} = 0 \quad (5.42)$$

which implies that  $\dot{\gamma}$  vanishes in  $\mathcal{E}$  such that the condition (5.39) is satisfied and on  $\mathcal{Y}$  the plastic multiplier is  $\dot{\gamma} \geq 0$  for  $\Phi = 0$  which enables condition (5.40). If the hardening process is derived from the same potential, the associative assumption allows the evolution equation of the internal hardening variables

$$\dot{\alpha} := -\dot{\gamma} \cdot \frac{\partial \Psi}{\partial \mathbf{A}} := -\dot{\gamma} \cdot \frac{\partial \Phi}{\partial \mathbf{A}}. \quad (5.43)$$

This work uses the flow rule derived from the von Mises yield function (5.35) known as the *Prandtl-Reuss plasticity law*

$$\dot{\boldsymbol{\varepsilon}}^p = \dot{\gamma} \cdot \mathbf{N} \quad (5.44)$$

where  $\mathbf{N}$  is the *flow vector*

$$\mathbf{N} = \frac{\partial \Phi}{\partial \boldsymbol{\sigma}} = \frac{\partial}{\partial \boldsymbol{\sigma}} \left[ \sqrt{3 \cdot J_2(\mathbf{s}(\boldsymbol{\sigma}))} - \sigma_y(\mathbf{A}) \cdot \mathbf{I} \right] = \sqrt{\frac{3}{2}} \cdot \frac{\mathbf{s}}{\|\mathbf{s}\|}. \quad (5.45)$$

Using both, the *Prandtl-Reuss flow rule* and the *von Mises yield criterion* in conjunction is referred to as the *von Mises model*.

The associative law originates from the *principle of maximum plastic dissipation* which states that among all admissible pairs of  $(\sigma, A)$

$$\mathcal{A} = \{(\sigma, A) \mid \Phi(\sigma, A) \leq 0\} \quad (5.46)$$

the actual state of stress and internal hardening variables maximizes the plastic dissipation function (5.19)

$$\begin{aligned} \max \quad & Y^p(\sigma, A; \dot{\epsilon}^p, \alpha) \quad \forall (\sigma, A) \in \mathcal{A} \\ \text{subject to} \quad & \Phi(\sigma, A) \leq 0. \end{aligned} \quad (5.47)$$

The *Karush-Kuhn-Tucker optimality conditions* of this optimization problem are the primal feasibility in form of the yield function being non-positive, the dual feasibility represented by the plastic flow rule (5.41) and the complementary loading/unloading condition (5.42)

$$\Phi(\sigma, A) \leq 0 \quad \dot{\gamma} \geq 0 \quad \Phi(\sigma, A) \cdot \dot{\gamma} = 0. \quad (5.48)$$

### 5.1.6 Hardening law

As introduced with (5.35), the yield stress  $\sigma_y(A)$  is a function of the hardening thermodynamic force  $A$ . Essentially, the phenomenon of hardening is the dependence of the yield stress upon the history of the plastic strains during a deformation process. Essentially, the process of hardening can be categorized in *isotropic hardening* where the yield surface expands uniformly in tension and compression loading, and *kinematic hardening* where the yield surface translates rigidly under preservation of its shape. The direction of translation corresponds to the opposite direction in which the material was loaded, or in other words, the material shows a decreased resistance against compression after being tensioned and vice versa, known as the *Bauschinger effect*. Plasticity models without strain hardening are called *perfectly plastic* and the yield stress  $\sigma_y$  of the von Mises model is considered as a constant. Essentially, the kinematic hardening enables to capture material effects during cyclic loading. Since this work does not aim to investigate bodies under cyclic boundary conditions, the hardening is assumed to be isotropic.

For ductile metals, the internal hardening variables  $\alpha$  capture the hardening process through the density of dislocations in the crystallographic microstructure. Those dislocations are induced during plastic straining and cause the isotropic increase of the yield limit  $\sigma_y$ .

The isotropic hardening constitutive is usually treated by means of a single scalar variable in  $\alpha$ , either approached by so-called *strain hardening* or *work hardening*. In the

realm of the von Mises model, the scalar internal hardening variable for *strain hardening* is the *von Mises effective plastic strain* or *accumulated plastic strain*

$$\bar{\varepsilon}^p := \int_0^t \sqrt{\frac{2}{3} \cdot \dot{\varepsilon}^p : \dot{\varepsilon}^p} dt = \int_0^t \sqrt{\frac{2}{3}} \cdot \|\dot{\varepsilon}^p\| dt \quad (5.49)$$

since it accumulates the plastic strains regardless of its direction to ensure that both, tensile and compressive plastic straining contributes to the internal hardening variable. The *rate of accumulated plastic strain* simply follows by the integrand

$$\dot{\varepsilon}^p = \sqrt{\frac{2}{3} \cdot \dot{\varepsilon}^p : \dot{\varepsilon}^p} = \sqrt{\frac{2}{3}} \cdot \|\dot{\varepsilon}^p\|. \quad (5.50)$$

By the assumption of  $\alpha := \{\bar{\varepsilon}^p\}$ , the plastic free energy contribution in (5.15) is a function  $\psi^p = \psi^p(\bar{\varepsilon}^p)$ . Hence, the set of hardening thermodynamic forces is a single scalar as well

$$\mathbf{A} := \rho \cdot \frac{\partial \psi^p}{\partial \alpha} := \rho \cdot \frac{\partial \psi^p}{\partial \bar{\varepsilon}^p} \quad \rightarrow \quad \mathbf{A} := \{\kappa(\bar{\varepsilon}^p)\} \quad (5.51)$$

introduced as  $\kappa$ , the *scalar hardening thermodynamic force*. The hardening curve of the yield stress is postulated as a function of an *initial yield stress*  $\sigma_{y_0}$  and the accumulated plastic strain through  $\kappa(\bar{\varepsilon}^p)$

$$\sigma_y(\bar{\varepsilon}^p) := \sigma_{y_0} + \kappa(\bar{\varepsilon}^p), \quad \kappa(\bar{\varepsilon}^p) = \begin{cases} 0 & \text{perfect plasticity} \\ H \cdot \bar{\varepsilon}^p & \text{linear hardening} \\ H(\bar{\varepsilon}^p) & \text{nonlinear hardening} \end{cases} \quad (5.52)$$

where  $H$  is the *hardening modulus* which is generally obtained by

$$H(\bar{\varepsilon}^p) = \frac{\partial \sigma_y}{\partial \bar{\varepsilon}^p}. \quad (5.53)$$

The associative evolution of the hardening variables (5.43) provides

$$\dot{\alpha} := \dot{\varepsilon}^p := \dot{\gamma} \cdot \mathbf{H} \quad (5.54)$$

where the *associative generalized hardening modulus* shall be introduced with

$$\mathbf{H} := -\frac{\partial \Phi}{\partial \mathbf{A}} := -\frac{\partial \Phi}{\partial \kappa} = -\frac{\partial}{\partial \kappa} \left[ \sqrt{3 \cdot J_2(\mathbf{s}(\boldsymbol{\sigma}))} - [\sigma_{y_0} + \kappa(\bar{\varepsilon}^p)] \right] = 1 \quad (5.55)$$

yielding the identity

$$\dot{\varepsilon}^p = \dot{\gamma}. \quad (5.56)$$

In contrast to *strain hardening*, *work hardening* models assume the yield stress as a function of the *plastic work*

$$\sigma_y = \sigma_y(w^p) \quad \text{with} \quad w^p := \int_0^t \boldsymbol{\sigma} : \dot{\boldsymbol{\epsilon}}^p dt \quad (5.57)$$

being the area enclosed by the elastoplastic stress-strain-curve under loading and subsequent unloading back to a stress-free state. The von Mises model in this work uses isotropic strain hardening exclusively to cover the evolution of  $\sigma_y$ .

### 5.1.7 Summary of the elastoplastic model

Table 5.1 lists all components of the von Mises model with isotropic strain hardening.

Strain decomposition	$\boldsymbol{\epsilon} = \boldsymbol{\epsilon}^e + \boldsymbol{\epsilon}^p$
Specific free energy	$\psi = \psi^e(\boldsymbol{\epsilon}^e) + \psi^p(\boldsymbol{\alpha})$
Elastic constitutive law	$\boldsymbol{\sigma} = \mathbf{C}^e : \boldsymbol{\epsilon}^e = 2 \cdot G \cdot \boldsymbol{\epsilon}_d^e + K \cdot \boldsymbol{\epsilon}_v^e \cdot \mathbf{I}$
Yield function	$\Phi = \sqrt{3 \cdot J_2(\mathbf{s}(\boldsymbol{\sigma}))} - \sigma_y(\bar{\boldsymbol{\epsilon}}^p)$
Internal variables	$\boldsymbol{\alpha} = \{\bar{\boldsymbol{\epsilon}}^p\}, \quad \bar{\boldsymbol{\epsilon}}^p = \int_0^t \sqrt{\frac{2}{3}} \cdot \ \dot{\boldsymbol{\epsilon}}^p\  dt$
Hardening constitutive law	$\mathbf{A} = \{\kappa(\bar{\boldsymbol{\epsilon}}^p)\}$
Hardening curve	$\sigma_y = \sigma_{y_0} + \kappa(\bar{\boldsymbol{\epsilon}}^p)$
Plastic flow rule	$\dot{\boldsymbol{\epsilon}}^p = \dot{\gamma} \cdot \mathbf{N} = \dot{\gamma} \cdot \sqrt{\frac{3}{2}} \cdot \frac{\mathbf{s}(\boldsymbol{\sigma})}{\ \mathbf{s}(\boldsymbol{\sigma})\ }$
Hardening law	$\dot{\boldsymbol{\epsilon}}^p = \dot{\gamma} \cdot \mathbf{H} = \dot{\gamma} = \sqrt{\frac{2}{3}} \cdot \ \dot{\boldsymbol{\epsilon}}^p\ $
Karush-Kuhn-Tucker conditions	$\Phi \leq 0, \quad \dot{\gamma} \geq 0, \quad \Phi \cdot \dot{\gamma} = 0$

**Table 5.1** Tabular summary of the associative von Mises plasticity model with isotropic strain hardening.

## 5.2 Finite elements for elastoplasticity

To solve the plasticity problem by means of the finite element method, the equations of Table 5.1 are required in a temporally discrete formulation with so-called *pseudo-time* indicating an incremental time stepping in the elastoplastic process. Figure 5.2 illustrates the idea of the global/local solution procedure. While the elastoplastic constitutive problem is treated locally in each quadrature point, the load to which the body is subjected will be applied globally in an incremental fashion to solve for the displacements.

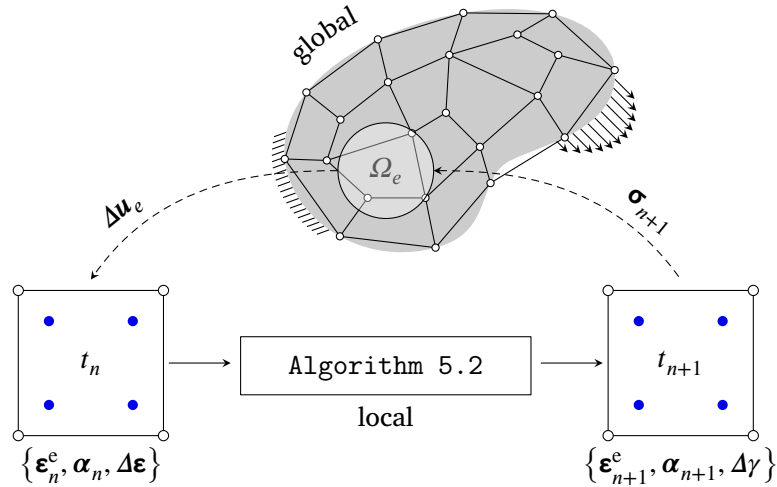


**Figure 5.2** Integration procedure of the elastoplastic material: The global solution of Algorithm 5.1 provides the incremental strains at the quadrature point  $\Delta\epsilon$  through the incremental displacements of the element  $\Delta u_e$ . The local Algorithm 5.2 updates the stresses  $\sigma_{n+1}$  for the global scheme to update the internal forces.

### 5.2.1 Euler discretization of the initial value problem

A material point at  $x$  of a body with domain  $\Omega$  shall be considered following the constitutive behavior stated in Table 5.1. Given the initial values of  $\epsilon^e(t_0)$  and of  $\alpha(t_0)$  as well as the history of the strain tensor  $\epsilon(t)$ ,  $t \in [t_0, \hat{t}]$ , the functions of the elastic strain tensor  $\epsilon^e(t)$ , the internal variables  $\alpha(t)$  and plastic multiplier  $\dot{\gamma}(t)$  shall be found which satisfy the elastoplastic constitutive equations

$$\dot{\epsilon}^e(t) = \dot{\epsilon}(t) - \dot{\epsilon}^p(t) = \dot{\epsilon}(t) - \dot{\gamma}(t) \cdot N(\sigma(t), A(t)) \quad (5.58a)$$

$$\dot{\alpha}(t) = \dot{\gamma}(t) \cdot H(\sigma(t), A(t)) \quad (5.58b)$$

$$\Phi(\sigma(t), A(t)) \leq 0, \quad \dot{\gamma}(t) \geq 0, \quad \Phi(\sigma(t), A(t)) \cdot \dot{\gamma}(t) = 0 \quad (5.58c)$$

for each time instant  $t \in [t_0, \hat{t}]$ , with

$$\sigma(t) = \rho \cdot \frac{\partial \psi}{\partial \epsilon^e} \Big|_t, \quad A(t) = \rho \cdot \frac{\partial \psi}{\partial \alpha} \Big|_t. \quad (5.59)$$

By employing a standard *implicit Euler time discretization*, the initial value problem (5.58) can be formulated within a pseudo-time interval  $[t_n, t_{n+1}]$  of size  $\Delta t$  where the continuous functions  $(\bullet)(t)$  are rewritten in the incremental format

$$(\bullet)_{n+1} = (\bullet)_n + \Delta(\bullet). \quad (5.60)$$

Thus now, given the elastic strain tensor  $\epsilon^e_n$  and internal variables  $\alpha_n$  at the beginning of the pseudo-time interval  $[t_n, t_{n+1}]$ , and given the strain increment  $\Delta\epsilon$  for this interval,

the system of algebraic equations

$$\boldsymbol{\varepsilon}_{n+1}^e = \boldsymbol{\varepsilon}_n^e + \Delta\boldsymbol{\varepsilon} - \Delta\boldsymbol{\varepsilon}^p = \boldsymbol{\varepsilon}_n^e + \Delta\boldsymbol{\varepsilon} - \Delta\gamma \cdot \mathbf{N}(\boldsymbol{\sigma}_{n+1}, \mathbf{A}_{n+1}) \quad (5.61a)$$

$$\boldsymbol{\alpha}_{n+1} = \boldsymbol{\alpha}_n + \Delta\gamma \cdot \mathbf{H}(\boldsymbol{\sigma}_{n+1}, \mathbf{A}_{n+1}) \quad (5.61b)$$

subjected to the constraints

$$\Phi(\boldsymbol{\sigma}_{n+1}, \mathbf{A}_{n+1}) \leq 0, \quad \Delta\gamma \geq 0, \quad \Phi(\boldsymbol{\sigma}_{n+1}, \mathbf{A}_{n+1}) \cdot \Delta\gamma = 0 \quad (5.62)$$

with

$$\boldsymbol{\sigma}_{n+1} = \rho \cdot \frac{\partial\psi}{\partial\boldsymbol{\varepsilon}^e} \Big|_{n+1}, \quad \mathbf{A}_{n+1} = \rho \cdot \frac{\partial\psi}{\partial\boldsymbol{\alpha}} \Big|_{n+1}. \quad (5.63)$$

shall be solved for the unknowns  $\boldsymbol{\varepsilon}_{n+1}$ ,  $\boldsymbol{\alpha}_{n+1}$  and  $\Delta\gamma$ .

### 5.2.2 Global incremental-iterative solution procedure

Following the incremental Euler scheme (5.60), the stress tensor at time instant  $t_{n+1}$  reads

$$\boldsymbol{\sigma}_{n+1} = \boldsymbol{\sigma}_n + \Delta\boldsymbol{\sigma} \quad (5.64)$$

which leads to a decomposition of the internal forces in the stationary equilibrium

$$\mathbf{f}_{n+1}^{\text{int}} = \mathbf{f}_{n+1}^{\text{ext}} \quad (5.65)$$

$$\begin{aligned} \mathbf{A} \int_e^{n_e} \mathbf{B}_e^\top \cdot \boldsymbol{\sigma}_{n+1} d\Omega &= \mathbf{f}_{n+1}^{\text{ext}} \\ \mathbf{A} \int_e^{n_e} \mathbf{B}_e^\top \cdot [\boldsymbol{\sigma}_n + \Delta\boldsymbol{\sigma}] d\Omega &= \mathbf{f}_{n+1}^{\text{ext}} \\ \mathbf{A} \int_e^{n_e} \mathbf{B}_e^\top \cdot \Delta\boldsymbol{\sigma} d\Omega &= \mathbf{f}_{n+1}^{\text{ext}} - \mathbf{A} \int_e^{n_e} \mathbf{B}_e^\top \cdot \boldsymbol{\sigma}_n d\Omega \\ \underbrace{\left[ \mathbf{A} \int_e^{n_e} \mathbf{B}_e^\top \cdot \mathbf{C}_n \cdot \mathbf{B}_e d\Omega \right]}_{\mathbf{K}_n} \cdot \Delta\mathbf{u} &= \mathbf{f}_{n+1}^{\text{ext}} - \mathbf{f}_n^{\text{int}} \end{aligned} \quad (5.66)$$

where the unknown  $\Delta\mathbf{u}$  is a vector of discrete displacement increments from which the engineering strain increments for the plastic flow rule (5.61a) are obtained via interpolation at the quadrature points

$$\Delta\boldsymbol{\varepsilon}(\xi) = \mathbf{B}_e(\xi) \cdot \Delta\mathbf{u}_e. \quad (5.67)$$

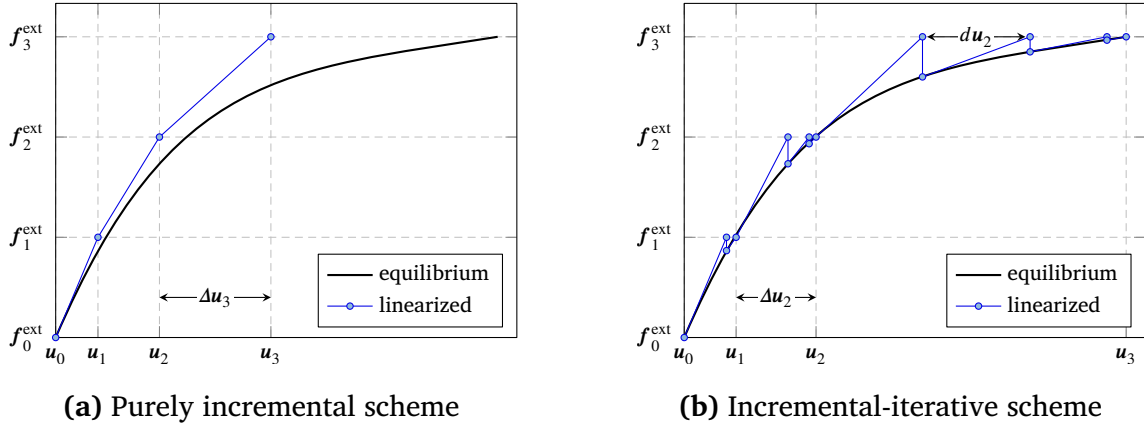


**Figure 5.3** Force-displacement curves of incremental solution schemes demonstrating the drift-away from the equilibrium path in a and the incremental-iterative *Newton-Raphson* scheme in b where the incremental solutions are corrected by iterating back onto the equilibrium path.

here written in Voigt vector notation on element level. In every tensor-involving equation however, the physical strains  $\boldsymbol{\epsilon}$  are assumed, thus one has to closely pay attention to their conversion rule (4.29).  $\mathbf{K}_n$  is now called the *tangent stiffness matrix* at time instant  $t_n$ ,  $\mathbf{r}_{n+1}$  is the residual vector and  $\mathbf{f}_{n+1}^{\text{ext}}$  is the vector containing all external loads applied to the system for the current load step  $[t_n, t_{n+1}]$ . In the case of nonlinear material behavior, like in plasticity, the material matrix  $\mathbf{C}_n$  is required to be updated for every load step and is now termed *consistent tangent modulus*.

### Load control

Applying the external load is usually achieved by a load step factor  $\lambda$  which scales a normalized vector of external forces  $\hat{\mathbf{f}}^{\text{ext}}$  to increment the load level. The linearized system of equations of the so-called *load-controlled* approach then reads

$$\mathbf{K}_n \cdot \Delta\mathbf{u}_{n+1} = \lambda_n \cdot \hat{\mathbf{f}}^{\text{ext}} - \mathbf{f}_n^{\text{int}}. \quad (5.68)$$

As depicted in Figure 5.3, the load is applied subsequently  $\mathbf{f}_n^{\text{ext}}, n = 1, 2, \dots, n_{\max}$  to solve for the displacements  $\mathbf{u}_n$  at the respective load level. Following the linearized form (5.68) yields a load-displacement curve which drifts away from the equilibrium path where  $\mathbf{r} = \mathbf{0}$ , as shown in Figure 5.3a. To obtain a linearized solution that follows the equilibrium path, the solution increment  $\Delta\mathbf{u}$  needs to be corrected iteratively. Those incremental-iterative approaches, like the one shown in Figure 5.3b, are known as *Newton-Raphson* schemes and are widely used to solve non-linear problems [De Borst et al., 2012]. Algorithm 5.1 shows the implemented solving approach where a correction  $d\mathbf{u}$  updates the displacement increments  $\Delta\mathbf{u}$  such that they converge towards the equilibrium where the residual norm vanishes  $\|\mathbf{r}\|_2 \rightarrow 0$ . For every load step  $n$ , the displacement increments are initialized as a zero vector and the external forces of the current load

step are computed. Now, for every iteration  $j$  the corrections  $d\mathbf{u}_{j+1}$  are computed by means of an updated tangent stiffness matrix  $\mathbf{K}_j$  and internal force vector  $\mathbf{f}_j^{\text{int}}$ . The displacement and strain increments are updated by their respective corrections. After updating the stress tensor with Algorithm 5.2, using the elastoplastic constitutive equations, the internal forces can be evaluated in the corrected state. The solution is considered as converged if the residual norm falls below a tolerance  $\epsilon \approx 0$ . If a user-defined maximum of iterations  $j_{\max}$  is reached, the iterative process is terminated as well as the incremental load stepping. After successful convergence, the load step factor is incremented by  $\Delta\lambda$  in preparation for the next load step.

**Algorithm 5.1** The global incremental-iterative *Newton-Raphson* scheme, with a convergence tolerance  $0 < \epsilon \lll 1$ , the load step factor increment, typically  $\Delta\lambda = 1$ , the total number of load steps  $n_{\max}$  and the maximum number of corrective iterations  $j_{\max}$ . The procedure can be found for example in [De Borst et al., 2012].

---

```

1    $\lambda_n = 1$ 
2   for  $n = 1, 2, \dots, n_{\max}$ 
3      $\mathbf{f}_{n+1}^{\text{ext}} = \lambda_n \cdot \hat{\mathbf{f}}^{\text{ext}}$ 
4      $j = 0, \Delta\mathbf{u}_j = \mathbf{0}$ 
5     while  $\|\mathbf{r}_{j+1}\| > \epsilon \wedge j < j_{\max}$ 
6        $\mathbf{K}_j = \mathbf{A}_e^{n_e} \int_{\Omega_e} \mathbf{B}_e^\top \cdot \mathbf{C}_j \cdot \mathbf{B}_e d\Omega$ 
7        $\mathbf{K}_j \cdot d\mathbf{u}_{j+1} = \mathbf{f}_{n+1}^{\text{ext}} - \mathbf{f}_j^{\text{int}}$ 
8        $\Delta\mathbf{u}_{j+1} = \Delta\mathbf{u}_j + d\mathbf{u}_{j+1}$ 
9        $\Delta\boldsymbol{\varepsilon}_{j+1} = \Delta\boldsymbol{\varepsilon}_j + d\boldsymbol{\varepsilon}_{j+1}(d\mathbf{u}_{j+1})$ 
10      Find  $\boldsymbol{\sigma}_{j+1}(\Delta\boldsymbol{\varepsilon}_{j+1})$  with Algorithm 5.2
11       $\mathbf{f}_{j+1}^{\text{int}} = \int_{\Omega_e} \mathbf{B}_e^\top \cdot \boldsymbol{\sigma}_{j+1} d\Omega$ 
12       $\|\mathbf{r}_{j+1}\|_2 = \|\mathbf{f}_{n+1}^{\text{ext}} - \mathbf{f}_{j+1}^{\text{int}}\|_2$ 
13       $j = j + 1$ 
14    endwhile
15    if  $j = j_{\max}$ 
16      error ( No convergence within  $j_{\max}$  iterations. )
17    else
18       $\lambda_{n+1} = \lambda_n + \Delta\lambda$ 
19    endif
20  endfor
```

---

The so-called *load-controlled* increment scheme proposed up to this point works well for monotonic curves. However, as Figure 5.4a depicts, it can lose stability if extrema are present. In the case of the local maximum, the iterative solution hits the equilibrium path at or near the point with a zero slope where the tangent stiffness matrix is ill-

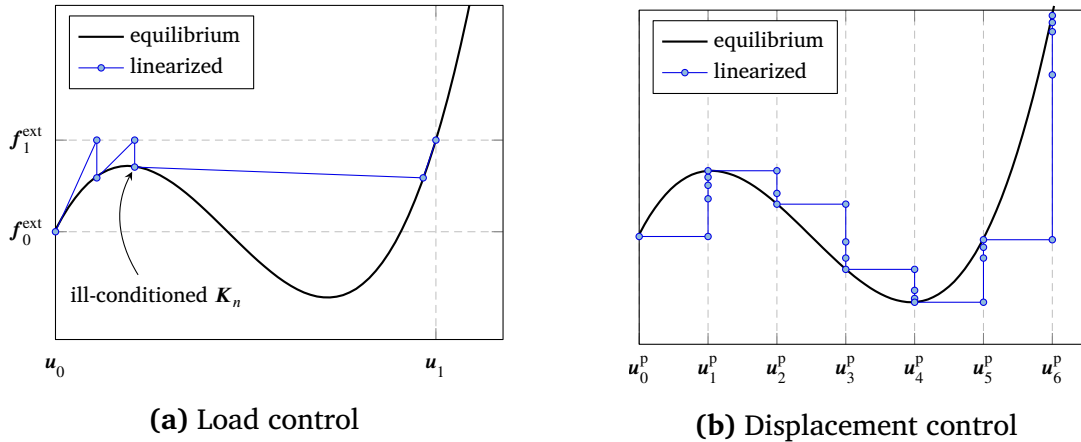


**Figure 5.4** Force-displacement curves of incremental-iterative solution schemes depicting the *snap-through* of a load-controlled solver at a local maximum in a and a displacement-controlled scheme in b where the solutions are prescribed incrementally on the Dirichlet boundary.

conditioned or even singular. Assuming a linear solver that does not fail to solve the system at this point, the Newton-Raphson scheme searches for the next intersection with the equilibrium path in the direction given by  $\mathbf{K}_n$ . For a local maximum, an intersection and thereby a solution can be found, but a significant part of the material behavior is skipped such that information is lost. If a global extremum is present the solver diverges since no intersection with the equilibrium path can be found. To tackle this problem, a *displacement-controlled* solver can be employed where the load stepping is implicitly performed by prescribed displacements.

### Displacement control

As depicted in Figure 5.4b, the displacements  $\mathbf{u}_n^P$  are fixed during the iterations such that the material characteristics after the local maximum can be captured by iteratively updating the displacement increments until the equilibrium force is reached. Just like in the procedure introduced in (2.35), the prescribed and free degrees of freedom are split into separate vectors such that the prescribed displacements can form a force equivalent on the right-hand side

$$\begin{bmatrix} \mathbf{K}_{ff} & \mathbf{K}_{fp} \\ \mathbf{K}_{pf} & \mathbf{K}_{pp} \end{bmatrix}_j \cdot \begin{bmatrix} \Delta\mathbf{u}_f \\ \Delta\mathbf{u}_p \end{bmatrix}_{j+1} = \begin{bmatrix} \mathbf{f}_f^{\text{ext}} \\ \mathbf{f}_p^{\text{ext}} \end{bmatrix}_{j+1} - \begin{bmatrix} \mathbf{f}_f^{\text{int}} \\ \mathbf{f}_p^{\text{int}} \end{bmatrix}_j. \quad (5.69)$$

Assuming no external forces along with the prescribed displacement increments  $\Delta\mathbf{u}_p$ , the linear system of equations for the first iteration reads

$$\mathbf{K}_{ff_j} \cdot \Delta\mathbf{u}_{f_{j+1}} = -\mathbf{K}_{fp_j} \cdot \Delta\mathbf{u}_{p_{j+1}} - \mathbf{f}_{f_j}^{\text{int}}, \quad j = 0 \quad (5.70)$$

while the prescribed displacement increments vanish for the following iterations of the load step such that

$$\mathbf{K}_{\text{ff}_j} \cdot \Delta \mathbf{u}_{f_{j+1}} = -\mathbf{f}_{f_j}^{\text{int}}, \quad j = 1, 2, \dots . \quad (5.71)$$

According to [De Borst et al., 2012], the reduced matrix  $\mathbf{K}_{\text{ff}}$  is better conditioned than the full matrix in a load-controlled scheme and does not become singular in extrema. In general, a better conditioned stiffness matrix leads to a faster convergence behavior.

### 5.2.3 Elastic predictor return mapping algorithm

Due to the Karush-Kuhn-Tucker conditions (5.62), the initial value problem cannot be treated by the standard Euler scheme directly. The constraint of the incremental plastic multiplier  $\Delta\gamma \geq 0$  however, recovers the distinction between a stress state in the purely elastic domain  $\mathcal{E}$  and on the yield surface  $\mathcal{Y}$  by defining two mutually exclusive states which can be treated straight-forward:

1. A purely elastic step within  $[t_n, t_{n+1}]$  where no plastic flow and no evolution of internal variables takes place with an incremental plastic multiplier of

$$\Delta\gamma = 0 \quad (5.72)$$

and the yield function constraint

$$\Phi(\boldsymbol{\sigma}, \mathbf{A}) \leq 0. \quad (5.73)$$

2. A plastic step within  $[t_n, t_{n+1}]$  where plastic flow occurs and internal variables change with an incremental plastic multiplier of

$$\Delta\gamma > 0 \quad (5.74)$$

and the yield function constraint

$$\Phi(\boldsymbol{\sigma}, \mathbf{A}) = 0. \quad (5.75)$$

Whether to accept the final valid solution from the elastic or the plastic equations motivates an algorithm that employs the equations in two subsequent steps. This so-called *elastic predictor return mapping algorithm* shown in Figure 5.5a first assumes an elastic step  $[t_n, t_{n+1}]$  with  $\Delta\lambda = 0$  such that (5.61) yields an *elastic trial solution*

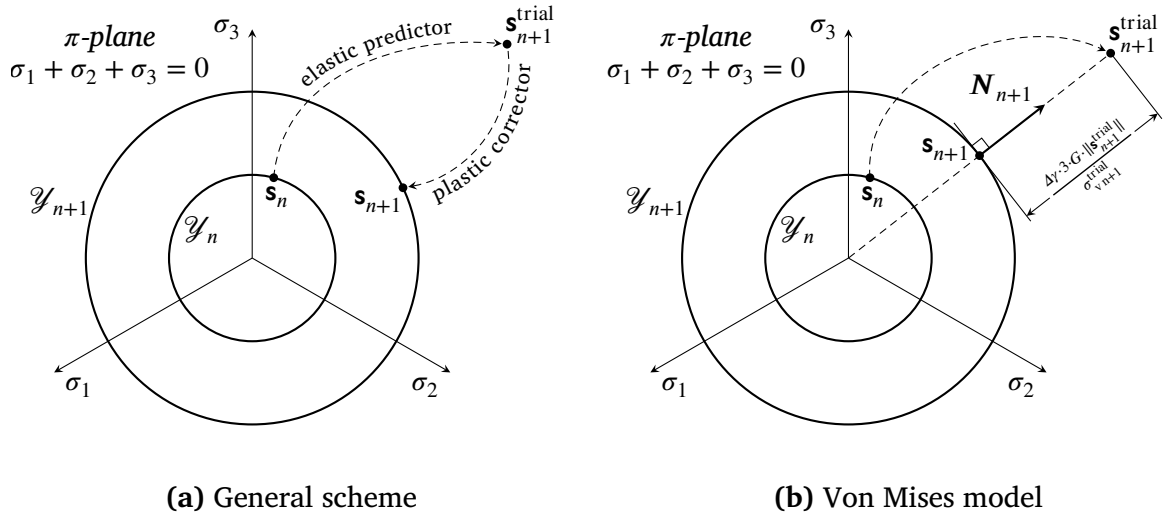


**Figure 5.5** The implicit elastic predictor return mapping under isotropic hardening. The scheme represents the geometric interpretation of the yield surface  $\mathcal{Y}$  at an initial time instant  $t_n$  and the isotropically hardened yield surface at  $t_{n+1}$ . The normal vector of the *deviatoric plane* or  $\pi$ -*plane* in the principal stress space  $(\sigma_1, \sigma_2, \sigma_3)$  coincides with the hydrostatic axis of the infinite cylinder where  $\sigma_1 = \sigma_2 = \sigma_3$ .

$$(\boldsymbol{\varepsilon}_{n+1}^e, \boldsymbol{\alpha}_{n+1}^e)$$

$$\boldsymbol{\varepsilon}_{n+1}^e = \boldsymbol{\varepsilon}_n^e + \Delta \boldsymbol{\varepsilon} \quad (5.76a)$$

$$\boldsymbol{\alpha}_{n+1}^e = \boldsymbol{\alpha}_n. \quad (5.76b)$$

The corresponding *elastic trial state*  $(\boldsymbol{\sigma}_{n+1}^{\text{trial}}, \mathbf{A}_{n+1}^{\text{trial}})$  is obtained by

$$\boldsymbol{\sigma}_{n+1}^{\text{trial}} = \rho \cdot \frac{\partial \psi}{\partial \boldsymbol{\varepsilon}^e} \Big|_{n+1}^{\text{trial}} = \mathbf{C}^e : \boldsymbol{\varepsilon}_{n+1}^{\text{trial}} \quad (5.77)$$

and in case of the proposed assumption  $\boldsymbol{\alpha} := \{\bar{\boldsymbol{\varepsilon}}^p\}$

$$\mathbf{A}_{n+1}^{\text{trial}} = \rho \cdot \frac{\partial \psi}{\partial \boldsymbol{\alpha}} \Big|_{n+1}^{\text{trial}} := \kappa(\boldsymbol{\alpha}_{n+1}^{\text{trial}}) = \kappa(\bar{\boldsymbol{\varepsilon}}_{n+1}^{\text{trial}}). \quad (5.78)$$

If the elastic trial state is plastically admissible, that is

$$\Phi(\boldsymbol{\sigma}_{n+1}^{\text{trial}}, \mathbf{A}_{n+1}^{\text{trial}}) \leq 0 \quad \rightarrow \quad (\boldsymbol{\sigma}_{n+1}^{\text{trial}}, \mathbf{A}_{n+1}^{\text{trial}}) \in \mathcal{A} \quad (5.79)$$

it is accepted as a solution and all variables are updated by

$$(\bullet)_{n+1} = (\bullet)_{n+1}^{\text{trial}}. \quad (5.80)$$

Otherwise, the plastic admissibility of the trial state is not satisfied, and a second step is required, namely, the *return mapping* also referred to as the *plastic corrector step*.

Therefore, the constrained system of equations (5.61) and (5.62) is rewritten in terms of the elastic trial solution to

$$\boldsymbol{\epsilon}_{n+1}^e = \boldsymbol{\epsilon}_{n+1}^{e\text{trial}} - \Delta\gamma \cdot \mathbf{N}(\boldsymbol{\sigma}_{n+1}, \mathbf{A}_{n+1}) \quad (5.81a)$$

$$\boldsymbol{\alpha}_{n+1} = \boldsymbol{\alpha}_{n+1}^{\text{trial}} + \Delta\gamma \cdot \mathbf{H}(\boldsymbol{\sigma}_{n+1}, \mathbf{A}_{n+1}) \quad (5.81b)$$

$$\Phi(\boldsymbol{\sigma}_{n+1}, \mathbf{A}_{n+1}) = 0 \quad (5.81c)$$

for which the return mapping shall find a solution  $\boldsymbol{\epsilon}_{n+1}^e$ ,  $\boldsymbol{\alpha}_{n+1}$  and  $\Delta\gamma$  that satisfies  $\Delta\gamma > 0$ . The implicit elastic predictor return mapping is summarized in Algorithm 5.2. Here, *implicit* refers to the initially applied implicit Euler scheme from which the algorithm is derived.

---

**Algorithm 5.2** General implicit elastic predictor return mapping algorithm with given strain increment  $\Delta\boldsymbol{\epsilon}$  and known state variables  $\boldsymbol{\epsilon}_n^e$ ,  $\boldsymbol{\alpha}_n$  at time instant  $t_n$ .

---

```

1    $\boldsymbol{\epsilon}_{n+1}^{\text{trial}} = \boldsymbol{\epsilon}_n^e + \Delta\boldsymbol{\epsilon}$ 
2    $\boldsymbol{\alpha}_{n+1}^{\text{trial}} = \boldsymbol{\alpha}_n$ 
3    $\boldsymbol{\sigma}_{n+1}^{\text{trial}} = \mathbf{C}^e : \boldsymbol{\epsilon}_{n+1}^{\text{trial}}$ 
4    $\mathbf{A}_{n+1}^{\text{trial}} = \rho \cdot \frac{\partial \psi}{\partial \boldsymbol{\alpha}} \Big|_{n+1}^{\text{trial}}$ 
5   if  $\Phi(\boldsymbol{\sigma}_{n+1}^{\text{trial}}, \mathbf{A}_{n+1}^{\text{trial}}) \leq 0$ 
6      $(\bullet)_{n+1} = (\bullet)_{n+1}^{\text{trial}}$ 
7   else
8     Solve return mapping equations (5.81) for  $(\boldsymbol{\epsilon}_{n+1}^e, \boldsymbol{\alpha}_{n+1}, \Delta\gamma)$  with  $\Delta\gamma > 0$ 
9      $\boldsymbol{\sigma}_{n+1} = \mathbf{C}^e : \boldsymbol{\epsilon}_{n+1}^e$ 
10     $\mathbf{A}_{n+1}^{\text{trial}} = \rho \cdot \frac{\partial \psi}{\partial \boldsymbol{\alpha}} \Big|_{n+1}$ 
11  endif

```

---

In the implemented von Mises model with isotropic strain hardening, the return mapping equations (5.81) are identified through Table 5.1 as

$$\boldsymbol{\epsilon}_{n+1}^e = \boldsymbol{\epsilon}_{n+1}^{\text{trial}} - \Delta\gamma \cdot \sqrt{\frac{3}{2}} \cdot \frac{\mathbf{s}_{n+1}}{\|\mathbf{s}_{n+1}\|} \quad (5.82a)$$

$$\bar{\boldsymbol{\epsilon}}_{n+1}^p = \bar{\boldsymbol{\epsilon}}_{n+1}^{\text{trial}} + \Delta\gamma \quad (5.82b)$$

$$\sigma_v(\mathbf{s}_{n+1}) - \sigma_y(\bar{\boldsymbol{\epsilon}}_{n+1}^p) = 0. \quad (5.82c)$$

The above system with unknowns  $\boldsymbol{\epsilon}_{n+1}^e$ ,  $\bar{\boldsymbol{\epsilon}}_{n+1}^p$  and  $\Delta\gamma$  can be significantly simplified to a single nonlinear equation with only  $\Delta\gamma$  as an unknown. Since the Prandtl-reuss flow vector is purely deviatoric, the volumetric strains as well as the hydrostatic pressure are directly accepted in their trial state. With the relation  $\mathbf{s} = 2 \cdot G \cdot \boldsymbol{\epsilon}_d^e$ , see (5.25), the

deviatoric strains and stresses are obtained by

$$\boldsymbol{\epsilon}_{d,n+1}^e = \boldsymbol{\epsilon}_{d,n+1}^{e,\text{trial}} - \Delta\gamma \cdot \sqrt{\frac{3}{2}} \cdot \frac{\mathbf{s}_{n+1}}{\|\mathbf{s}_{n+1}\|} \quad (5.83\text{a})$$

$$\mathbf{s}_{n+1} = \mathbf{s}_{n+1}^{\text{trial}} - \Delta\gamma \cdot 2 \cdot G \cdot \sqrt{\frac{3}{2}} \cdot \frac{\mathbf{s}_{n+1}}{\|\mathbf{s}_{n+1}\|}. \quad (5.83\text{b})$$

Per rearrangement of equation (5.83b) to

$$\mathbf{s}_{n+1}^{\text{trial}} = \left[ 1 + \sqrt{\frac{3}{2}} \cdot \frac{\Delta\gamma \cdot 2 \cdot G}{\|\mathbf{s}_{n+1}\|} \right] \cdot \mathbf{s}_{n+1} \quad \rightarrow \quad \frac{\mathbf{s}_{n+1}}{\|\mathbf{s}_{n+1}\|} = \frac{\mathbf{s}_{n+1}^{\text{trial}}}{\|\mathbf{s}_{n+1}^{\text{trial}}\|} \quad (5.84)$$

the trial and updated deviatoric stresses turn out to be collinear, namely just a scaling factor relating the two coinciding tensors. Considering the collinearity and the relations (5.33b) and (5.37), equation (5.84) can be reformulated to

$$\mathbf{s}_{n+1} = \left[ 1 - \sqrt{\frac{3}{2}} \cdot \frac{\Delta\gamma \cdot 2 \cdot G}{\|\mathbf{s}_{n+1}^{\text{trial}}\|} \right] \cdot \mathbf{s}_{n+1}^{\text{trial}} = \left[ 1 - \frac{\Delta\gamma \cdot 3 \cdot G}{\sigma_v(\mathbf{s}_{n+1}^{\text{trial}})} \right] \cdot \mathbf{s}_{n+1}^{\text{trial}}. \quad (5.85)$$

Thus, with  $\mathbf{s}_{n+1}^{\text{trial}}$  being a constant tensor during the return mapping, the updated deviatoric stresses are only in linear dependence of  $\Delta\gamma$ . In other words,  $\mathbf{s}_{n+1}^{\text{trial}}$  is scaled down during the return mapping to obtain  $\mathbf{s}_{n+1}$  which Figure 5.5b illustrates in a geometric interpretation. Substituting the reformulated expression for  $\mathbf{s}_{n+1}$  into the plastic consistency equation (5.82c) together with (5.82b) reduces the system of nonlinear equations to a single scalar return mapping equation

$$r(\Delta\gamma) := \sigma_v(\mathbf{s}_{n+1}^{\text{trial}}) - 3 \cdot G \cdot \Delta\gamma - \sigma_y(\bar{\epsilon}_{n+1}^{p,\text{trial}} + \Delta\gamma) = 0 \quad (5.86)$$

which can be solved by means of a Newton-Raphson scheme. Algorithm 5.3 shows the entire implicit elastic predictor return mapping Algorithm 5.2 specifically adapted to the von Mises plasticity model with isotropic strain hardening. It shall be noted that for perfect plasticity and linear hardening, the return mapping can be performed by a closed-form solution, or if a Newton-Raphson solver is used, within a single iteration.

**Algorithm 5.3** Von Mises model with isotropic strain hardening: Implicit elastic predictor return mapping algorithm with given strain increment  $\Delta\boldsymbol{\epsilon}$ , known state variables  $\boldsymbol{\epsilon}_n^e, \alpha_n$  at time instant  $t_n$ , maximum number of return mapping iterations  $k_{\max}$  and a convergence tolerance  $0 < \epsilon \ll 1$ .

---

- 1  $\boldsymbol{\epsilon}_{n+1}^{e,\text{trial}} = \boldsymbol{\epsilon}_n^e + \Delta\boldsymbol{\epsilon}$

- 2  $\bar{\epsilon}_{n+1}^{p,\text{trial}} = \bar{\epsilon}_n$

- 3  $p_{n+1}^{\text{trial}} = K \cdot \epsilon_{vn+1}^{e,\text{trial}}$

- 4  $\mathbf{s}_{n+1}^{\text{trial}} = 2 \cdot G \cdot \boldsymbol{\epsilon}_{d,n+1}^{e,\text{trial}}$

```

5    $\sigma_v^{\text{trial}} = \sqrt{\frac{3}{2}} \cdot \|\mathbf{s}_{n+1}^{\text{trial}}\|$ 
6   if  $\sigma_v^{\text{trial}} - \sigma_y(\bar{\varepsilon}_{n+1}^{\text{p trial}}) \leq 0$ 
7      $(\bullet)_{n+1} = (\bullet)_{n+1}^{\text{trial}}$ 
8   else
9      $k = 0$ 
10     $\Delta\gamma_{(k)} = 0$ 
11     $r_k = \sigma_v^{\text{trial}} - 3 \cdot G \cdot \Delta\gamma_{(k+1)} - \sigma_y(\bar{\varepsilon}_{n+1}^{\text{p trial}})$ 
12    while  $|r_k| > 0 \wedge k < k_{\max}$ 
13       $H = \frac{d\sigma_y}{d\bar{\varepsilon}^{\text{p}}} \Big|_{\bar{\varepsilon}_n^{\text{p}} + \Delta\gamma_{(k)}}$ 
14       $d = \frac{dr_k}{d\Delta\gamma} = -3 \cdot G - H$ 
15       $\Delta\gamma_{(k+1)} = \Delta\gamma_{(k)} - \frac{r_k}{d}$ 
16       $r_{k+1} = \sigma_v^{\text{trial}} - 3 \cdot G \cdot \Delta\gamma_{(k+1)} - \sigma_y(\bar{\varepsilon}_{n+1}^{\text{p trial}} + \Delta\gamma_{(k+1)})$ 
17       $k = k + 1$ 
18  endwhile
19  if  $k = k_{\max}$ 
20    error ( No convergence within  $k_{\max}$  iterations. )
21  else
22     $p_{n+1} = p_{n+1}^{\text{trial}}$ 
23     $\mathbf{s}_{n+1} = \left[1 - \Delta\gamma \cdot 3 \cdot G / \sigma_v^{\text{trial}}\right] \cdot \mathbf{s}_{n+1}^{\text{trial}}$ 
24     $\boldsymbol{\sigma}_{n+1} = \mathbf{s}_{n+1} + p_{n+1} \cdot \mathbf{I}$ 
25     $\boldsymbol{\varepsilon}_{n+1}^{\text{e}} = \frac{1}{2G} \cdot \mathbf{s}_{n+1} + \frac{1}{3} \cdot \boldsymbol{\varepsilon}_{v,n+1}^{\text{e trial}} \cdot \mathbf{I}$ 
26     $\bar{\varepsilon}_{n+1}^{\text{p}} = \bar{\varepsilon}_n + \Delta\gamma$ 
27  endif

```

---

### 5.2.4 Elastoplastic consistent tangent operator

During the global Algorithm 5.1, the consistent tangent operator  $\mathbf{C}_j$  for the current Newton-Raphson iteration  $j$  is required to update the tangent stiffness matrix  $\mathbf{K}_j$  according to the current elastoplastic state. For a purely elastic state, the stresses are an explicit function of the plastically admissible elastic strains following equation (5.25) as

$$\boldsymbol{\sigma}_{n+1} = \boldsymbol{\sigma}(\boldsymbol{\varepsilon}^{\text{e}}) := \mathbf{C}^{\text{e}} : \boldsymbol{\varepsilon}^{\text{e}} = \mathbf{s} + p \cdot \mathbf{I} = 2 \cdot G \cdot \boldsymbol{\varepsilon}_{\text{d}}^{\text{e}} + K \cdot \boldsymbol{\varepsilon}_{\text{v}}^{\text{e}} \cdot \mathbf{I} \quad (5.87)$$

wherein the consistent tangent operator is exactly the standard fourth order isotropic linear elasticity tensor

$$\mathbf{C}^{\text{e}} := \frac{\partial \boldsymbol{\sigma}}{\partial \boldsymbol{\varepsilon}^{\text{e}}} = 2 \cdot G \cdot \mathbf{I}_{\text{d}} + K \cdot \mathbf{I} \otimes \mathbf{I} \quad (5.88)$$

with  $\mathbf{I}_d$  being the fourth order deviatoric projection tensor

$$\mathbf{I}_d := \mathbf{I}^{\text{sym}} - \frac{1}{3} \cdot \mathbf{I} \otimes \mathbf{I} \quad (5.89)$$

which projects second order symmetric tensors into the deviatoric space of traceless tensors, for example, the deviatoric stress  $\mathbf{s} = \mathbf{I}_d : \boldsymbol{\sigma}$ . In the three-dimensional space, the fourth order deviatoric projection tensor  $\mathbf{I}_d$  and the fourth order symmetric identity tensor  $\mathbf{I}^{\text{sym}}$  can be represented by the matrices

$$\mathbf{I}_d := \begin{bmatrix} \frac{2}{3} & -\frac{1}{3} & -\frac{1}{3} & 0 & 0 & 0 \\ -\frac{1}{3} & \frac{2}{3} & -\frac{1}{3} & 0 & 0 & 0 \\ -\frac{1}{3} & -\frac{1}{3} & \frac{2}{3} & 0 & 0 & 0 \\ 0 & 0 & 0 & \frac{1}{2} & 0 & 0 \\ 0 & 0 & 0 & 0 & \frac{1}{2} & 0 \\ 0 & 0 & 0 & 0 & 0 & \frac{1}{2} \end{bmatrix}, \quad \mathbf{I}^{\text{sym}} := \begin{bmatrix} 1 & 0 & 0 & 0 & 0 & 0 \\ 0 & 1 & 0 & 0 & 0 & 0 \\ 0 & 0 & 1 & 0 & 0 & 0 \\ 0 & 0 & 0 & \frac{1}{2} & 0 & 0 \\ 0 & 0 & 0 & 0 & \frac{1}{2} & 0 \\ 0 & 0 & 0 & 0 & 0 & \frac{1}{2} \end{bmatrix}. \quad (5.90)$$

In the case of a plastic state however, stress update  $\boldsymbol{\sigma}_{n+1}$  is an implicit function of the elastic trial strains  $\boldsymbol{\varepsilon}_{n+1}^{\text{trial}}$  defined by the return mapping equations which can be formulated using equation (5.85) and the elastic law (5.87) to

$$\begin{aligned} \boldsymbol{\sigma}_{n+1} &= \boldsymbol{\sigma}_{n+1}(\boldsymbol{\varepsilon}_{n+1}^{\text{trial}}) = \mathbf{s}_{n+1} + p_{n+1} \cdot \mathbf{I} \\ &= \left[ 1 - \frac{\Delta\gamma \cdot 3 \cdot G}{\sigma_v(\mathbf{s}_{n+1}^{\text{trial}})} \right] \cdot \mathbf{s}_{n+1}^{\text{trial}} + p_{n+1}^{\text{trial}} \cdot \mathbf{I} \\ &= \left[ \mathbf{C}^e - \frac{\Delta\gamma \cdot 6 \cdot G^2}{\sigma_v(\mathbf{s}_{n+1}^{\text{trial}})} \cdot \mathbf{I}_d \right] : \boldsymbol{\varepsilon}_{n+1}^{\text{trial}} \end{aligned} \quad (5.91)$$

such that the elastoplastic consistent tangent operator can be derived by the application of tensor differentiation rules

$$\begin{aligned} \mathbf{C}^{\text{ep}} &:= \frac{\partial \boldsymbol{\sigma}_{n+1}}{\partial \boldsymbol{\varepsilon}_{n+1}^{\text{trial}}} \\ &= \mathbf{C}^e - \frac{\Delta\gamma \cdot 6 \cdot G^2}{\sigma_v(\mathbf{s}_{n+1}^{\text{trial}})} \cdot \mathbf{I}_d \\ &\quad + 6 \cdot G^2 \cdot \left[ \frac{\Delta\gamma}{\sigma_v(\mathbf{s}_{n+1}^{\text{trial}})} - \frac{1}{3 \cdot G + H(\bar{\varepsilon}_{n+1}^{\text{trial}} + \Delta\gamma)} \right] \cdot \frac{\mathbf{s}_{n+1}^{\text{trial}}}{\|\mathbf{s}_{n+1}^{\text{trial}}\|} \otimes \frac{\mathbf{s}_{n+1}^{\text{trial}}}{\|\mathbf{s}_{n+1}^{\text{trial}}\|} \end{aligned} \quad (5.92)$$

or for an implementation more conveniently written in Algorithm 5.4. Naturally, at the time point of evaluating the tangent operator  $\mathbf{C}_j^{\text{ep}}$  for the tangent stiffness matrix  $\mathbf{K}_j$ , the values of  $\boldsymbol{\sigma}_{n+1}$ ,  $\Delta\gamma$  and  $\bar{\varepsilon}_{n+1}^{\text{p}}$  are the ones from the previous global iteration  $j - 1$  which were obtained the return mapping Algorithm 5.3.

**Algorithm 5.4** Von Mises model with isotropic strain hardening: Computation of the three-dimensional elastoplastic consistent tangent operator  $\mathbf{C}^{\text{ep}}$ .

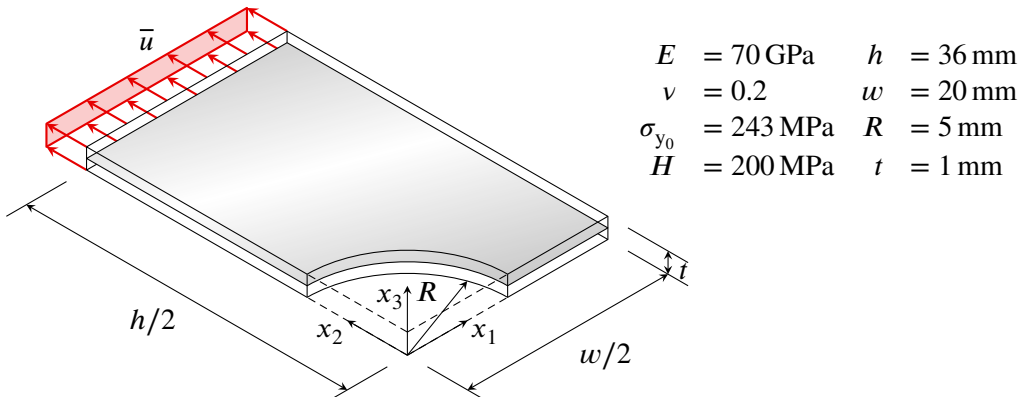


**Figure 5.6** A symmetric quarter of the perforated plate benchmark. The plate is stretched by prescribed displacements at the top surface and constrained with symmetry boundary conditions at the cut faces at  $x_2 = 0$  and  $x_1 = 0$  as well as constrained on the back normal to the face to provide the assumptions for the plane stress theory.

---

```

1   $p_{n+1} = \frac{1}{3} \cdot \text{tr}(\sigma_{n+1})$ 
2   $\mathbf{s}_{n+1} = \sigma_{n+1} - p_{n+1} \cdot \mathbf{I}$ 
3   $\sigma_{vn+1} = \sqrt{\frac{3}{2}} \cdot \|\mathbf{s}_{n+1}\| + 3 \cdot G \cdot \Delta\gamma$ 
4   $a = 2 \cdot G \cdot \left[ 1 - \frac{3 \cdot G \cdot \Delta\gamma}{\sigma_{vn+1}} \right]$ 
5   $b = \frac{6 \cdot G^2}{\|\mathbf{s}_{n+1}\|^2} \cdot \left[ \frac{\Delta\gamma}{\sigma_{vn+1}} - \frac{1}{3 \cdot G \cdot H(\bar{\epsilon}_{n+1}^p)} \right]$ 
6  for i = 1, 2, ..., 6
7    for j = 1, 2, ..., 6
8       $[\mathbf{C}^p]_{ij} = a \cdot [\mathbf{I}_d]_{ij} + b \cdot [\mathbf{s}_{n+1} \otimes \mathbf{s}_{n+1}]_{ij} + K \cdot [\mathbf{I} \otimes \mathbf{I}]_{ij}$ 
9    endfor
10 endfor

```

---

## 5.3 Perforated plate benchmark

The introduced elastoplastic von Mises model with isotropic hardening is verified against a plane stress reference analysis done by [de Souza Neto et al., 2011]. Figure 5.6 depicts the model set up. The material is assumed to have an initial yield stress of  $\sigma_{y_0} = 243$  MPa and a linear hardening with slope  $H = 200$  MPa. For the analysis, the finite cell method is utilized with  $5 \times 9 \times 2$  cells of polynomial order  $p = 2$ . During the verification, the non-negative moment fitting is applied in comparison to the adaptive spacetime quadrature. The multi-level  $hp$ -refinement is applied in three uniform cycles  $i = 1, \dots, 3$ , each time based on the field solution in the final load step.

### Note on the refinement metric

To decide which cells shall be refined with overlays, the so-called *Kelly estimator* is employed as a refinement metric. Herein, the cells are adaptively refined based on the badness of discontinuity between them and their neighbors. The metric is a scalar value that results from the integration of the solution gradient jump along the boundary of a given cell or *leaf* in case of an already refined cell. So-called leafs are the uppermost or most refined overlays at a given location. The Kelly estimator is calculated by

$$\eta(\Omega_l^i) = \sqrt{\int_{\partial\Omega_l^i} c \cdot \|[\nabla u]\|_2^2 d\partial\Omega}. \quad (5.93)$$

where  $[\![\cdot]\!]$  is the jump operator and  $c$  is a user defined factor for which common choices are

$$c = \frac{h_l}{24} \quad \text{or} \quad c = \frac{h_l}{2 \cdot p_n} \quad (5.94)$$

with  $h_l$  being the length or area of the leaf boundary and  $p_n$  the polynomial degree of the neighboring leaf. Here, the first choice is used in combination with a threshold of  $a \cdot \bar{\eta}$ , meaning all leafs with a Kelly estimator error above this threshold shall be refined. The factor  $a$  is a user-defined factor to scale the mean value of all Kelly estimator errors in the considered domain. In this work, the factor is chosen to be  $a = 0.75$ . For more details on the refinement metric and its implementation, the reader is referred to [Schmäke, 2023].

The perforated plate is stretched to a total displacement of 0.6 mm at the top face applied in 43 load steps. Figure 5.7 shows the reaction force at the top face over the prescribed displacement  $\bar{u}$ . The FCM solutions are compared with a FEM analysis using  $6 \times 10 \times 2$  standard  $p = 2$  elements which seem to be in very accurate agreement. The analyses are further compared to a reference of [de Souza Neto et al., 2011] drawn in brown. This curve appears to be slightly over the curves of this work. This may not originate from the fact that a plane model is compared to a spacial model but rather the type of the finite element. In the reference solution triangles with linear basis were used which tend to be stiffer than quadrilaterals known as *shear locking*. Due to the artificially increased stiffness, the reaction force against the prescribed displacement will overshoot. Within the FCM analyses the adaptive spacetree quadrature is compared with the non-negative moment fitting. The difference between the quadrature techniques appears marginal. However, the moment fitting curves are slightly below the spacetree curves which might stem from the fact that not only the tangent stiffness matrix and the internal force vector are integrated by using the quadrature points, where the error might be negligible. But also the return mapping procedure is performed at the point locations which makes the NNMF efficient due to the low number of points in the first place but

might lead to small differences compared to the AST which evaluates far more points in regions where plastic straining occurs at cut boundaries. During the refinement cycles no difference between the curves can be observed. Together with the load-displacement curves, a second plot shows the global Newton-Raphson iterations that were required to correct the solution back onto the equilibrium path. Here, the FCM seems to converge faster than FEM in general. While the NNMF and AST quadrature show no relevant difference in the number of iterations, the refinements do. The convergence does not slow continuously with increasing refinement cycles, but refined meshes of cycle  $i > 0$  do need more correcting iterations in general. Each of the shown analyses requires more iterations over the load steps which could stem from an increasing plastically strained fraction of the domain.

Below in Table 5.2, the increase of efficiency is outlined in terms of the number of quadrature points and computation runtime. Overall refinement cycles the non-negative moment fitting can reduce the number of quadrature points in the range of around 75% - 88% which leads to a reduction in runtime of around 30%. The mesh of the refinement cycles  $i = 2$  and  $i = 3$  is very similar indicated by the similar number of quadrature points and the fact that the curves in Figure 5.7 entirely match each other. Hence, the mesh seems to be converged to a reasonable degree of refinement.

Figure 5.8 shows the distribution of the refinement level, displacement magnitude and the accumulated plastic strain on the domain. Here, cycle  $i = 3$  is not shown due to its similarity to  $i = 2$ . The refinement metric can locate the relevant region of the domain where the gradients in the displacement and plastic strain are high. By visual assessment, the refinement manages to improve the smoothness of the accumulated plastic strain field and produces a clear band of the plastically deformed region.

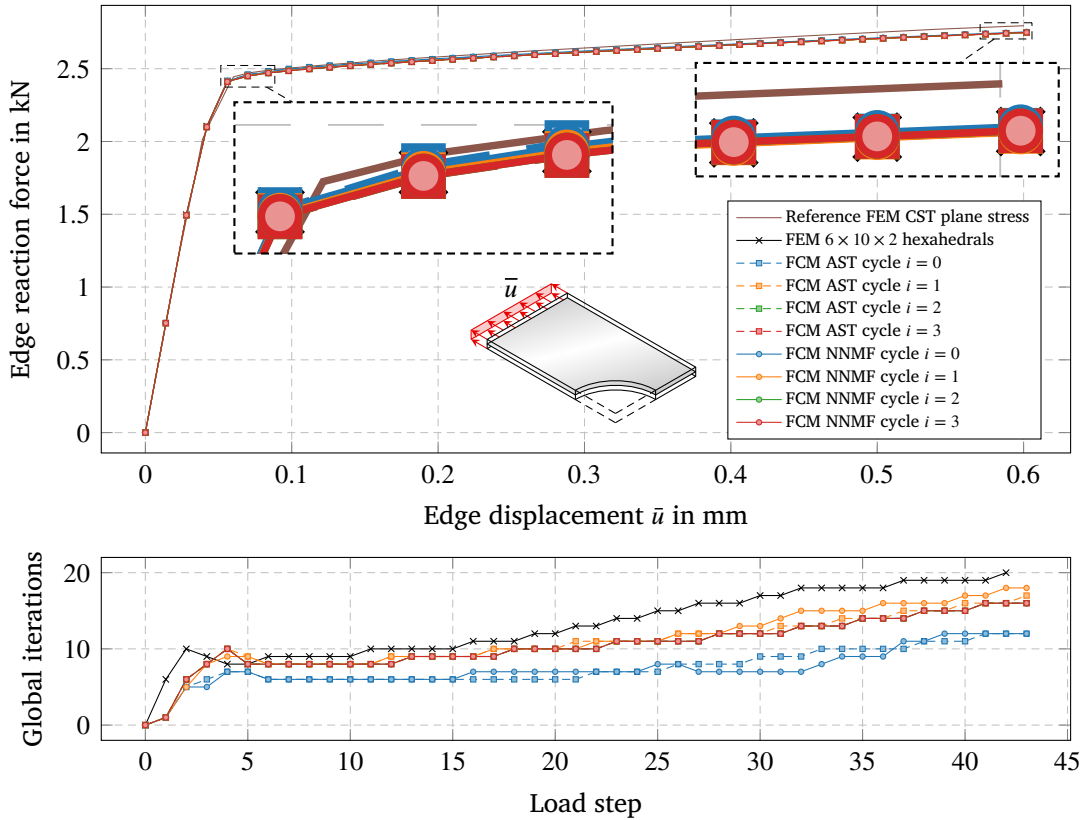


**Figure 5.7** Results of the elastoplastic analysis of the perforated plate using a  $5 \times 9 \times 2$  cell grid with  $p = 2$  basis which is refined in three cycles. The reference in the force-displacement graph is taken from [de Souza Neto et al., 2011].

Cycle	Total			Physical domain		Fictitious domain	
	AST	NNMF	Reduction	AST	NNMF	AST	NNMF
$i = 0$	20 412	2 468	87.91%	20 142	2 198	270	270
$i = 1$	38 031	6 039	84.12%	36 477	4 485	1 554	1 554
$i = 2$	58 544	14 389	75.42%	54 432	10 051	4 112	4 338
$i = 3$	58 936	14 781	74.92%	54 432	10 051	4 504	4 730

(a) Number of quadrature points.

Normalized computational effort := Runtime / Runtime with AST at  $i = 0$

Cycle	Total			Quadrature setup		Solving procedure	
	AST	NNMF	Reduction	AST	NNMF	AST	NNMF
$i = 0$	1.00	0.68	31.94%	1.00	3.27	1.00	0.68
$i = 1$	3.10	2.16	30.17%	1.95	8.03	3.10	2.16
$i = 2$	4.35	2.95	32.05%	1.93	37.74	4.35	2.94
$i = 3$	4.51	3.20	29.10%	1.79	35.23	4.51	3.19

(b) Normalized computational effort.

**Table 5.2** Efficiency of the non-negative moment fitting quadrature (NNMF) compared with the adaptive spacetree decomposition (AST) for an elastoplastic analysis of the perforated plate with refinement cycles  $i = 0, \dots, 3$ .

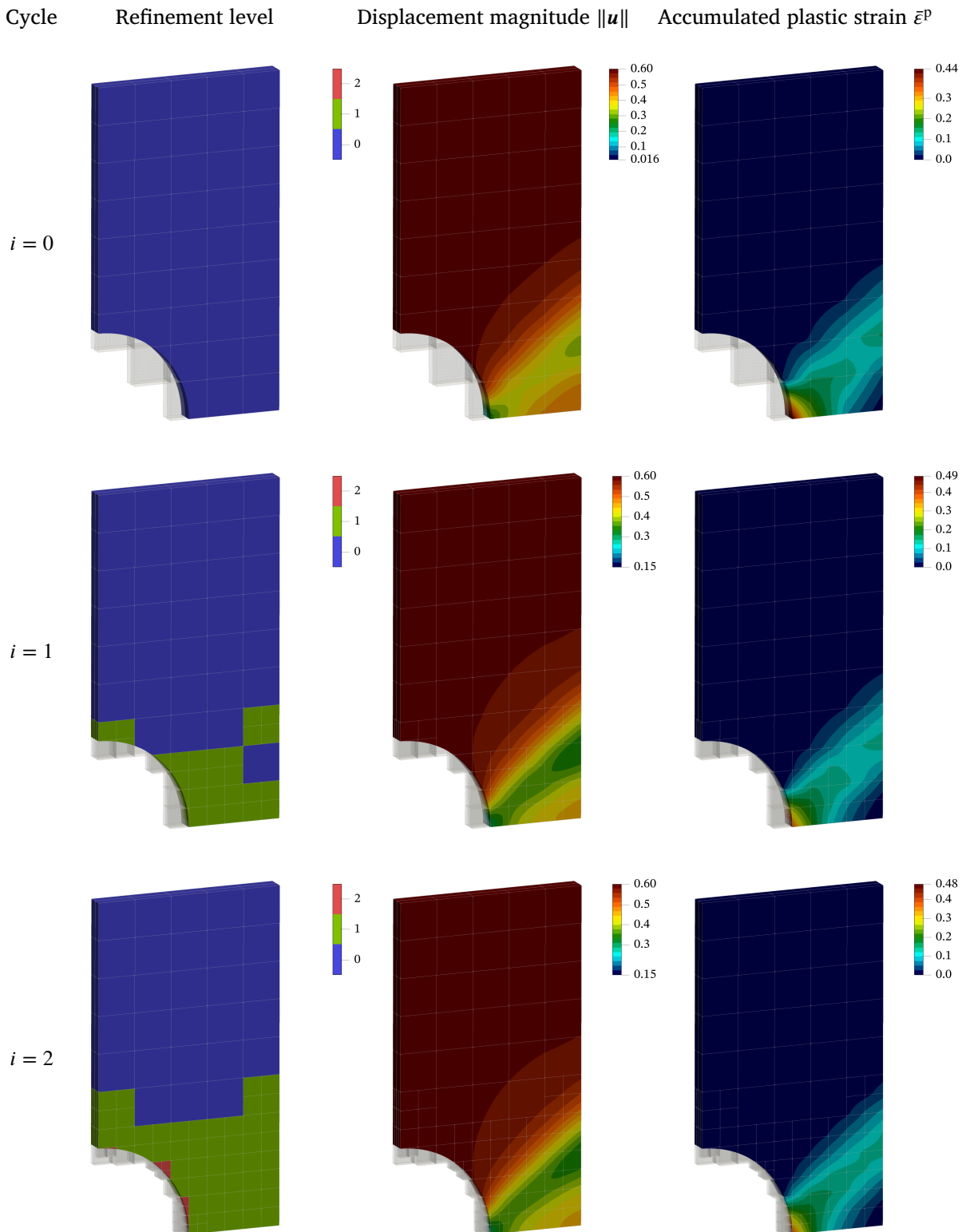


**Figure 5.8** Distribution of the refinement level, the displacement magnitude  $\|u\|$  and the accumulated plastic strain  $\bar{\varepsilon}^p$  over the domain of the perforated plate under elastoplastic tension for the refinement cycles  $i = 0, 1, 2$ . The results of the third cycle are not shown since they are fairly identical to  $i = 2$ .

# Chapter 6

## Thermo-viscoplasticity

So far, the elastoplastic material was assumed to behave independently of the deformation velocity, which is why it is also termed *rate-independent plasticity*. In this chapter, the material is considered to be *rate-dependent* as real materials are generally time-dependent, such that their stress response depends on the rate of loading. In continuum mechanics, the rate dependence is known as *viscosity* which describes the material's resistance at a given deformation rate or simply the resistance to flow in a context of fluids. That is why *rate-dependent plasticity* is interchangeably used with *viscoplasticity*.

In a second step, another independence of the previous material model is taken into account. Especially in the context of metals, the material properties change with temperature. While thermal effects are neglected for solid metals with fairly uniform temperature, they are essential in analyses where thermal boundary conditions are heavily involved besides the structural mechanics. By combining the thermoelastic coupling of Chapter 4 with viscoplastic material, a *thermo-viscoplastic* model for the analysis of complex engineering problems is achieved.

### 6.1 Mathematical theory of viscoplasticity

Considering the specimen under uniaxial tensile load in Figure 6.1 shall demonstrate the basic phenomenological aspects of viscoplasticity. Especially for metals at higher temperatures beyond around one-third of their melting point, the rate dependence can be observed with significant effects on the stress response. This knowledge on the behavior of the metal is of great importance, for instance, in metal-forging operations like hot forging to design the process properly. On the right, the influence on the stress-strain curve is shown for three different strain rates  $\dot{\epsilon}_1$ ,  $\dot{\epsilon}_2$  and  $\dot{\epsilon}_3$  characterized by the slope of the applied strain over time which will be considered as constant throughout this work. The applied strains  $\epsilon$  over time  $t$  are depicted on the left side. The slope of

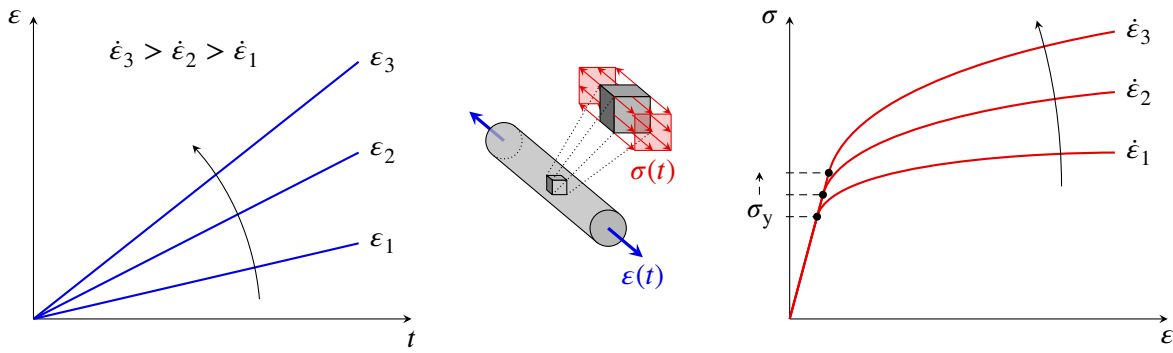


**Figure 6.1** Schematic stress response of an uniaxial tensile specimen for different applied strain rates  $\dot{\epsilon}_i$ . On the left axis, the applied strain is shown over time while the right axis depicts the stress response over the applied strain.

the linear elastic domain is largely independent of the strain rate while the yield stress and the hardening curve strongly depend on the rate of straining.

For the most part, rate-dependent plasticity can be recovered from the rate-independent theory of plasticity. Therefore, the following viscoplastic model is based on the work of [de Souza Neto et al., 2011] and continues to use the von Mises yield criterion with the yield function

$$\Phi(\sigma, A) = \sqrt{3 \cdot J_2(\mathbf{s}(\sigma))} - \sigma_y(\bar{\epsilon}^p), \quad \sigma = \mathbf{C}^e : \boldsymbol{\epsilon}^e \quad (6.1)$$

and an isotropic strain hardening rule of the form

$$\sigma_y(\bar{\epsilon}^p) := \sigma_{y_0} + \chi(\bar{\epsilon}^p), \quad \chi(\bar{\epsilon}^p) = \begin{cases} 0 & \text{perfect plasticity} \\ H \cdot \bar{\epsilon}^p & \text{linear hardening} \\ H(\bar{\epsilon}^p) & \text{nonlinear hardening} \end{cases}. \quad (6.2)$$

The entrance of introducing irreversible deformation to the material model remains in the decomposition of the strains

$$\boldsymbol{\epsilon} = \boldsymbol{\epsilon}^e + \boldsymbol{\epsilon}^p \quad (6.3)$$

leading to a split of the specific Helmholtz free energy in the same manner

$$\Psi(\boldsymbol{\epsilon}^e, \alpha) = \Psi^e(\boldsymbol{\epsilon}^e) + \Psi^p(\alpha) \quad (6.4)$$

from which the elastic part in the form of the elastic strain energy yields the elastic constitutive law

$$\sigma = \frac{\partial \Psi^e}{\partial \boldsymbol{\epsilon}^e} = \mathbf{C}^e : \boldsymbol{\epsilon}^e \quad (6.5)$$

and the plastic part still depends on the internal hardening variable

$$\alpha = \{\bar{\epsilon}^p\}, \quad \bar{\epsilon}^p = \int_0^t \sqrt{\frac{2}{3}} \cdot \|\dot{\epsilon}^p\| dt \quad (6.6)$$

leading to the hardening thermodynamic force

$$A := \rho \cdot \frac{\partial \Psi^p}{\partial \alpha} = \{x(\bar{\epsilon}^p)\}. \quad (6.7)$$

### 6.1.1 Viscoplastic flow rule and hardening law

Despite the analogous formulation to the rate-independent counterpart, the viscoplastic model differs in its formulation of the evolution laws. Up to this point, the concept of time throughout this work was considered as a *pseudo-time*. Thus, the plastic strain rate  $\dot{\epsilon}^p$  is in fact a derivative of  $\epsilon^p$  with respect to a *pseudo-time* parameter which merely indicates a time stepping in the sequence of events and the actual timescale is irrelevant. However, for rate-dependent materials,  $\dot{\epsilon}^p$  is the actual derivative with respect to time. Additionally, in order to capture viscous phenomena, the plastic multiplier  $\dot{\gamma}$  is postulated as an explicit function of the stress tensor  $\sigma$  and hardening thermodynamic forces  $A$

$$\dot{\epsilon}^p(\sigma, A) = \dot{\gamma}(\sigma, A) \cdot N(\sigma, A) \quad (6.8a)$$

$$\dot{\alpha}(\sigma, A) = \dot{\gamma}(\sigma, A) \cdot H(\sigma, A) \quad (6.8b)$$

while maintaining the same format as in the rate-independent case. The explicit function  $\dot{\gamma}(\sigma, A)$  is a constitutive relation that should represent how the rate of plastic straining varies with the level of stress. Two very similar models shall be introduced which are widely used in the computational analysis of viscoplasticity. The first and older version is from [Perzyna, 1971] and suggests the power law

$$\dot{\gamma}(\sigma, A) = \begin{cases} \frac{1}{\mu} \cdot \left[ \frac{\sigma_v(\sigma)}{\sigma_y(A)} - 1 \right]^{\frac{1}{m}} & \text{if } \Phi(\sigma, A) \geq 0 \\ 0 & \text{if } \Phi(\sigma, A) < 0 \end{cases} \quad (6.9)$$

where  $\mu > 0$  is the *relaxation time* in seconds representing the viscosity,  $m > 0$  is the non-dimensional *viscoplastic exponent* representing the rate sensitivity. The second, adapted version of [Perić, 1993] uses the same material constants and a similar power

law approach

$$\dot{\gamma}(\sigma, A) = \begin{cases} \frac{1}{\mu} \cdot \left[ \left[ \frac{\sigma_v(\sigma)}{\sigma_y(A)} \right]^{\frac{1}{m}} - 1 \right] & \text{if } \Phi(\sigma, A) \geq 0 \\ 0 & \text{if } \Phi(\sigma, A) < 0. \end{cases} \quad (6.10)$$

### 6.1.2 Summary of the viscoplastic model

Table 6.1 summarizes the viscoplastic von Mises model with isotropic strain hardening.

Strain decomposition	$\epsilon = \epsilon^e + \epsilon^p$
Specific free energy	$\psi = \psi^e(\epsilon^e) + \psi^p(\alpha)$
Elastic constitutive law	$\sigma = C^e : \epsilon^e = 2 \cdot G \cdot \epsilon_d^e + K \cdot \epsilon_v^e \cdot I$
Yield function	$\Phi = \sqrt{3 \cdot J_2(s(\sigma))} - \sigma_y(\bar{\epsilon}^p)$
Internal variables	$\alpha = \{\bar{\epsilon}^p\}, \quad \bar{\epsilon}^p = \int_0^t \sqrt{\frac{2}{3}} \cdot \ \dot{\epsilon}^p\  dt$
Hardening constitutive law	$A = \{\kappa(\bar{\epsilon}^p)\}$
Hardening curve	$\sigma_y = \sigma_{y_0} + \kappa(\bar{\epsilon}^p)$
Viscoplastic constitutive	$\dot{\gamma}(\sigma, A) \quad \text{e.g. (6.9) or (6.10)}$
Viscoplastic flow rule	$\dot{\epsilon}^p = \dot{\gamma}(\sigma, A) \cdot N = \dot{\gamma}(\sigma, A) \cdot \sqrt{\frac{3}{2}} \cdot \frac{s(\sigma)}{\ s(\sigma)\ }$
Hardening law	$\dot{\epsilon}^p = \dot{\gamma}(\sigma, A) \cdot H = \dot{\gamma}(\sigma, A)$

**Table 6.1** Tabular summary of the associative von Mises viscoplasticity model with isotropic strain hardening.

### 6.1.3 Euler discretization of the viscoplastic initial value problem

A material point at  $x$  of a body with domain  $\Omega$  shall be considered following the constitutive behavior stated in the equations (6.8a) and (6.8b). Given the initial values of  $\epsilon^e(t_0)$  and of  $\alpha(t_0)$  as well as the history of the strain tensor  $\epsilon(t)$ ,  $t \in [t_0, \hat{t}]$ , the functions of the elastic strain tensor  $\epsilon^e(t)$  and the internal variables  $\alpha(t)$  shall be found which satisfy the viscoplastic constitutive equations

$$\dot{\epsilon}^e(t) = \dot{\epsilon}(t) - \dot{\gamma}(\sigma(t), A(t)) \cdot N(\sigma(t), A(t)) \quad (6.11a)$$

$$\dot{\alpha}(t) = \dot{\gamma}(\sigma(t), A(t)) \cdot H(\sigma(t), A(t)) \quad (6.11b)$$

for each time instant  $t \in [t_0, \hat{t}]$ , with

$$\boldsymbol{\sigma}(t) = \rho \cdot \frac{\partial \psi}{\partial \boldsymbol{\epsilon}^e} \Big|_t, \quad \mathbf{A}(t) = \rho \cdot \frac{\partial \psi}{\partial \boldsymbol{\alpha}} \Big|_t. \quad (6.12)$$

In contrast to the rate-independent case, the viscoplastic multiplier is no longer an unknown of the constitutive equations since it is now formulated as an explicit. By employing a standard *implicit Euler time discretization*, the initial value problem (6.11) can be formulated within a time interval  $[t_n, t_{n+1}]$  with a time increment of  $\Delta t = t_{n+1} - t_n$  where the continuous functions  $(\bullet)(t)$  are rewritten in the incremental format

$$(\bullet)_{n+1} = (\bullet)_n + \Delta(\bullet). \quad (6.13)$$

Thus now, given the elastic strain tensor  $\boldsymbol{\epsilon}_n^e$  and internal variables  $\boldsymbol{\alpha}_n$  at the beginning of the time step  $[t_n, t_{n+1}]$ , and given the strain increment  $\Delta\boldsymbol{\epsilon}$  for this interval, the system of algebraic equations

$$\boldsymbol{\epsilon}_{n+1}^e = \boldsymbol{\epsilon}_n^e + \Delta\boldsymbol{\epsilon} - \Delta\gamma \cdot \mathbf{N}(\boldsymbol{\sigma}_{n+1}, \mathbf{A}_{n+1}) \quad (6.14a)$$

$$\boldsymbol{\alpha}_{n+1} = \boldsymbol{\alpha}_n + \Delta\gamma \cdot \mathbf{H}(\boldsymbol{\sigma}_{n+1}, \mathbf{A}_{n+1}) \quad (6.14b)$$

with the incremental viscoplastic multiplier given in terms of the explicit constitutive function for  $\dot{\gamma}$  and the time increment  $\Delta t$  by

$$\Delta\gamma = \Delta\gamma(\boldsymbol{\sigma}_{n+1}, \mathbf{A}_{n+1}) = \Delta t \cdot \dot{\gamma}(\boldsymbol{\sigma}_{n+1}, \mathbf{A}_{n+1}) \quad (6.15)$$

and the constitutive relations of the stress and hardening thermodynamic forces

$$\boldsymbol{\sigma}_{n+1} = \rho \cdot \frac{\partial \psi}{\partial \boldsymbol{\epsilon}^e} \Big|_{n+1}, \quad \mathbf{A}_{n+1} = \rho \cdot \frac{\partial \psi}{\partial \boldsymbol{\alpha}} \Big|_{n+1}. \quad (6.16)$$

shall be solved for the unknowns  $\boldsymbol{\epsilon}_{n+1}$  and  $\boldsymbol{\alpha}_{n+1}$ . It shall be noted that for the non-elastic case the updated stress state  $\boldsymbol{\sigma}_{n+1}$  generally does not lie on the yield surface, that is

$$\Phi(\boldsymbol{\sigma}_{n+1}, \mathbf{A}_{n+1}) > 0. \quad (6.17)$$

Thus, in contrast to the rate-independent case, the consistency condition  $\Phi_{n+1} = 0$  is no longer valid for the viscoplastic model.

#### 6.1.4 Elastic predictor viscoplastic return mapping algorithm

Since the viscoplastic multiplier  $\dot{\gamma}(\boldsymbol{\sigma}, \mathbf{A})$  holds the properties

$$\dot{\gamma}(\boldsymbol{\sigma}, \mathbf{A}) \begin{cases} = 0 & \text{if } \Phi(\boldsymbol{\sigma}, \mathbf{A}) \leq 0 \\ \neq 0 & \text{if } \Phi(\boldsymbol{\sigma}, \mathbf{A}) > 0 \end{cases} \quad (6.18)$$

the plastic strain  $\boldsymbol{\epsilon}^p$  and internal hardening variables  $\alpha$  may only evolve if  $\Phi(\sigma_{n+1}, \mathbf{A}_{n+1}) > 0$ . Therefore, it still is reasonable to compute an elastic trial state which may be corrected in a second step. Although the updated stress state will not lie on the yield surface in general, that is  $\Phi_{n+1} \neq 0$ , for material models that are formulated based on the existence of a yield surface, the two-step procedure remains identical to the rate-independent case. The terminology of the *elastic predictor viscoplastic return mapping algorithm* remains justifiable in the sense that the corrective step still returns the trial stress towards the yield surface. Thus, the trial step described in equations (5.76) to (5.80) remains identical while the return mapping equations (5.81) are replaced by (6.14) and (6.15) in order to solve

$$\boldsymbol{\epsilon}_{n+1}^e = \boldsymbol{\epsilon}_{n+1}^{e\text{trial}} - \Delta\gamma \cdot \mathbf{N}(\sigma_{n+1}, \mathbf{A}_{n+1}) \quad (6.19a)$$

$$\alpha_{n+1} = \alpha_{n+1}^{\text{trial}} + \Delta\gamma \cdot \mathbf{H}(\sigma_{n+1}, \mathbf{A}_{n+1}) \quad (6.19b)$$

with the incremental viscoplastic multiplier

$$\Delta\gamma = \Delta t \cdot \dot{\gamma}(\sigma_{n+1}, \mathbf{A}_{n+1}) \quad (6.20)$$

for the elastic strains  $\boldsymbol{\epsilon}_{n+1}^e$  and the internal hardening variables  $\alpha_{n+1}$ . Then naturally, Algorithm 5.2 holds for the viscoplastic model in consideration of the viscoplastic return mapping equations (6.19).

Lastly, the return mapping algorithm shall be given specifically for the viscoplastic von Mises model and isotropic strain hardening. The trial variables shall be considered as given by equations (5.76) to (5.80) and the viscoplastic case  $\Phi_{n+1}^{\text{trial}} \geq 0$  is discussed. For now, the viscoplastic multiplier is assumed in the form proposed by [Perić, 1993]

$$\dot{\gamma}(\sigma, \mathbf{A}) = \frac{1}{\mu} \cdot \left[ \left[ \frac{\sigma_v(\sigma)}{\sigma_y(\mathbf{A})} \right]^{\frac{1}{m}} - 1 \right]. \quad (6.21)$$

By adopting the Prandtl-Reuss flow vector for  $\mathbf{N}$  and the unit generalized hardening modulus for  $\mathbf{H}$ , the return mapping equations regarding the trial state read

$$\boldsymbol{\epsilon}_{n+1}^e = \boldsymbol{\epsilon}_{n+1}^{e\text{trial}} - \Delta\gamma \cdot \sqrt{\frac{3}{2}} \cdot \frac{\mathbf{s}_{n+1}}{\|\mathbf{s}_{n+1}\|} \quad (6.22a)$$

$$\bar{\epsilon}_{n+1}^p = \bar{\epsilon}_{n+1}^{p\text{trial}} + \Delta\gamma \quad (6.22b)$$

with the incremental viscoplastic multiplier

$$\Delta\gamma = \frac{\Delta t}{\mu} \cdot \left[ \left[ \frac{\sigma_v(\sigma)}{\sigma_y(\mathbf{A})} \right]^{\frac{1}{m}} - 1 \right]. \quad (6.23)$$

Using the elastic law and the deviatoric split, (6.22a) yields the stress update and its

deviatoric part

$$\boldsymbol{\sigma}_{n+1} = \mathbf{C}^e : \left[ \boldsymbol{\epsilon}_{n+1}^{e_{\text{trial}}} - \Delta\gamma \cdot \sqrt{\frac{3}{2}} \cdot \frac{\mathbf{s}_{n+1}}{\|\mathbf{s}_{n+1}\|} \right] \quad (6.24a)$$

$$\mathbf{s}_{n+1} = \mathbf{s}^{\text{trial}} - \Delta\gamma \cdot 2 \cdot G \cdot \sqrt{\frac{3}{2}} \cdot \frac{\mathbf{s}_{n+1}}{\|\mathbf{s}_{n+1}\|}. \quad (6.24b)$$

Due to the collinearity between the trial and updated deviatoric stress  $\mathbf{s}_{n+1}^{\text{trial}}$  and  $\mathbf{s}_{n+1}$ , the relation

$$\mathbf{s}_{n+1} = \left[ 1 - \frac{\Delta\gamma \cdot 3 \cdot G}{\sigma_v(\mathbf{s}_{n+1}^{\text{trial}})} \right] \cdot \mathbf{s}_{n+1}^{\text{trial}}, \quad \sigma_v(\mathbf{s}) = \frac{1}{2} \cdot \mathbf{s} : \mathbf{s} \quad (6.25)$$

remains valid, see (5.85). Applying the definition of the von Mises equivalent stress  $\sigma_v$  on both sides provides

$$\sigma_v(\mathbf{s}_{n+1}) = \sigma_v(\mathbf{s}_{n+1}^{\text{trial}}) - 3 \cdot G \cdot \Delta\gamma. \quad (6.26)$$

Finally, a single return mapping equation to solve for  $\Delta\gamma$  can be obtained by substituting (6.26) together with (6.22b) into (6.23)

$$\Delta\gamma = \frac{\Delta t}{\mu} \cdot \left[ \left[ \frac{\sigma_v(\mathbf{s}_{n+1}^{\text{trial}}) - 3 \cdot G \cdot \Delta\gamma}{\sigma_y(\bar{\epsilon}_n^p + \Delta\gamma)} \right]^{\frac{1}{m}} - 1 \right] \quad (6.27)$$

or in an equivalent form

$$[\sigma_v(\mathbf{s}_{n+1}^{\text{trial}}) - 3 \cdot G \cdot \Delta\gamma] \cdot \left[ \frac{\Delta t}{\mu \cdot \Delta\gamma + \Delta t} \right]^m - \sigma_y(\bar{\epsilon}_n^p + \Delta\gamma) = 0 \quad (6.28)$$

where the division by the viscoplastic exponent is avoided in the exponent to prevent numerical instabilities for small values of  $m$ . Analogous to the rate-independent Algorithm 5.2, the elastic predictor viscoplastic return mapping algorithm is outlined in its particular form for the von Mises model with strain hardening and the viscoplastic multiplier of [Perić, 1993] in Algorithm 6.1.

**Algorithm 6.1** Viscoplastic von Mises model with isotropic strain hardening and plastic flow rule according to [Perić, 1993]: Implicit elastic predictor viscoplastic return mapping algorithm with given strain increment  $\Delta\boldsymbol{\epsilon}$ , known state variables  $\boldsymbol{\epsilon}_n^e$ ,  $\alpha_n$  at time instant  $t_n$  and maximum number of return mapping iterations  $k_{\max}$ .

- 
- 1  $\boldsymbol{\epsilon}_{n+1}^{e_{\text{trial}}} = \boldsymbol{\epsilon}_n^e + \Delta\boldsymbol{\epsilon}$
  - 2  $\bar{\epsilon}_{n+1}^{p_{\text{trial}}} = \bar{\epsilon}_n$
  - 3  $p_{n+1}^{\text{trial}} = K \cdot \epsilon_{v n+1}^{e_{\text{trial}}}$
  - 4  $\mathbf{s}_{n+1}^{\text{trial}} = 2 \cdot G \cdot \boldsymbol{\epsilon}_{d n+1}^{e_{\text{trial}}}$

```

5    $\sigma_v^{\text{trial}} = \sqrt{\frac{3}{2} \cdot \|\mathbf{s}_{n+1}^{\text{trial}}\|}$ 
6   if  $\sigma_v^{\text{trial}} - \sigma_y(\bar{\varepsilon}_{n+1}^{\text{p trial}}) \leq 0$ 
7      $(\bullet)_{n+1} = (\bullet)_{n+1}^{\text{trial}}$ 
8   else
9      $k = 0$ 
10     $\Delta\gamma_{(k)} = 0$ 
11     $r_k = [\sigma_v^{\text{trial}} - 3 \cdot G \cdot \Delta\gamma_{(k)}] \cdot \left[ \frac{\Delta t}{\mu \cdot \Delta\gamma_{(k)} + \Delta t} \right]^m - \sigma_y(\bar{\varepsilon}_{n+1}^{\text{p trial}} + \Delta\gamma_{(k)})$ 
12    while  $|r_k| > 0 \wedge k < k_{\max}$ 
13       $H = \frac{d\sigma_y}{d\bar{\varepsilon}^{\text{p}}} \Big|_{\bar{\varepsilon}_n^{\text{p}} + \Delta\gamma_{(k)}}$ 
14       $d = \frac{dr_k}{d\Delta\gamma_{(k)}} = - \left[ 3 \cdot G + m \cdot \mu \cdot \frac{\sigma_v^{\text{trial}} - 3 \cdot G \cdot \Delta\gamma_{(k)}}{\mu \cdot \Delta\gamma_{(k)} + \Delta t} \right] \cdot \left[ \frac{\Delta t}{\mu \cdot \Delta\gamma_{(k)} + \Delta t} \right]^m - H$ 
15       $\Delta\gamma_{(k+1)} = \Delta\gamma_{(k)} - \frac{r_k}{d}$ 
16       $r_{k+1} = [\sigma_v^{\text{trial}} - 3 \cdot G \cdot \Delta\gamma_{(k+1)}] \cdot \left[ \frac{\Delta t}{\mu \cdot \Delta\gamma_{(k+1)} + \Delta t} \right]^m - \sigma_y(\bar{\varepsilon}_{n+1}^{\text{p trial}} + \Delta\gamma_{(k+1)})$ 
17       $k = k + 1$ 
18  endwhile
19  if  $k = k_{\max}$ 
20    error ( No convergence within  $k_{\max}$  iterations. )
21  else
22     $p_{n+1} = p_{n+1}^{\text{trial}}$ 
23     $\mathbf{s}_{n+1} = \left[ 1 - \Delta\gamma \cdot 3 \cdot G / \sigma_v^{\text{trial}} \right] \cdot \mathbf{s}_{n+1}^{\text{trial}}$ 
24     $\boldsymbol{\sigma}_{n+1} = \mathbf{s}_{n+1} + p_{n+1} \cdot \mathbf{I}$ 
25     $\boldsymbol{\varepsilon}_{n+1}^{\text{e}} = \frac{1}{2 \cdot G} \cdot \mathbf{s}_{n+1} + \frac{1}{3} \cdot \boldsymbol{\varepsilon}_{n+1}^{\text{e trial}} \cdot \mathbf{I}$ 
26     $\bar{\varepsilon}_{n+1}^{\text{p}} = \bar{\varepsilon}_n + \Delta\gamma$ 
27  endif
28 endif

```

---

The return mapping equation for the viscoplastic multiplier definition (6.9) following [Perzyna, 1971] is derived identically and reads

$$\sigma_v(\mathbf{s}_{n+1}^{\text{trial}}) - 3 \cdot G \cdot \Delta\gamma - \left[ 1 + \left[ \frac{\mu \cdot \Delta\gamma}{\Delta t} \right]^m \right] \cdot \sigma_y(\bar{\varepsilon}_n^{\text{p}} + \Delta\gamma) = 0. \quad (6.29)$$

### 6.1.5 Viscoplastic consistent tangent operator

The stress update still is an implicit function of the elastic trial strains defined through the return mapping equations. Therefore, the same procedure for deriving the viscoplastic consistent tangent operator holds as in the rate-independent case up to equation (5.91),

that is

$$\boldsymbol{\sigma}_{n+1}(\boldsymbol{\epsilon}_{n+1}^{\text{e trial}}) = \left[ \mathbf{C}^e - \frac{\Delta\gamma \cdot 6 \cdot G^2}{\sigma_v(\mathbf{s}_{n+1}^{\text{trial}})} \cdot \mathbf{I}_d \right] : \boldsymbol{\epsilon}_{n+1}^{\text{e trial}}. \quad (6.30)$$

Taking the derivative of  $\boldsymbol{\sigma}_{n+1}$  with respect to  $\boldsymbol{\epsilon}_{n+1}^{\text{e trial}}$  yields the viscoplastic consistent tangent operator

$$\mathbf{C}^{\text{ep}} := \frac{\partial \boldsymbol{\sigma}_{n+1}}{\partial \boldsymbol{\epsilon}_{n+1}^{\text{e trial}}}. \quad (6.31)$$

However, since the incremental viscoplastic multiplier  $\Delta\gamma$  is now the solution of a different return mapping equation, equation (6.27) is required to be considered in  $\boldsymbol{\sigma}_{n+1}$  during the evaluation of the differential above. The evaluation of the viscoplastic consistent tangent operator is then obtained through the application of tensor differentiation rules with

$$\begin{aligned} \mathbf{C}^{\text{ep}} &= \mathbf{C}^e - \frac{\Delta\gamma \cdot 6 \cdot G^2}{\sigma_v(\mathbf{s}_{n+1}^{\text{trial}})} \cdot \mathbf{I}_d \\ &+ 6 \cdot G^2 \cdot \left[ \frac{\Delta\gamma}{\sigma_v(\mathbf{s}_{n+1}^{\text{trial}})} - \frac{1}{3 \cdot G + \left[ \frac{\Delta t}{\mu \cdot \Delta\gamma + \Delta t} \right]^{-m} \cdot H + \frac{m \cdot \mu \cdot \sigma_v(\mathbf{s}_{n+1}^{\text{trial}})}{\mu \cdot \Delta\gamma + \Delta t}} \right] \cdot \frac{\mathbf{s}_{n+1}^{\text{trial}}}{\|\mathbf{s}_{n+1}^{\text{trial}}\|} \otimes \frac{\mathbf{s}_{n+1}^{\text{trial}}}{\|\mathbf{s}_{n+1}^{\text{trial}}\|}. \end{aligned} \quad (6.32)$$

The rate-independent consistent tangent operator (5.92) can be recovered by inspection in the limits of a vanishing rate sensitivity  $m \rightarrow 0$ , vanishing viscosity  $\mu \rightarrow 0$  or an infinitely slow straining  $\Delta t \rightarrow \infty$ . In a more implementation-friendly formulation, the tangent operator can be rewritten as shown in the rate-independent Algorithm 5.4 where the factor  $b$  is replaced by

$$b = \frac{6 \cdot G^2}{\|\mathbf{s}_{n+1}\|^2} \cdot \left[ \frac{\Delta\gamma}{\sigma_{v,n+1}} - \frac{1}{3 \cdot G + \left[ \frac{\Delta t}{\mu \cdot \Delta\gamma + \Delta t} \right]^{-m} \cdot H + \frac{m \cdot \mu \cdot \sigma_v(\mathbf{s}_{n+1}^{\text{trial}})}{\mu \cdot \Delta\gamma + \Delta t}} \right] \quad (6.33)$$

to obtain the viscoplastic equivalent with a viscoplastic multiplier definition following [Perić, 1993].

For the same model with a viscoplastic multiplier definition according to [Perzyna, 1971], that is (6.9), the consistent tangent operator is derived from the corresponding

return mapping equations (6.29) identically and reads

$$\mathbf{C}^{\text{ep}} = \mathbf{C}^{\text{e}} - \frac{\Delta\gamma \cdot 6 \cdot G^2}{\sigma_v(\mathbf{s}_{n+1}^{\text{trial}})} \cdot \mathbf{I}_d + 6 \cdot G^2 \cdot \left[ \frac{\Delta\gamma}{\sigma_v(\mathbf{s}_{n+1}^{\text{trial}})} - \frac{1}{3 \cdot G + \left[ 1 + \left[ \frac{\mu \cdot \Delta\gamma}{\Delta t} \right]^m \right] \cdot H + \frac{m \cdot \mu}{\Delta t} \cdot \left[ \frac{\mu \cdot \Delta\gamma}{\Delta t} \right]^{m-1} \cdot \sigma_v(\mathbf{s}_{n+1}^{\text{trial}})} \right] \cdot \frac{\mathbf{s}_{n+1}^{\text{trial}}}{\|\mathbf{s}_{n+1}^{\text{trial}}\|} \otimes \frac{\mathbf{s}_{n+1}^{\text{trial}}}{\|\mathbf{s}_{n+1}^{\text{trial}}\|}. \quad (6.34)$$

or equivalently in an algorithmic sense with the factor

$$b = \frac{6 \cdot G^2}{\|\mathbf{s}_{n+1}\|^2} \cdot \left[ \frac{\Delta\gamma}{\sigma_v(\mathbf{s}_{n+1})} - \frac{1}{3 \cdot G + \left[ 1 + \left[ \frac{\mu \cdot \Delta\gamma}{\Delta t} \right]^m \right] \cdot H + \frac{m \cdot \mu}{\Delta t} \cdot \left[ \frac{\mu \cdot \Delta\gamma}{\Delta t} \right]^{m-1} \cdot \sigma_v(\mathbf{s}_{n+1}^{\text{trial}})} \right] \quad (6.35)$$

applied in Algorithm 5.4.

## 6.2 Viscoplastic perforated plate benchmark

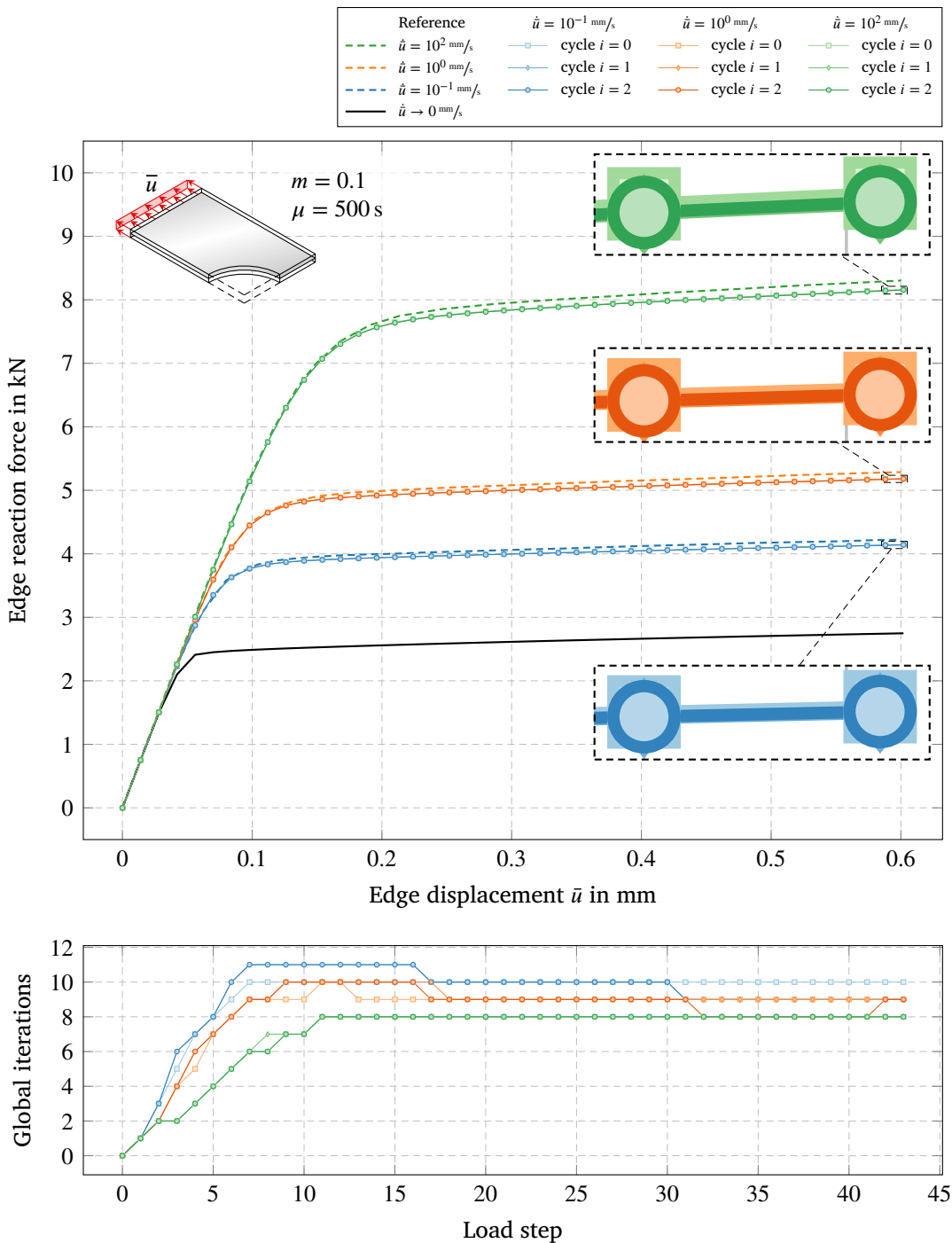
Analogous to the elastoplastic perforated plate benchmark, the same model will be analyzed and compared to the reference solution to verify the concept and implementation. For this purpose, Peric's viscoplastic flow rule is employed to cover the viscous phenomena. While the relaxation time is held constant at  $\mu = 500$  s, the viscoplastic exponent is chosen to be  $m = 0.1$  and  $m = 1.0$  as well as varying deformation rates  $\dot{\nu}$ . The residual material parameters are identical to the elastoplastic model.

Figure 6.2 depicts the load-displacement curves with a viscoplastic exponent of  $m = 0.1$  and deformation rates  $\dot{\nu} = 10^{-2}, 10^0, 10^2$  mm/s along with their corresponding reference curve obtained from [de Souza Neto et al., 2011] and the rate-independent curve in black. For the shown curves only the non-negative moment fitting is used to integrate the cut-cells. The curves immediately show the rate dependence in their elongated elastic region and the magnitude of the edge force. The same offset of the reference curve to the obtained curves from this work can be observed as in the rate-independent case which might have the same origin. If the deformation rate is decreased, the viscoplastic theory recovers the rate-independent case such that the behavior of an infinitely slow deformation  $\dot{\nu} \rightarrow 0$  can be expected. The graph showing the number of global Newton-Raphson iterations suggests that a lower deformation rate which approaches zero worsens the accuracy of the integration of the viscoplastic equations. The rate-independent limit can be reached either by  $\mu \rightarrow 0$  and/or  $\dot{\nu} \rightarrow 0$  for which [de Souza Neto et al., 2011] both demonstrate the largest errors can be expected. This dependence is more clearly observable in Figure 6.3 where a viscoplastic exponent is chosen to be  $m = 1.0$ . While the highest of the three deformation rates  $\dot{\nu} = 10^{-4}, 10^{-3}, 10^{-2}$  mm/s shows a very stable

convergence behavior, the slowest rate which is the nearest to the rate-independent limit requires significantly more equilibrium iterations. Additionally, the load-displacement curves of Figure 6.3 illustrate the effect of the viscoplastic exponent which acts as a rate sensitivity parameter. Even though the rate of deformation is much slower compared to the previous case, the resulting curves show a much more significant change in shape and magnitude. In both cases, the overlay refinements have no significant effect on the load-displacement curves.

Comparing two different deformation rates  $\dot{\nu} = 10^{-3} \text{ mm/s}$  and  $\dot{\nu} = 10^{-2} \text{ mm/s}$ , both with viscoplastic exponent  $m = 1.0$  in Figures 6.4 and 6.5 reveals rate-dependence on the distribution of the deformation. While the slower rate results in a rather narrow band of plastic deformation, the faster rate spreads far more broadly across the domain. In both cases, but especially the latter one, the overlay refinements successfully manage to improve the smoothness of the accumulated plastic strain field in critical regions of high gradients.

Table 6.2 provides insights into the efficiency gain due to the integration via non-negative moment fitting compared to the spacetree quadrature scheme. Overall, the reduction of quadrature points lies between 70% and 88% similar to the perforated plate model in the rate-independent case. The reduction of runtime is similar as well around 30% to 40% for cycles  $i = 0, 1$  but decreases to around 16% at its worst. This may be caused by the overall lower number of global Newton-Raphson iterations of these two analyses compared to the rate-independent case for NNMF, but likewise for the AST. The reduction of computational effort through the usage of a quadrature rule with fewer points involved is particularly dominant if the number of integration procedures during the analysis is high. However, as long as any reduction is achieved, the moment fitting quadrature is to be preferred since no loss in accuracy was exchanged for the efficiency gain so far.



**Figure 6.2** The results of the viscoplastic analysis of the perforated plate with viscoplastic exponent  $m = 0.1$  using a  $5 \times 9 \times 2$  cell grid with  $p = 2$  basis. The initial mesh  $i = 0$  is adaptively refined in three cycles  $i = 1, \dots, 3$  via multi-level  $hp$  overlays. The reference curves are obtained from [de Souza Neto et al., 2011] who use constant strain triangles with plane stress material model.

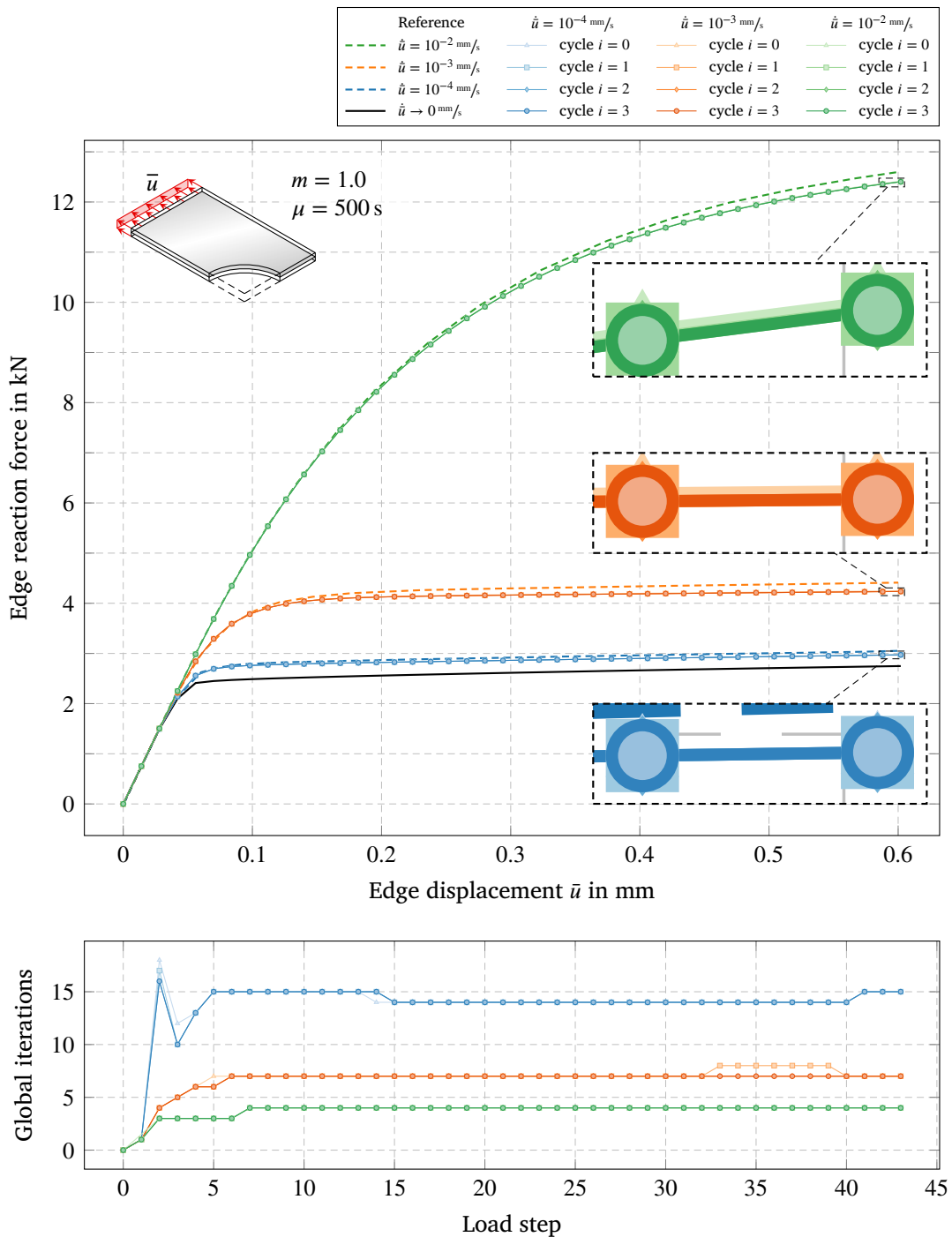


**Figure 6.3** The results of the viscoplastic analysis of the perforated plate using Perić's viscoplastic flow rule with viscoplastic exponent  $m = 1.0$  using a  $5 \times 9 \times 2$  cell grid with  $p = 2$  basis. The initial mesh  $i = 0$  is adaptively refined in three cycles  $i = 1, \dots, 3$  via multi-level  $hp$  overlays. The reference curves are obtained from [de Souza Neto et al., 2011] who use constant strain triangles with plane stress material model.

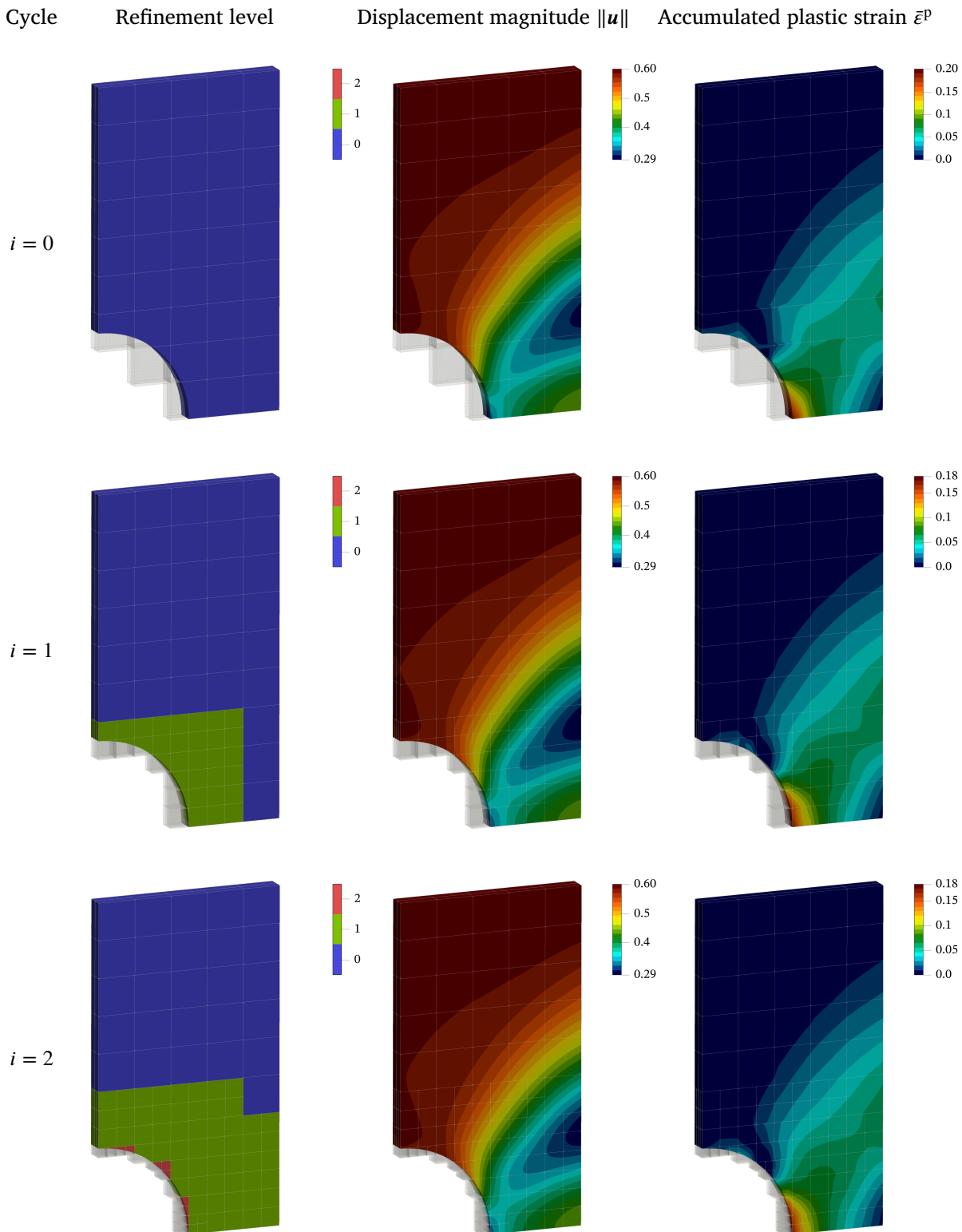


**Figure 6.4** Distribution of the refinement level, the displacement magnitude  $\|u\|$  and the accumulated plastic strain  $\bar{\varepsilon}^p$  over the domain of the perforated plate under viscoplastic tension using Perić's flow rule with exponent  $m = 1.0$  and  $\dot{u} = 10^{-3} \text{ mm/s}$  for the refinement cycles  $i = 0, 1, 2$ . The results of the third cycle are not shown since they are fairly identical to  $i = 2$ .

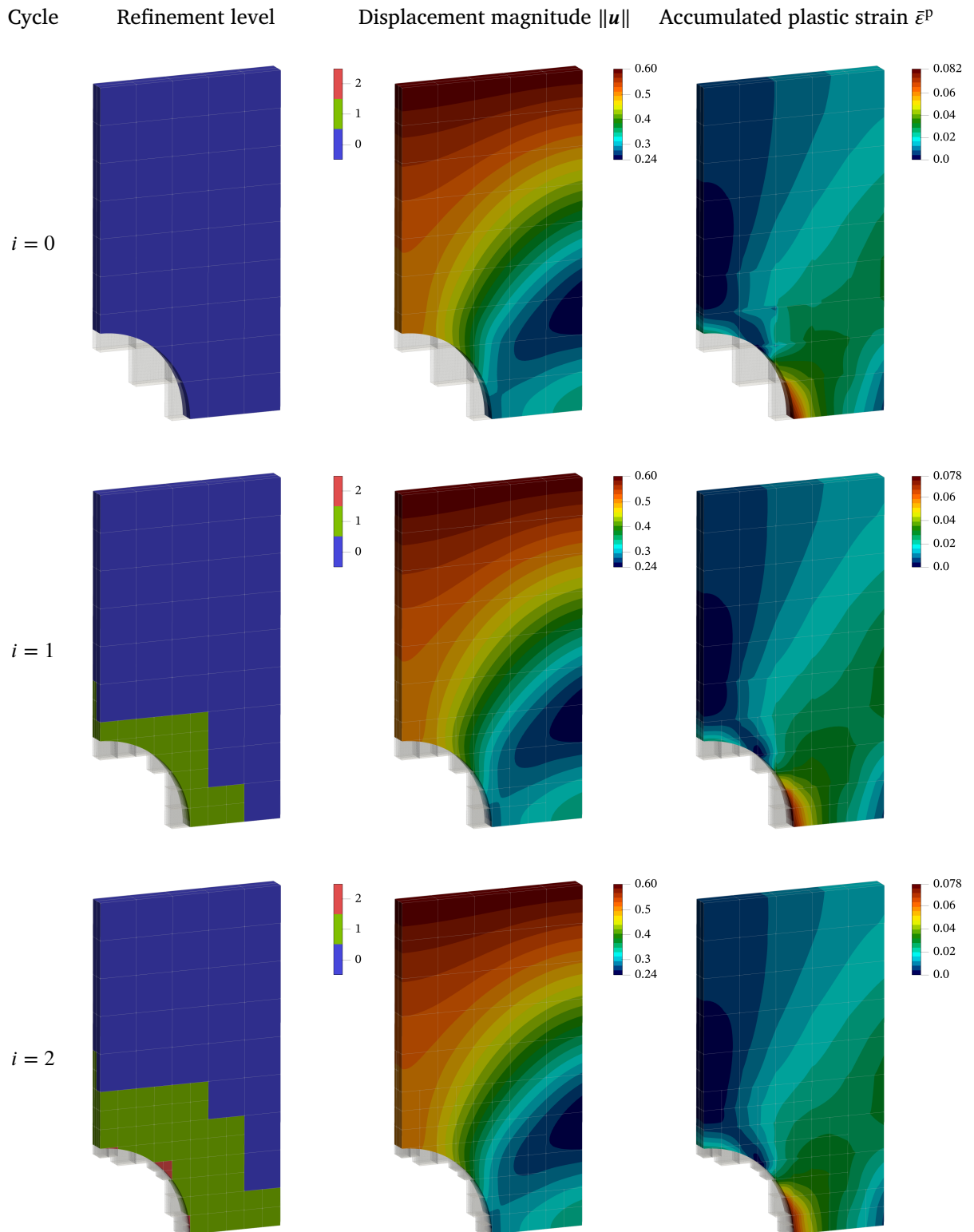


**Figure 6.5** Distribution of the refinement level, the displacement magnitude  $\|u\|$  and the accumulated plastic strain  $\bar{\varepsilon}^p$  over the domain of the perforated plate under viscoplastic tension using Perić's flow rule with exponent  $m = 1.0$  and  $\dot{u} = 10^{-2} \text{ mm/s}$  for the refinement cycles  $i = 0, 1, 2$ . The results of the third cycle are not shown since they are fairly identical to  $i = 2$ .

Cycle	Total			Physical domain		Fictitious domain	
	AST	NNMF	Reduction	AST	NNMF	AST	NNMF
$\dot{u} = 10^{-3} \text{ mm/s}$							
$i = 0$	20 412	2 468	87.91%	20 142	2 198	270	270
$i = 1$	41 730	6 928	83.40%	39 798	4 996	1 932	1 932
$i = 2$	59 300	17 148	71.08%	55 188	12 132	4 112	5 016
$i = 3$	59 741	17 540	70.64%	55 404	12 132	4 337	5 408
$\dot{u} = 10^{-2} \text{ mm/s}$							
$i = 0$	20 412	2 468	87.91%	20 142	2 198	270	270
$i = 1$	41 163	6 367	84.53%	39 231	4 435	1 932	1 932
$i = 2$	53 583	14 819	72.34%	49 923	10 707	3 660	4 112
$i = 3$	54 024	15 267	71.74%	50 139	10 707	3 885	4 560

(a) Number of quadrature points.

Normalized computational effort := Runtime / Runtime with AST at  $i = 0$

Cycle	Total			Quadrature setup		Solving procedure	
	AST	NNMF	Reduction	AST	NNMF	AST	NNMF
$\dot{u} = 10^{-3} \text{ mm/s}$							
$i = 0$	1.00	0.64	36.33%	1.00	4.79	1.00	0.64
$i = 1$	2.36	1.40	40.85%	1.67	12.31	2.36	1.39
$i = 2$	3.09	2.20	28.88%	2.31	42.85	3.09	2.19
$i = 3$	3.03	2.37	21.58%	2.34	39.65	3.03	2.36
$\dot{u} = 10^{-2} \text{ mm/s}$							
$i = 0$	1.00	0.69	31.50%	1.00	3.44	1.00	0.68
$i = 1$	2.25	1.49	33.70%	2.53	9.27	2.25	1.49
$i = 2$	2.79	2.05	26.43%	1.68	37.97	2.79	2.03
$i = 3$	2.91	2.43	16.56%	1.58	30.77	2.91	2.41

(b) Normalized computational effort.

**Table 6.2** Efficiency of the non-negative moment fitting quadrature (NNMF) compared with the adaptive spacetree decomposition (AST) for a viscoplastic analysis of the perforated plate using Perić's viscoplastic flow rule with the viscoplastic exponent  $m = 1.0$  and refinement cycles  $i = 0, \dots, 3$ .

### 6.3 Thermo-viscoplastic coupling

The postulation of the Helmholtz free energy  $\Psi$  in (5.10) as a function of the deformation gradient  $\mathbf{F}$ , the temperature  $T$  and internal variables  $\alpha$  can be assumed to be decomposable like (5.15) but with an additional thermal contribution

$$\Psi(\mathbf{F}, T; \alpha) = \Psi^e(\mathbf{F}) + \Psi^{th}(T) + \Psi^p(\alpha) \quad (6.36)$$

or in the specific format written as

$$\Psi(\boldsymbol{\epsilon}, T; \boldsymbol{\epsilon}^p, \alpha) = \Psi^e(\boldsymbol{\epsilon} - \boldsymbol{\epsilon}^p) + \Psi^{th}(T) + \Psi^p(\alpha). \quad (6.37)$$

Doing so, [Oppermann et al., 2022] have shown that an accurate description of the thermo-viscoplastic phenomena can be established to be handled by the finite element method. Their model handles the thermal strains due to isotropic expansion as well as the heat generation due to viscoplastic yielding. In this work, only the effect of isotropic expansion of the material is considered. However, not only the coupling of the fields is crucial in a mechanical analysis with thermal boundary conditions, but equally the temperature dependence of the material itself. Assumptions made in the following will be focussed on metallic materials.

Pursuing the one-way coupling consideration, the strain tensor can be split into a reversible strain tensor  $\boldsymbol{\epsilon}^r$  in which the elastic strains  $\boldsymbol{\epsilon}^e$  and thermal strains  $\boldsymbol{\epsilon}^{th}$  are lumped together

$$\boldsymbol{\epsilon} = \underbrace{\boldsymbol{\epsilon}^e + \boldsymbol{\epsilon}^{th}}_{\boldsymbol{\epsilon}^r} + \boldsymbol{\epsilon}^p. \quad (6.38)$$

Thereby,  $\boldsymbol{\epsilon}^r$  can be treated just like  $\boldsymbol{\epsilon}^e$  so far. The temperature has no direct contribution to the free energy potential but rather acts through the reversible strains

$$\Psi^e(\boldsymbol{\epsilon} - \boldsymbol{\epsilon}^p) = \Psi^e(\boldsymbol{\epsilon}^r) = \Psi^e(\boldsymbol{\epsilon}^e + \boldsymbol{\epsilon}^{th}) \quad (6.39)$$

to couple the thermal and mechanical solution fields. The definition of thermal strain tensor is adapted to the temperature dependence of the thermal expansion coefficient by

$$\boldsymbol{\epsilon}^{th} = \varepsilon^{th} \cdot \mathbf{I} = \left[ \gamma_m(T) \cdot [T - T_{0^\circ C}] - \gamma_m(T) \cdot [T_0 - T_{0^\circ C}] \right] \cdot \mathbf{I} \quad (6.40)$$

where the scalar  $\varepsilon^{th}$  is the isotropic thermal strain. The coefficient  $\gamma_m$  is the mean thermal expansion coefficient which is usually measured in experiments [Kohlrausch, 1986].

The elastic law remains unchanged with the reversible strains replacing the purely

elastic strains

$$\boldsymbol{\sigma} = 2 \cdot G(T) \cdot \boldsymbol{\epsilon}_d^r + K(T) \cdot \boldsymbol{\epsilon}_v^e \cdot \mathbf{I} \quad (6.41)$$

where the bulk and shear modulus  $G(T)$  and  $K(T)$  are now functions of the temperature. Naturally, the inferred Young's modulus  $E(T)$  and Poisson ratio  $\nu(T)$  are temperature-dependent as well. The temperature  $T_{0^\circ\text{C}} = 273.15\text{ K}$  provides the Celsius scale and  $T_0$  is the initial temperature at the material point in a stress-free state. For metals, all three elastic moduli show a decreasing, generally nonlinear behavior for an increasing temperature.

The von Mises yield function will be employed here as well with a temperature-dependent yield stress

$$\Phi(\boldsymbol{\sigma}, \mathbf{A}) = \sqrt{3 \cdot J_2(\mathbf{s}(\boldsymbol{\sigma}))} - \sigma_y(\bar{\epsilon}^p, T). \quad (6.42)$$

Contrarily to the strain hardening, due to the accumulation of plastic strain  $\bar{\epsilon}^p$ , the rising temperature induces softening to the material. The unstrained, initial yield stress  $\sigma_{y_0}(T)$  as a decreasing, generally nonlinear function of  $T$  is hardened by the evolution of plastic strain. Let  $(\bar{\epsilon}, T)$  be a given state at a material point, then  $\sigma_{y_0}(T)$  will be softened by an exponentially saturating contribution as a function of the scalar hardening thermodynamic force  $\kappa(\bar{\epsilon}^p)$  and the temperature postulated by [Oppermann et al., 2022] in the form

$$\sigma_y(\bar{\epsilon}^p, T) = \sigma_{y_0}(T) - \phi_\kappa(T) \cdot \kappa(\bar{\epsilon}^p) \quad (6.43)$$

where  $\phi_\kappa(T)$  accounts for the softening contribution. The scalar hardening thermodynamical force shall follow a mixed formulation

$$\kappa(\bar{\epsilon}^p) := -\rho \cdot \frac{\partial \Psi}{\partial \bar{\epsilon}^p} = [1 - r^{\text{mix}}] \cdot \Delta\sigma_{y_{\infty 0}} \cdot \left[ \exp\left(-\frac{\bar{\epsilon}^p}{\bar{\epsilon}_0^p}\right) - 1 \right] - r^{\text{mix}} \cdot H_0 \cdot \bar{\epsilon}^p \quad (6.44)$$

where  $r^{\text{mix}} \in [0, 1]$  controls the fraction of linear hardening. For  $r^{\text{mix}} = 0$  the hardening is purely linear with isothermal hardening modulus  $H_0$  while for  $r^{\text{mix}} = 1$ , the hardening is purely exponentially saturating. The saturation is controlled by an isothermal saturation yield stress increment  $\Delta\sigma_{y_{\infty 0}}$  and saturation parameter  $\bar{\epsilon}_0^p$ . The hardening modulus is obtained by the slope of the yield stress as defined above

$$H(\bar{\epsilon}^p) = \frac{\partial \sigma_y}{\partial \bar{\epsilon}^p} = \phi_\kappa(T) \cdot [1 - r^{\text{mix}}] \cdot \frac{\Delta\sigma_{y_{\infty 0}}}{\bar{\epsilon}_0^p} \cdot \left[ \exp\left(-\frac{\bar{\epsilon}^p}{\bar{\epsilon}_0^p}\right) - 1 \right]. \quad (6.45)$$

For the viscoplastic flow rule, the laws of Peric and Perzyna can be utilized with temperature-dependent relaxation time  $\mu(T)$  and viscoplastic exponent  $m(T)$ . For the proposed thermo-viscoplastic model in this work, the Perzyna-type flow rule (6.9) is

Temperatures			Heat flow			Hardening		
$T_{0^\circ\text{C}}$	273.15	K	$\gamma_{m_{01}}$	1.108358	$10^{-5}/\text{K}$	$r^{\text{mix}}$	0.0	[–]
$T_r$	293.15	K	$w_{\gamma_{m1}}$	-4.989882	$10^{-4}/\text{K}$	$H_0$	1.897765	GPa
$T_A^{16\text{MnCr}5}$	1023.15	K	$\gamma_{m_{02}}$	1.232077	$10^{-5}/\text{K}$	$\Delta\sigma_{\infty_0}$	206.3425	MPa
Elasticity			$w_{\gamma_{m2}}$	-6.655428	$10^{-4}/\text{K}$	$\bar{\varepsilon}_0^p$	2.784959	$10^{-2}$
$K_0$	163.1952	GPa	$\kappa_{0_1}$	43.34265	$\text{W}/\text{m}\cdot\text{K}$	$\omega_x$	-39.22882	–
$\omega_K$	8.592410	$10^{-1}$	$w_{\kappa_{11}}$	-5.154848	$10^{-4}/\text{K}$	$\chi_x$	-9.042314	$10^{-3}/\text{K}$
$\chi_K$	4.509029	$10^{-3}/\text{K}$	$w_{\kappa_{21}}$	5.937507	$10^{-3}/\text{K}$	$\varphi_x$	-1.461198	–
$\varphi_K$	-1.338357	–	$w_{\kappa_{31}}$	1.071197	$10^{-3}/\text{K}$	Viscosity		
$G_0$	80.89153	GPa	$w_{\kappa_{41}}$	3.689398	$10^{-4}/\text{K}$	$m$	1.0	–
$\omega_G$	1.265276	[–]	$\kappa_{0_2}$	22.25796	$\text{W}/\text{m}\cdot\text{K}$	$\mu$	0.001 - 1.0	s
$\chi_G$	2.136860	$10^{-3}/\text{K}$	$\omega_{\kappa_2}$	4.963377	$10^{-1}$	Physical		
$\varphi_G$	-1.071127	[–]	$\chi_{\kappa_2}$	-2.782682	$10^{-3}/\text{K}$	$\rho$	7821.8	$\text{kg}/\text{m}^3$

**Table 6.3** Fitting variables of the material parameter interpolation functions  $\phi_{[\bullet]}(\Delta T_r)$  identified by [Oppermann et al., 2022] and material constants used in the thermo-viscoplastic model.

employed.

### 6.3.1 Numerical treatment of temperature-dependent parameters

Following the work of [Oppermann et al., 2022], the material parameter of the case-hardening steel 16MnCr5 (1.1731) [Spittel and Spittel, 2009b] are interpolated from experimental data by three kinds of ansatz functions  $\phi_{[\bullet]}$ . The general scheme of interpolation for a parameter  $[\bullet]$  follows

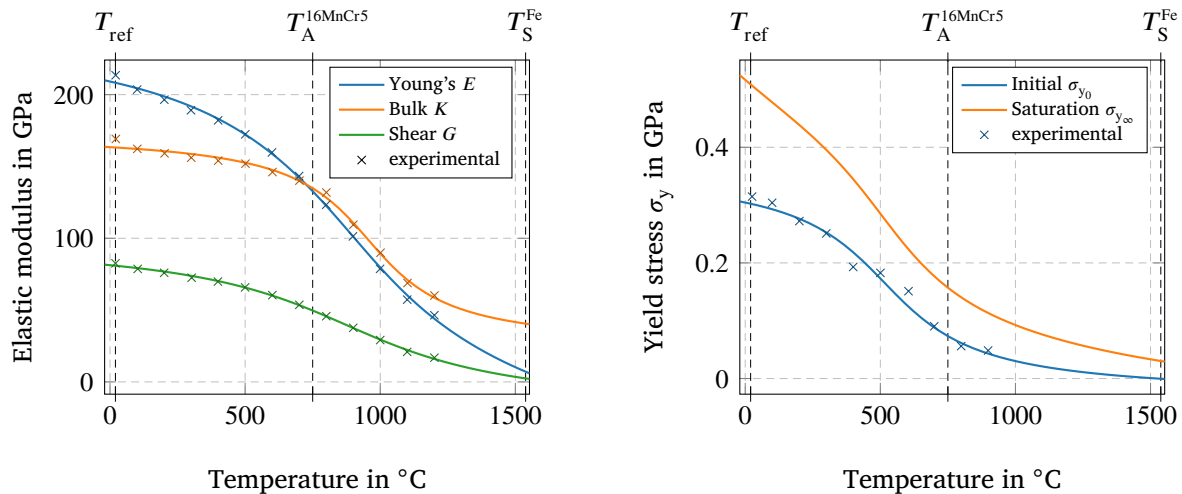
$$[\bullet](T) = [\bullet]_0 \cdot \phi_{[\bullet]}(\Delta T_r) \quad (6.46)$$

where  $\Delta T_r = T - Tr$  describes the difference of the current temperature to a reference temperature which is typically  $20^\circ\text{C} = 293.15\text{ K}$ .  $[\bullet]_0$  is the parameter value at reference temperature. In this work, the viscous parameters  $\mu(T)$  and  $m(T)$  are held constant for the sake of complexity reduction.

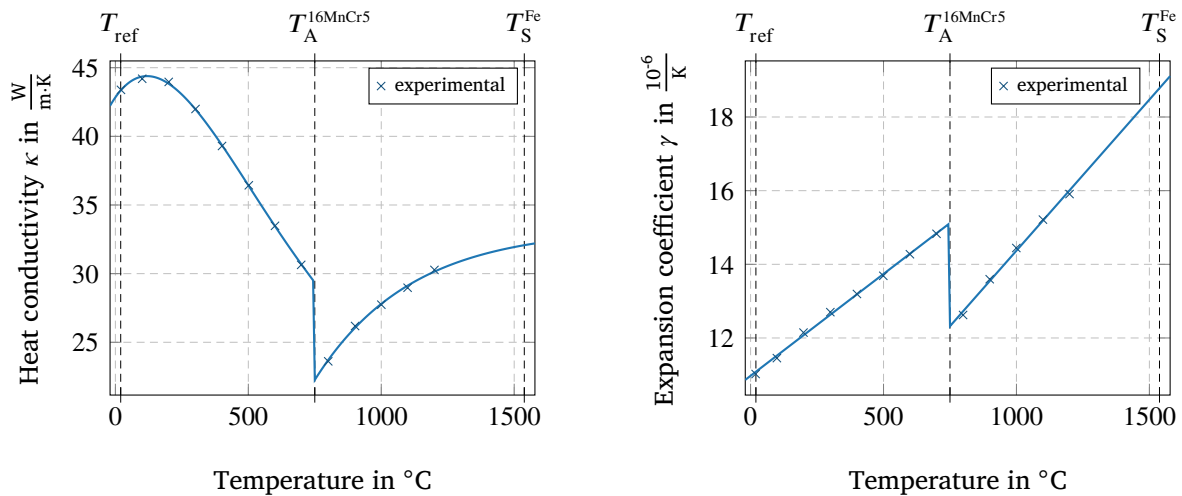
For the interpolation of  $[\bullet](T) = K(T)$ ,  $G(T)$ ,  $\sigma_{y_0}(T)$  and  $\chi(T)$ , an arcus tangens ansatz is used of the form

$$\phi_{[\bullet]}^{\text{atan}}(\Delta T_r) = 1 - \frac{2 \cdot \omega_{[\bullet]}}{\pi - 2 \cdot \varphi_{[\bullet]}} \left[ \arctan \left( \chi_{[\bullet]} \cdot \Delta T_r + \arctan(\varphi_{[\bullet]}) \right) - \varphi_{[\bullet]} \right] \quad (6.47)$$

where  $\omega_{[\bullet]}$ ,  $\varphi_{[\bullet]}$  and  $\chi_{[\bullet]}$  are constant fitting variables. The thermal material parameter  $[\bullet](T) = \gamma_m(T)$  and  $\kappa(T)$  are interpolated piecewise due to the austenitisation property of steel. At  $T_A^{16\text{MnCr}5} = 750^\circ\text{C}$  the crystalline structure of the material changes its cubic lattice from body- to face-centered with increasing temperature. Due to this phenomenon, the thermal expansion coefficient and heat conductivity change rapidly which cannot be



**(a)** Mechanical material parameter with experimental data taken from [Fukuhara and Sanpei, 1993, Spittel and Spittel, 2009a, Liscic et al., 2010].



**(b)** Thermal material parameter with experimental data taken from [Spittel and Spittel, 2009b].

**Figure 6.6** Temperature-dependent material parameters of the case hardening steel 16MnCr5 (1.1731). The continuous curves are obtained by fitting their interpolation function with the parameters of Table 6.3 to the experimental data [Oppermann et al., 2022].  $T_{\text{ref}} = 20^\circ\text{C}$  is the reference temperature,  $T_A^{16\text{MnCr}5} = 750^\circ\text{C}$  is the austenitisation temperature and  $T_S^{\text{Fe}} = 1538^\circ\text{C}$  is the solidus temperature of pure iron.

captured properly by a single ansatz. Defining the piecewise ansatz as

$$[\bullet](T) = \begin{cases} [\bullet]_{0_1} \cdot \phi_{[\bullet]_1}(\Delta T_{r_1}) & \text{if } T \leq T_{r_2} \quad \text{with} \quad \Delta T_{r_1} = T - \Delta T_{r_1} \\ [\bullet]_{0_2} \cdot \phi_{[\bullet]_2}(\Delta T_{r_2}) & \text{if } T > T_{r_2} \quad \text{with} \quad \Delta T_{r_2} = T - \Delta T_{r_2} \end{cases} \quad (6.48)$$

as well as a recursive formula for a polynomial of order  $n$

$$\phi_{[\bullet]}^{p_n}(\Delta T_r) = \left[ 1 - \omega_{[\bullet]_n} \cdot \Delta T_r \cdot \phi_{[\bullet]}^{p_{n-1}} \right] \quad \text{with} \quad n \geq 1 \quad \text{and} \quad \phi_{[\bullet]}^{p_0} = 1 \quad (6.49)$$

and an exponential ansatz

$$\phi_{[\bullet]}^{\exp}(\Delta T_r) = 1 - \omega_{[\bullet]} \cdot [\exp(-\chi_{[\bullet]} \cdot \Delta T_r) - 1] \quad (6.50)$$

the mean thermal expansion coefficient  $\gamma_m(T)$  uses linear polynomials  $\phi_{\gamma_{m1}}^{p_1}$ ,  $\phi_{\gamma_{m2}}^{p_1}$  and the heat conductivity  $\kappa(T)$  is interpolated by a fourth-order polynomial  $\phi_{\kappa_1}^{p_4}$  and an exponential ansatz  $\phi_{\kappa_2}^{\exp}$ . The fitting variables of the material parameter interpolation  $[\bullet](T, p_{[\bullet]})$ , collected in  $p_{[\bullet]}$ , were identified by [Oppermann et al., 2022] through the minimization of the least square problem

$$\min_{p_{[\bullet]}} \sum_{i=1}^{n_{\text{meas}}} \left[ [\bullet](T_i, p_{[\bullet]}) - [\bullet]_{\text{meas}}(T_i) \right]^2 \quad (6.51)$$

where  $[\bullet]_{\text{meas}}(T_i)$  are experimental measurements. The solution to the minimization problem is listed in Table 6.3. The interpolation of the temperature-dependent material parameters is shown in Figure 6.6 where the temperature range is chosen between the reference temperature and the solidus temperature for pure iron implying a valid range for the proposed model.

### 6.3.2 Thermo-viscoplastic perforated plate benchmark

The proposed thermo-viscoplastic model is first applied on the well-known perforated plate. At three different uniformly applied temperature offsets  $\Delta \bar{T} = 0.0^\circ \text{C}$ ,  $400.0^\circ \text{C}$  and  $600.0^\circ \text{C}$  and three different strain rates  $\dot{\varepsilon} = 10^{-1} \text{ mm/s}$ ,  $10^0 \text{ mm/s}$  and  $10^1 \text{ mm/s}$  the model is analyzed the same way as in the temperature-independent cases shown before. Figure 6.7 shows the corresponding force-displacement curves where the effect of the different temperatures is visible in the shape and magnitude of the curves. Due to the chosen exponentially saturating hardening law, the reaction force reaches a maximum where the yield stress is fully saturated and further deformation results in a softening of the material. The viscous parameters are hold constant at  $m = 1.0$  and  $\mu = 0.001 \text{ s}$ .

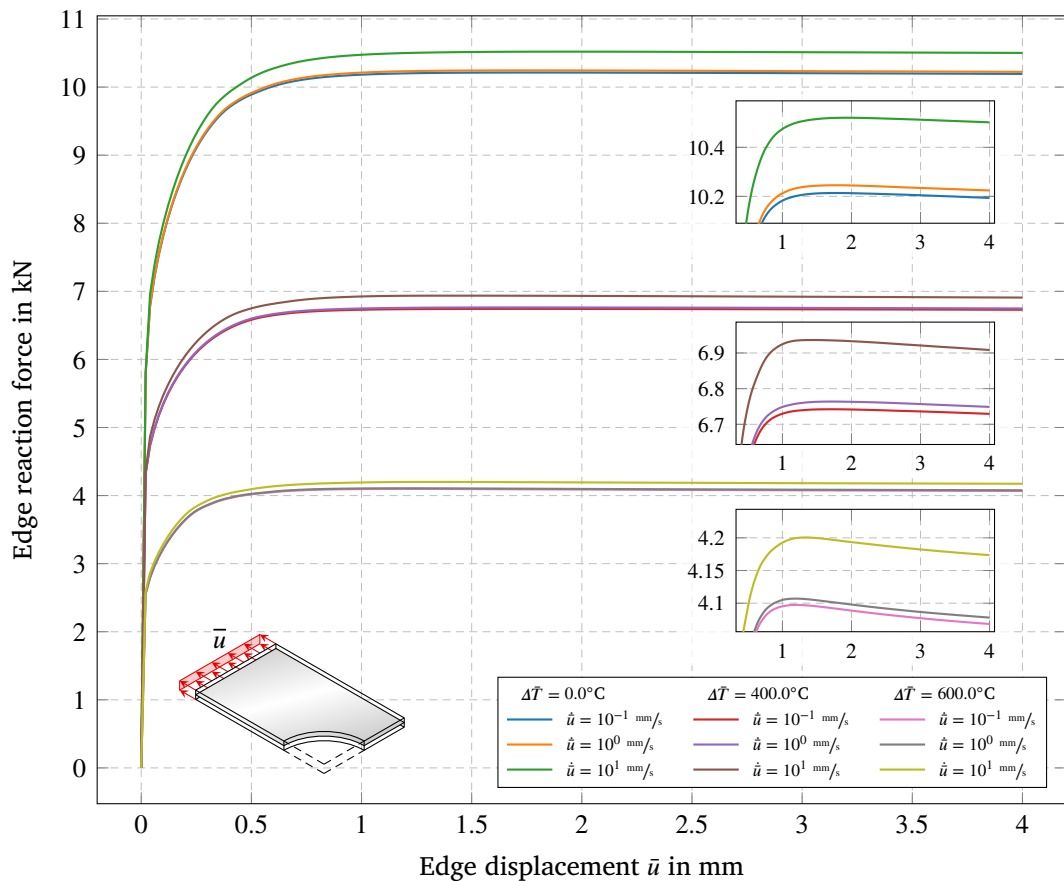


**Figure 6.7** The results of the thermo-viscoplastic analysis of the perforated plate with viscoplastic exponent  $m = 1.0$  and  $\mu = 0.001\text{s}$  using a  $5 \times 9 \times 2$  cell grid with  $p = 2$  basis. The different temperature offsets  $\Delta\bar{T}$  are uniformly applied across the domain.

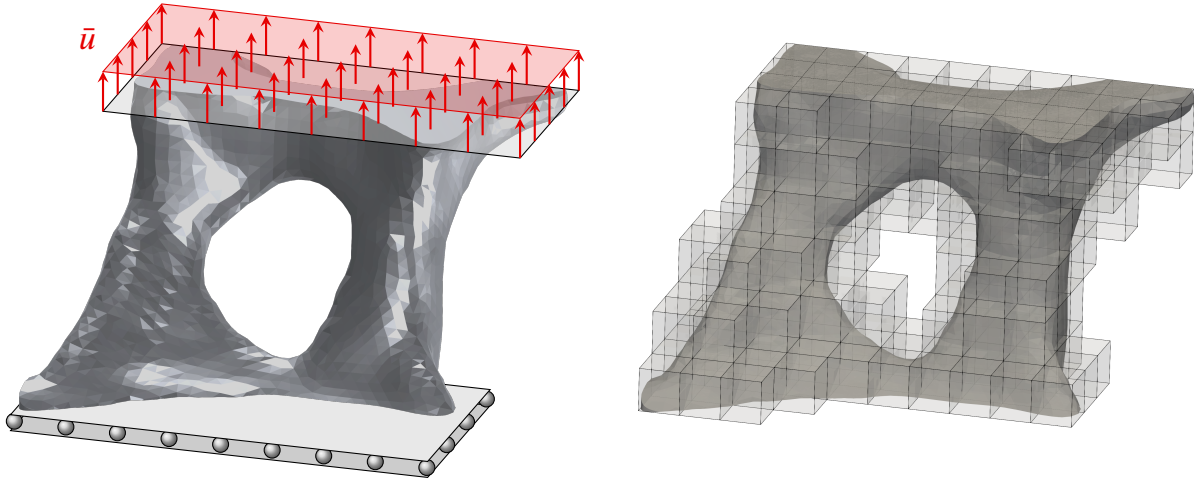


**Figure 6.8** The boundary conditions of the metallic foam pore on the left and the finite cell mesh on the right. The mesh initially consists of  $6 \times 11 \times 8$  cells with  $p = 2$  basis.

## 6.4 Analysis of a metal foam pore

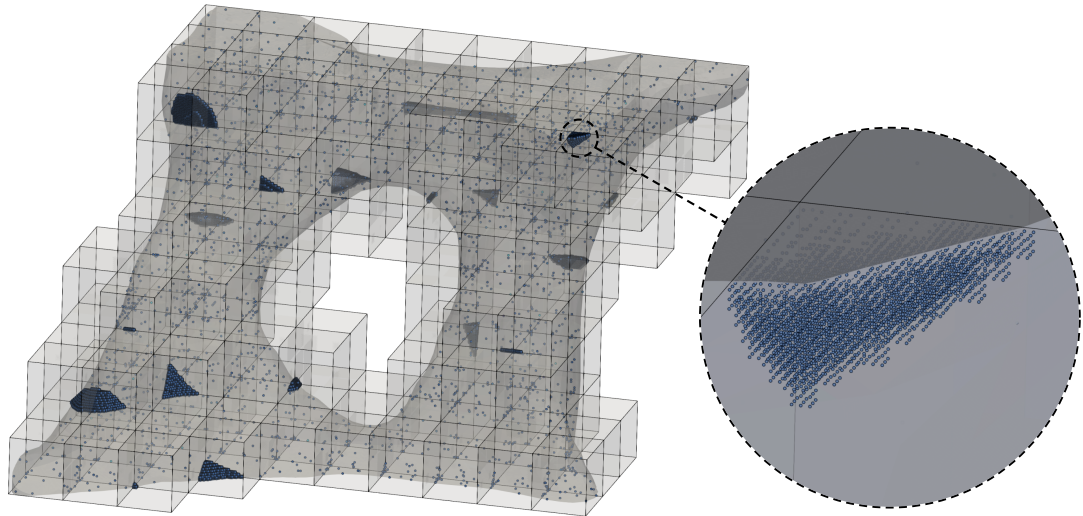
To demonstrate the proposed thermo-viscoplasticity model in combination with the non-negative moment fitting quadrature on a real world example, a small portion of a porous metal foam with a height of 1.4 mm is extracted from a computer tomographic scan based on voxel data. This voxel data is composed of thin slices of the geometry where each slice represents a pixel matrix, just like an actual image, with a gray-scale value indicating the density of the scanned point in space. Thereby, the indicator function can be represented by a straightforward inside/outside check where the density value of the voxel is evaluated at the coordinate of interest to decide whether the point is located in the physical or fictitious domain. This way even objects consisting of various materials having different densities can be incorporated. In Figure 6.8 the foam pore is depicted by an STL surface geometry which represents the boundary between material and void voxels as a surface consisting of triangles. The bottom face is constrained in its normal direction while the top face is prescribed with a total displacement of  $\bar{u} = 4 \mu\text{m}$  which is applied in 8 subsequent load steps. On the right-hand side, the mesh of initially  $6 \times 11 \times 8$  cells with shape function order  $p = 2$  is shown. The same 16MnCr5 Material is used as before with a relaxation time of  $\mu = 1.0 \text{ s}$  and viscoplastic exponent  $m = 1.0$ .

Figure 6.9 depicts the quadrature points used to integrate the foam pore domain. The illustrated magnification into a cluster of quadrature points shows a cell that is cut under bad conditions, namely the physical contribution in the cell is very small compared to the total volume of the cell. In this case, the moment fitting equations become ill-conditioned and in some cases unsolvable for the non-negative least square solver, which means no positive weights could be found for the given point locations. In the implementation of the moment fitting procedure, the number of potential points is

enlarged up to a user-defined number of times by increasing the factor  $L$  if the solver fails. However, even then some cells cannot be tackled and therefore the standard AST points are taken with the initial tree depth of  $k_{\text{AST}}$ . As introduced in [Düster et al., 2008, Hubrich and Düster, 2019], the physical volume fraction could be determined beforehand and badly cut cells could be refined and treated with a separate adaptive algorithm, which is not done in this work. But still, the non-negative moment fitting reduces the number of quadrature points from 8 860 050 initial points obtained from the adaptive spacetree quadrature down to 131 715 points in the physical domain which corresponds to a decrease of 98.51%.

The force-displacement curves of the analysis are depicted in Figure 6.10 for a uniform temperature offset of  $\Delta \bar{T} = 0^{\circ}\text{C}$  and  $\Delta \bar{T} = 80^{\circ}\text{C}$ . As expected, the higher temperature softens the material and leads to a lower edge reaction force for the prescribed displacement while the higher deformation rate produces a higher edge reaction force.

Lastly, the displacement magnitude and accumulated plastic strain distributions are depicted in Figure 6.11. Here, the higher deformation rate again clearly broadens the region of deformation. Due to the slanted orientation of the vertical arms of the pore, the plastic region spreads out diagonally from the constrained bottom to the loaded top face.



**Figure 6.9** Non-negative moment fitting quadrature points used in the foam pore. The NNMF reduces the number of AST quadrature points in the physical domain from 8 860 050 to 131 715. The magnification illustrates a badly cut cell that is equipped with standard AST points due to ill-conditioned/unsolvable moment fitting equations.

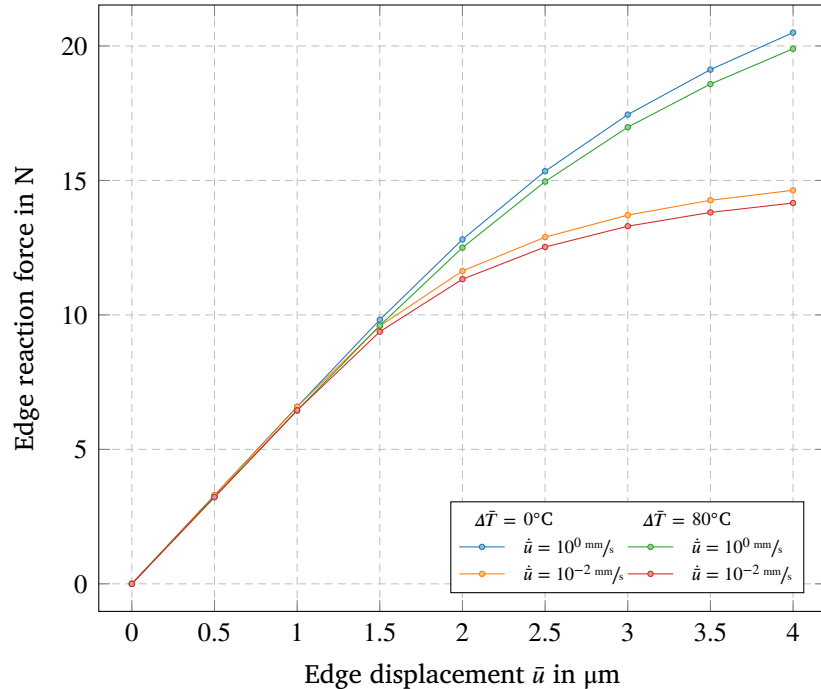


**Figure 6.10** Load-displacement curves of the foam pore for different temperatures and deformation rates.

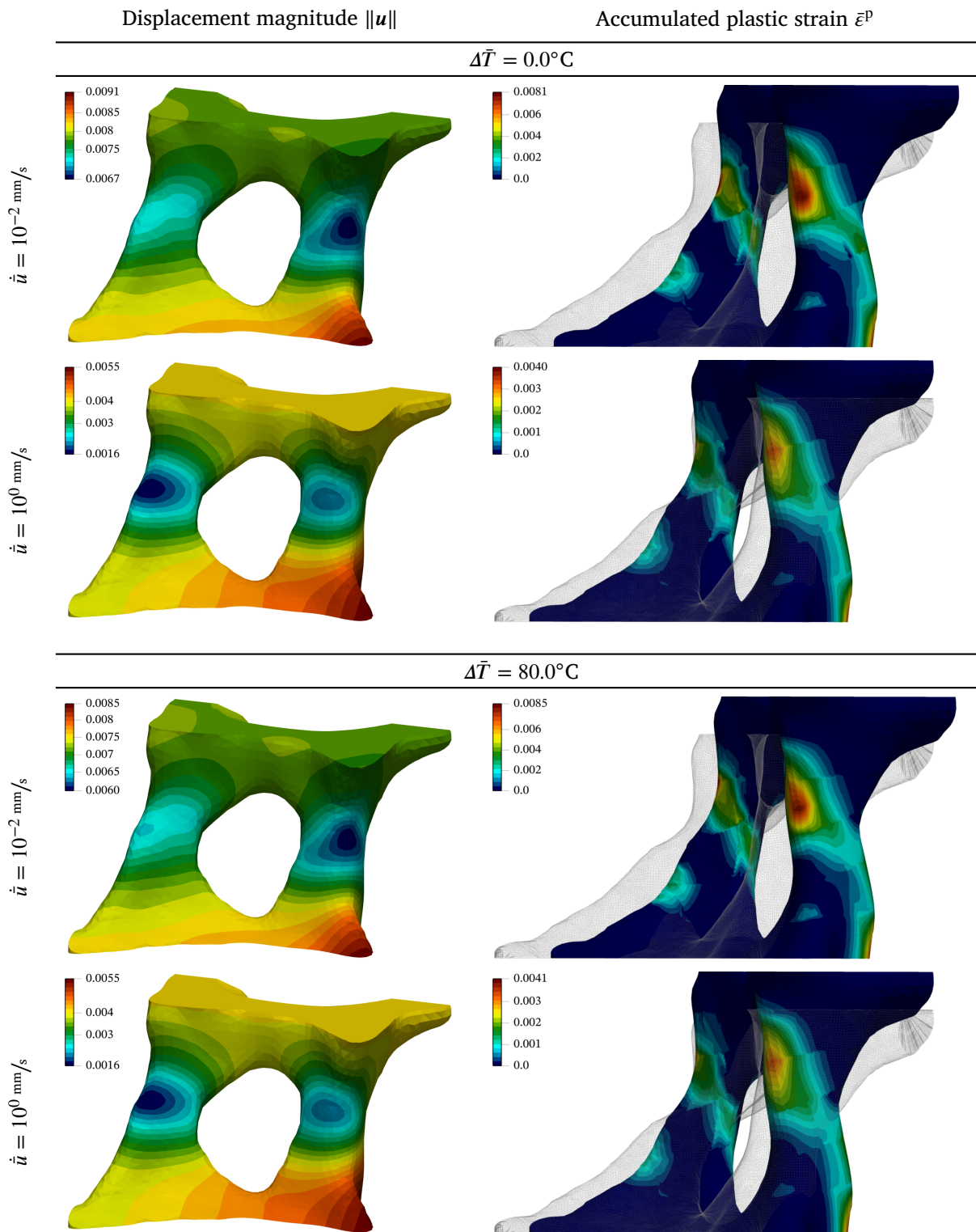


**Figure 6.11** The displacement magnitude and accumulated plastic strain distribution on the domain of the foam pore for different temperatures and deformation rates.

# Chapter 7

## Conclusion and outlook

### Summary

Recalling the main objective of the thesis being

*“[...] the identification of a viscoplastic material model for metals and implementation into the framework of the finite cell method using multi-level hp overlay refinements.”*

This has been achieved by using the  $J_2$  flow theory together with the viscoplastic flow vector defined by Perić and Perzyna. The finite cell method has been proven to be in good agreement with the reference solution and the standard FEM solution. The multi-level  $hp$  refinement technique improved the smoothness of the plastic strain field successfully while not having a significant impact on the force-displacement curves.

Secondly, the model should be extended to

*“[...] the thermo-viscoplastic coupling in order simulated rate-dependent plastic flow of metals at high temperatures.”*

The coupling was started with the linear theory of thermoelasticity which was implemented successfully and validated by the ring benchmark problem. Based on a fully coupled thermo-viscoplastic theory by [Oppermann et al., 2022], a reduced model was extracted to test the coupling on quadrature point level. Even though no reference data was obtainable for this model, the results presented a reasonable and expected behavior. This model is considered to be a solid preparation for a more sophisticated thermo-viscoplastic coupling.

Lastly, tackling the challenge of

*“[...] the efficient numerical integration of cut-cells in the finite cell method for nonlinear analysis. The novel non-negative moment fitting approach is tested on the models throughout this work in terms of stability and efficiency.”*

In the direct comparison against the adaptive spacetree quadrature, the non-negative

moment fitting did not show any relevant loss of accuracy while gaining reductions of around 75% to 90% in the number of quadrature points and on average around 30% reduction of the computation runtime. For geometrically more complex methods, the decrease in quadrature points even reached a reduction of 98.51% without losing convergence properties in the nonlinear equations. The implemented quadrature was able to work well along with the multi-level *hp* refinement technique. However, a tendency of the non-negative moment fitting can be observed to be less efficient for higher refinement levels.

## Outlook

### Refinement techniques for viscoplastic models

Besides the Kelly estimator based on the displacement gradient jump along the leaf boundaries, another metric could be tested which is more specialized on the viscoplastic processes in the material. It may be a profitable idea to refine along the plastic front, that is the interface between the elastic and plastic region. Additionally, a refinement strategy that is not only based on the final load step but refines and de-refines adaptively in between the load steps should be tested. Further, an anisotropic refinement could be more target-oriented, especially for slender geometries like the perforated plate.

### Thermo-viscoplastic coupling

As introduced in [Oppermann et al., 2022] a thermo-viscoplastic coupling can be coupled both ways to capture the heat generation due to plastic flow. The authors used the AceGen-Toolbox for the computer algebra program *Wolfram Mathematica* which can generate exact derivatives for the material tangent operator and allows for automatic generation of optimized source code [Korelc and Wriggers, 2016]. This way, the material description can be chosen to be more complex such that a more sophisticated thermo-mechanical coupling can be implemented.

### Digital twin experiments

The ultimate validation of the thermo-viscoplastic finite cell model could be achieved by taking probes for instant of metal foam structures for which the material is tested and can be fitted to the respective ansatz function as shown for experimental data taken from literature. By scanning the probes via computer tomography, an exact geometric description of the complex inner structure can be generated and analyzed by the finite cell method. Given the boundary conditions and temperature during testing, the digital finite cell model could be compared directly to its real-world twin. Methods like this are highly relevant for parts under strict safety regulations.

# Bibliography

- [Abedian and Düster, 2019] Abedian, A. and Düster, A. (2019). Equivalent legendre polynomials: Numerical integration of discontinuous functions in the finite element methods. *Computer Methods in Applied Mechanics and Engineering*, 343:690–720.
- [Abedian et al., 2013] Abedian, A., Parvizian, J., Düster, A., Khademyzadeh, H., and Rank, E. (2013). Performance of different integration schemes in facing discontinuities in the finite cell method. *International Journal of Computational Methods*, 10(03):1350002.
- [Anand and Govindjee, 2020] Anand, L. and Govindjee, S. (2020). *Continuum mechanics of solids*. Oxford University Press.
- [Bataille and Kestin, 1977] Bataille, J. and Kestin, J. (1977). Thermodynamics of mixtures.
- [Bathe, 2006] Bathe, K.-J. (2006). *Finite element procedures*. Klaus-Jurgen Bathe.
- [Carlson, 1973] Carlson, D. E. (1973). Linear thermoelasticity. In *Linear Theories of Elasticity and Thermoelasticity: Linear and Nonlinear Theories of Rods, Plates, and Shells*, pages 297–345. Springer.
- [Cottrell et al., 2009] Cottrell, J. A., Hughes, T. J., and Bazilevs, Y. (2009). *Isogeometric analysis: toward integration of CAD and FEA*. John Wiley & Sons.
- [Davis, 1967] Davis, P. J. (1967). A construction of nonnegative approximate quadratures. *Mathematics of Computation*, 21(100):578–582.
- [Davis, 1969] Davis, P. J. (1969). Approximate integration rules with nonnegative weights. *Lectures in differential equations*, 2:233–256.
- [De Berg, 2000] De Berg, M. (2000). *Computational geometry: algorithms and applications*. Springer Science & Business Media.
- [De Borst et al., 2012] De Borst, R., Crisfield, M. A., Remmers, J. J., and Verhoosel, C. V. (2012). *Nonlinear finite element analysis of solids and structures*. John Wiley & Sons.

- [de Souza Neto et al., 2011] de Souza Neto, E. A., Perić, D., and Owen, D. R. J. (2011). *Computational methods for plasticity: theory and applications*. John Wiley & Sons.
- [Düster and Allix, 2020] Düster, A. and Allix, O. (2020). Selective enrichment of moment fitting and application to cut finite elements and cells. *Computational Mechanics*, 65:429–450.
- [Düster and Hubrich, 2020] Düster, A. and Hubrich, S. (2020). Adaptive integration of cut finite elements and cells for nonlinear structural analysis. *Modeling in Engineering Using Innovative Numerical Methods for Solids and Fluids*, pages 31–73.
- [Düster et al., 2008] Düster, A., Parvizian, J., Yang, Z., and Rank, E. (2008). The finite cell method for three-dimensional problems of solid mechanics. *Computer methods in applied mechanics and engineering*, 197(45-48):3768–3782.
- [Fukuhara and Sanpei, 1993] Fukuhara, M. and Sanpei, A. (1993). Elastic moduli and internal friction of low carbon and stainless steels as a function of temperature. *ISIJ international*, 33(4):508–512.
- [Garhuom and Düster, 2022] Garhuom, W. and Düster, A. (2022). Non-negative moment fitting quadrature for cut finite elements and cells undergoing large deformations. *Computational Mechanics*, 70(5):1059–1081.
- [Goldstein et al., 2002] Goldstein, H., Poole, C., and Safko, J. (2002). Classical mechanics.
- [Green, 1839] Green, G. (1839). On the laws of the reflection and refraction of light at the common surface of two non-crystallized media. *Transactions of the Cambridge Philosophical Society*, 7:1–24.
- [Hansbo, 2005] Hansbo, P. (2005). Nitsche’s method for interface problems in computational mechanics. *GAMM-Mitteilungen*, 28(2):183–206.
- [Hetnarski et al., 2009] Hetnarski, R. B., Eslami, M. R., and Gladwell, G. (2009). *Thermal stresses: advanced theory and applications*, volume 41. Springer.
- [Hubrich and Düster, 2019] Hubrich, S. and Düster, A. (2019). Numerical integration for nonlinear problems of the finite cell method using an adaptive scheme based on moment fitting. *Computers & Mathematics with Applications*, 77(7):1983–1997.
- [Hughes, 2012] Hughes, T. J. (2012). *The finite element method: linear static and dynamic finite element analysis*. Courier Corporation.
- [Huybrechs, 2009] Huybrechs, D. (2009). Stable high-order quadrature rules with equidistant points. *Journal of computational and applied mathematics*, 231(2):933–947.

- [Joulaian et al., 2016] Joulaian, M., Hubrich, S., and Düster, A. (2016). Numerical integration of discontinuities on arbitrary domains based on moment fitting. *Computational Mechanics*, 57:979–999.
- [Kohlrausch, 1986] Kohlrausch, F. (1986). Praktische physik. zum gebrauch fuer unterricht, forschung und technik. Stuttgart: Teubner.
- [Korelc and Wriggers, 2016] Korelc, J. and Wriggers, P. (2016). *Automation of Finite Element Methods*. Springer.
- [Kudela et al., 2015] Kudela, L., Zander, N., Bog, T., Kollmannsberger, S., and Rank, E. (2015). Efficient and accurate numerical quadrature for immersed boundary methods. *Advanced modeling and simulation in engineering sciences*, 2:1–22.
- [Kudela et al., 2016] Kudela, L., Zander, N., Kollmannsberger, S., and Rank, E. (2016). Smart octrees: Accurately integrating discontinuous functions in 3d. *Computer Methods in Applied Mechanics and Engineering*, 306:406–426.
- [Lawson and Hanson, 1995] Lawson, C. L. and Hanson, R. J. (1995). *Solving least squares problems*. SIAM.
- [Legrain, 2021] Legrain, G. (2021). Non-negative moment fitting quadrature rules for fictitious domain methods. *Computers & Mathematics with Applications*, 99:270–291.
- [Liscic et al., 2010] Liscic, B., Tensi, H. M., Canale, L. C., and Totten, G. E. (2010). *Quenching theory and technology*. CRC Press.
- [Marchuk et al., 1986] Marchuk, G., Kuznetsov, Y. A., and Matsokin, A. (1986). Fictitious domain and domain decomposition methods.
- [Müller et al., 2013] Müller, B., Kummer, F., and Oberlack, M. (2013). Highly accurate surface and volume integration on implicit domains by means of moment-fitting. *International Journal for Numerical Methods in Engineering*, 96(8):512–528.
- [Nitsche, 1971] Nitsche, J. (1971). Über ein variationsprinzip zur lösung von dirichlet-problemen bei verwendung von teilräumen, die keinen randbedingungen unterworfen sind. In *Abhandlungen aus dem mathematischen Seminar der Universität Hamburg*, volume 36, pages 9–15. Springer.
- [Nowacki, 2013] Nowacki, W. (2013). *Thermoelasticity*. Elsevier.
- [Oppermann et al., 2022] Oppermann, P., Denzer, R., and Menzel, A. (2022). A thermo-viscoplasticity model for metals over wide temperature ranges-application to case hardening steel. *Computational Mechanics*, 69(2):541–563.
- [Parvizian et al., 2007] Parvizian, J., Düster, A., and Rank, E. (2007). Finite cell method: h-and p-extension for embedded domain problems in solid mechanics. *Computational Mechanics*, 41(1):121–133.

- [Perić, 1993] Perić, D. (1993). On a class of constitutive equations in viscoplasticity: formulation and computational issues. *International journal for numerical methods in engineering*, 36(8):1365–1393.
- [Perzyna, 1971] Perzyna, P. (1971). Thermodynamic theory of viscoplasticity. *Advances in applied mechanics*, 11:313–354.
- [Petö et al., 2020] Petö, M., Duvigneau, F., and Eisenträger, S. (2020). Enhanced numerical integration scheme based on image-compression techniques: application to fictitious domain methods. *Advanced Modeling and Simulation in Engineering Sciences*, 7:1–42.
- [Petö et al., 2021] Petö, M., Duvigneau, F., Juhre, D., and Eisenträger, S. (2021). Enhanced numerical integration scheme based on image compression techniques: Application to rational polygonal interpolants. *Archive of Applied Mechanics*, 91:753–775.
- [Rank, 1992] Rank, E. (1992). Adaptive remeshing and hp domain decomposition. *Computer Methods in Applied Mechanics and Engineering*, 101(1-3):299–313.
- [Rank and Werner, 1986] Rank, E. and Werner, H. (1986). An adaptive finite element approach for the free surface seepage problem. *International journal for numerical methods in engineering*, 23(7):1217–1228.
- [Sadd, 2009] Sadd, M. H. (2009). *Elasticity: theory, applications, and numerics*. Academic Press.
- [Schillinger et al., 2012] Schillinger, D., Düster, A., and Rank, E. (2012). The hp-d-adaptive finite cell method for geometrically nonlinear problems of solid mechanics. *International Journal for Numerical Methods in Engineering*, 89(9):1171–1202.
- [Schillinger and Ruess, 2015] Schillinger, D. and Ruess, M. (2015). The finite cell method: A review in the context of higher-order structural analysis of cad and image-based geometric models. *Archives of Computational Methods in Engineering*, 22:391–455.
- [Schmäke, 2023] Schmäke, J. N. (2023). Hierarchic refinement and plasticity analysis in the framework of the finite cell method. Master's thesis, University of Applied Sciences Düsseldorf.
- [Schröder, 2011] Schröder, A. (2011). Constrained approximation in hp-fem: Unsymmetric subdivisions and multi-level hanging nodes. In *Spectral and High Order Methods for Partial Differential Equations: Selected papers from the ICOSAHOM'09 conference, June 22-26, Trondheim, Norway*, pages 317–325. Springer.
- [Šolín et al., 2008] Šolín, P., Červený, J., and Doležel, I. (2008). Arbitrary-level hanging nodes and automatic adaptivity in the hp-fem. *Mathematics and Computers in Simulation*, 77(1):117–132.

- [Šolín et al., 2010] Šolín, P., Dubcova, L., Červený, J., and Doležel, I. (2010). Adaptive hp-fem with arbitrary-level hanging nodes for maxwell's equations. *Adv. Appl. Math. Mech.*, 2(4):518–532.
- [Spittel and Spittel, 2009a] Spittel, M. and Spittel, T. (2009a). 4.2 young's modulus of steel: Datasheet from landolt-börnstein - group viii advanced materials and technologies · volume 2c1: “metal forming data of ferrous alloys - deformation behaviour”.
- [Spittel and Spittel, 2009b] Spittel, M. and Spittel, T. (2009b). Steel symbol/number: 16mncr5/1.7131: Datasheet from landolt-börnstein - group viii advanced materials and technologies · volume 2c1: “metal forming data of ferrous alloys - deformation behaviour”.
- [Sudhakar and Wall, 2013] Sudhakar, Y. and Wall, W. A. (2013). Quadrature schemes for arbitrary convex/concave volumes and integration of weak form in enriched partition of unity methods. *Computer Methods in Applied Mechanics and Engineering*, 258:39–54.
- [Szabó et al., 2004] Szabó, B., Düster, A., and Rank, E. (2004). The p-version of the finite element method. *Encyclopedia of computational mechanics*.
- [Szabó, 1986] Szabó, B. A. (1986). Estimation and control of error based on p convergence. *Accuracy estimates and adaptive refinements in finite element computations*, 1:61–70.
- [Tchakaloff, 1957] Tchakaloff, V. (1957). Formules de cubatures mécaniques à coefficients non négatifs. *Bull. Sci. Math*, 81(2):123–134.
- [Ventura, 2006] Ventura, G. (2006). On the elimination of quadrature subcells for discontinuous functions in the extended finite-element method. *International journal for numerical methods in engineering*, 66(5):761–795.
- [Ventura and Benvenuti, 2015] Ventura, G. and Benvenuti, E. (2015). Equivalent polynomials for quadrature in heaviside function enriched elements. *International Journal for Numerical Methods in Engineering*, 102(3-4):688–710.
- [Xu et al., 2016] Xu, F., Schillinger, D., Kamensky, D., Varduhn, V., Wang, C., and Hsu, M.-C. (2016). The tetrahedral finite cell method for fluids: Immersogeometric analysis of turbulent flow around complex geometries. *Computers & Fluids*, 141:135–154.
- [Zander et al., 2016] Zander, N., Bog, T., Elhaddad, M., Frischmann, F., Kollmannsberger, S., and Rank, E. (2016). The multi-level hp-method for three-dimensional problems: Dynamically changing high-order mesh refinement with arbitrary hanging nodes. *Computer Methods in Applied Mechanics and Engineering*, 310:252–277.

- [Zander et al., 2015] Zander, N., Bog, T., Kollmannsberger, S., Schillinger, D., and Rank, E. (2015). Multi-level hp-adaptivity: high-order mesh adaptivity without the difficulties of constraining hanging nodes. *Computational Mechanics*, 55(3):499–517.
- [Zander et al., 2012] Zander, N., Kollmannsberger, S., Ruess, M., Yosibash, Z., and Rank, E. (2012). The finite cell method for linear thermoelasticity. *Computers & Mathematics with Applications*, 64(11):3527–3541.
- [Zander, 2017] Zander, N. D. (2017). *Multi-level hp-FEM: dynamically changing high-order mesh refinement with arbitrary hanging nodes*. PhD thesis, Technische Universität München.

## **Declaration of Academic Integrity**

I, Oliver Wege, hereby affirm that I have written this Master of Science thesis on my own and that I have used no sources or aids other than the ones stated. This is the final version of the thesis, to be graded by the University of Applied Sciences Düsseldorf.

Düsseldorf, March 20, 2024

Oliver Wege